

UNCLASSIFIED

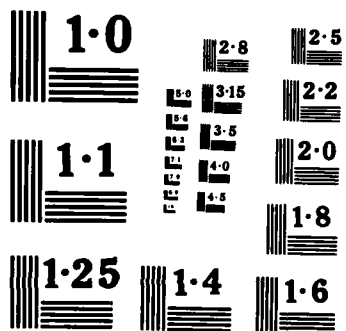
ARTICLES/CO FOREIGN TECHNOLOGY DIV ARIGHT-FITTER
AFB OH M JI ET AL 05 AUG 85 FTD-ID(RS)T-1515-84

1/3

F/G 1/3

NL

A 10x10 grid of squares. The top-left corner contains a small cluster of white squares: the square at (row, column) (1, 2) is white, and the squares at (2, 1), (2, 2), and (2, 3) are also white. All other squares in the grid are black.



NATIONAL BUREAU OF STANDARDS
MICROCOPY RESOLUTION TEST CHART

2

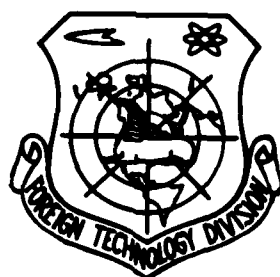
FTD-ID(RS)T-1515-84

AD-A158 454

FOREIGN TECHNOLOGY DIVISION



ACTA AERONAUTICA ET ASTRONAUTICA SINICA
(Selected Articles)



DTIC FILE COPY

DTIC
ELECTE
AUG 30 1985
S D E

Approved for public release;
distribution unlimited.

85 8 27 063

FTD-ID(RS)T-1515-84



EDITED TRANSLATION

FTD-ID(RS)T-1515-84

5 August 1985

MICROFICHE NR: FTD-85-C-000638

ACTA AERONAUTICA ET ASTRONAUTICA SINICA (Selected Articles)

English pages: 238

Source: Hangkong Xuebao, Vol. 5, Nr. 2, June 1984, pp. 103-167; 178-192; 200-247

Country of origin: China

Translated by: SCITRAN

F33657-84-D-0165

Requester: FTD/TQTA

Approved for public release; distribution unlimited.

Accession For	
NTIS GRA&I	<input checked="" type="checkbox"/>
DTIC TAB	<input type="checkbox"/>
Unannounced	<input type="checkbox"/>
Justification	
By _____	
Distribution/ _____	
Availability Codes	
Dist	Avail and/or Special
A-1	

THIS TRANSLATION IS A RENDITION OF THE ORIGINAL FOREIGN TEXT WITHOUT ANY ANALYTICAL OR EDITORIAL COMMENT. STATEMENTS OR THEORIES ADVOCATED OR IMPLIED ARE THOSE OF THE SOURCE AND DO NOT NECESSARILY REFLECT THE POSITION OR OPINION OF THE FOREIGN TECHNOLOGY DIVISION.

PREPARED BY:

TRANSLATION DIVISION
FOREIGN TECHNOLOGY DIVISION
WP-AFB, OHIO.

FTD-ID(RS)T-1515-84

Date 5 Aug 19 85

Table of Contents

→ Partial contents

Graphics Disclaimer	iii
Congratulations and Wishes, by Ji Wenmei	1
New Developments of Aeroelastic Research; by Guan De	20
Scene Matching and its Application to Aerospace Electronic Systems; by Sun Ahongkang	33
Strengthening the Study of the Usability of Aircraft Materials, by Wu Yunshu	59
A Kernel Function Method for Computing Unsteady Load on Three-dimensional Wings in Transonic Flow, by Wu Yizhao	75
Root Locus Method and Automatic Identification of Modes in Flutter Analysis; by Yang Xingjian and Li Guangquan	91
Determination of Axis and Angle of Rotation of Retractable Landing Gear; by Zhang Qixian	104
δ -Function and Generalized Tables of Thermodynamic Properties of Combustion Products of C ₂ H ₄ -Air System; by Fan Zuomin and Fu Xunquan	114
Multi-rate Digital Flight Control System; by Guo Buofeng	122
Reconfigurable Redundancy Management Strategy for a Triplex DFBW System; by Li Lichun	134
An Equivalent Strength Method for Optimum Design of Composite Laminates, by Liu Fanglong, and Huang Jixi	148

Modal Test and Parameter Identification of a Flutter Wing, by Zhang Lingmi	169
An Experimental Study on the Effect of Overload on Fatigue Life, by Zeng Chunhua and Guo Kangmin	183
An Experimental Investigation on Turbojet Engine Response to Turbulence-type of Dynamic Inlet Distortion, by Chen Fuqun, Li Wenlan, Wang Zongyuan, Cong Mengzi, Lu Baoquan and Zheng Lizhi	194
Using a Two-Dimensional Laser-Doppler Anemometer to Study a Complex Flow Field in a Combustor, by Lin Qinxun, Ding Yisheng, Du Qinfang, Tang Ming and Xiao Ningfang	210
Characteristics of Multi-ply Carbon/Epoxy Composite Materials and Acoustic Emission Analysis, by Xian Xingjuan and Jiang Conxing	225

GRAPHICS DISCLAIMER

All figures, graphics, tables, equations, etc. merged into this translation were extracted from the best quality copy available.

Congratulations and Wishes

/103

Chairman of the Society of Aeronautics of China, Ji Wenmei

The aerospace industry is one of the important markers of science and technology, as well as industrial development for a country. Its rapid development is based on the success in many disciplines of science and engineering. It, in turn, promotes the development of other science and engineering disciplines. The use of computers and a series of new instruments and panels significantly shortens the design, development and production cycle. The quality is improved and the cost is reduced. In the last twenty years, the ratio of electronic equipment in flight vehicles has increased steadily. The rate at which communication, navigation, control, instrument and electronic confrontation devices are developed far exceeds that for the flight vehicle itself. New materials and technologies are developed rapidly. Composite materials, in particular, are widely used in flight vehicles. The development of materials science in the past thirty years has surpassed the development in three hundred years prior to the fifties. Furthermore, materials science is closely linked to engineering.

((Acta Aeronautica et Astronautica Sinica)) printed over 300 papers to reflect the results of aerospace research in China. To some extent, it shows the academic level of scientists in China. The journal thoroughly implemented the "double hundred" policy and published some articles of different views. It helps the gradual build-up of a good atmosphere of collaboration. The journal began to pay attention to articles written by young and middle age scientists. It also recommended certain articles to participate in evaluations and international conferences in order to discover, encourage and raise useful talents.

((Acta Aeronautica et Astronautica Sinica)) was born in 1965. A year and half later, publishing was stopped due to the culture revolution. It was reinstated in 1978 and worldwide publication began in 1980. In the last 3-4 years, the

editing and publishing of the journal continued to improve. Very encouraging accomplishments have been obtained. The journal is gradually becoming a more important portion of society.

In order to satisfy the needs in the development of the aerospace industry, especially in electronics and materials science, we wish to publish more articles concerning experimental studies and techniques, as well as reports on actual practices of theoretical results. In addition, we hope to be able to control the number of words based on the rules specified. The purpose is to free more space for technical communications, overviews and reviews of specific topics, and letters from readers to make the journal more lively. Moreover, a youth corner should be made available to young scientists who are most aggressive and have the highest potential. This will allow them to make creative contributions as early as possible.

I wish that ((Acta Aeronautica et Astronautica Sinica)) can continue to improve the academic level under the guidance of the Chinese Society of Aeronautics. It should be closely linked to production. The contents should be enriched with its own characters. On the twentieth anniversary of the Society of Astronautics of China, I wish that the journal can be make an even larger contribution to the aerospace industry of China.

Table 1 Introduction to Structure Design Development

/104

	7. 1903年莱特飞机时代的 结构设计特点	14. 航空发展以后的情况: 新结构、新材料、新方法
1. 布局	8. 双翼机或带支撑的单翼机 (机翼相对厚度15~16%)	15. 单翼机, 高速翼型 (相对厚度4~6%), 高速翼平面形 (小展弦比), 整体油箱, 多种外挂物, 变后掠, 可折叠
2. 结构型式	9. 杆梁帆布结构	16. 薄壳结构, 整体结构, 夹层结构, 蜂窝结构, 复合材料结构
3. 材料	10. 木, 钢丝, 张线, 亚麻袋布	17. 铝合金 (1930年起), 镁合金 (1930~1940年起), 不锈钢 (1940~1950年起), 钛合金 (1950年起), 复合材料和陶瓷材料 (1960年起)
4. 设计要求	11. 极简单的承载能力	18. 强度、刚度、稳定性、耐震性、复杂环境要求, 结构完整性、耐久性、损伤容限, 计算机辅助一体化设计、优化设计、可靠性设计
5. 分析方法	12. 一般结构力学方法	19. 飞行器结构力学、有限元素法、结构分析系统、结构综合分析、气动弹性力学、模态控制与分析技术、疲劳与断裂、高温结构力学、统计处理方法、结构可靠性分析法
6. 试验技术	13. 老式静力试验技术	20. 多点自动控制协调加载系统, 地面振动试验, 数据采集处理系统, 疲劳与损伤容限试验, 先进的应力、变形、裂纹检测方法, 热应力试验, 复杂环境模拟条件

Key:

1. layout
2. structure
3. materials
4. design requirements
5. analytical methods
6. experimental techniques
7. structure design characteristics in the Wright era in 1903
8. biplane or supported single wing plane (relative wing thickness 15-16%)
9. rod and canvas
10. wood, steel wire, tension line, linen
11. simple load capability
12. usual structural mechanics
13. old-fashioned static tests
14. after aeronautic development: new structure, new materials and new methods
15. single wing plane, high speed wings (relative thickness 4-6%), high speed airfoil (small aspect ratio), bulk fuel tank, attachments, varying sweepback,

- capable of folding
16. thin wall structure, bulk structure, jacketed structure, honeycomb structure, composite material structure
 17. aluminum alloy (since 1930), magnesium alloy (since 1930-1940), stainless steel (since 1940-1950), titanium alloy (since 1950), composite materials and ceramics (since 1960)
 18. strength, rigidity, stability, shock resistance, complicated environmental requirements, structural integrity, durability, tolerance to damage, computer aided integrated design, optimization, reliable design
 19. flight vehicle structure mechanics, finite element method, structural analysis system, comprehensive structure analysis, elastic aerodynamics, modal control and analysis, fatigue and fracture, high temperature structure analysis, statistical treatment, structural reliability analysis
 20. automatic control coordinated loading system, ground vibration test, data acquisition and processing, fatigue and damage tolerance test, advanced detection methods for stress, deformation and cracks, thermal strength test and simulation of complicated environment.

Table 2 Major Incidents Due to Flight Vehicle Structure Failure

1. 年 代	4. 机 种	12 失 事 起 因	19 促 进 的 学 科
1903	5. 英国 Langley 飞行机模	13 机翼扭转扩大变形	20 刚度指标
2. 第一次世界大战 (1917)	6. 英国的DH-9飞机 7. 德国的D-8飞机	14 尾翼颤振	21 气动弹性力学
1934	8. 英国彗星 (Comet) 喷气旅客机	15 气密座舱疲劳爆裂	22 疲劳
1958	9 美国B-47轰炸机	16 机翼疲劳断裂	23 疲劳
1970	10 美国F-111战斗机	17 机翼铰轴断裂	24 断裂
3. 现代	11 高超音速飞机和航天器	18 热障	25 热强度和高温防护

1. era
2. First World War
3. now
4. type of vehicle
5. British Langely vehicle
6. British DH-9
7. German D-8
8. British Comet Passenger Jet
9. American B-47 bomber
10. American F-111 fighter
11. supersonic aircraft and spacecraft
12. cause of failure
13. twisted wing
14. tail fluttering
15. fatigue cracking of air tight cabin
16. fatigue fracture of wings
17. wing hinge fracture
18. thermal barrier
19. promoted discipline
20. rigidity indicator
21. elastic aerodynamics
22. fatigue
23. fatigue
24. cracking
25. thermal strength and high temperature protection

Table 3 Example of Drastic Improvement of Flight Performance

1. 年 代	2. 机 种	5. 飞行速度	8. 飞行高度
1934	3. 美国波音P-26A	6. 377公里/小时	9. 2286米
1979	4. 美国F-15A	7. 2655公里/小时 M=2.5	10. 18300米

Key:

1. era
2. aircraft
3. American Boeing P-26A
4. American F-15A
5. flying speed
6. 377 km/hour
7. 2655 km/hr, M = 2.5
8. altitude
9. 2286m
10. 18300m

In the area of structure, the situation is also similar. A /105
new efficient structure must also be tested under static,
dynamic, thermal, fatigue and cracking, and environmental
conditions. In addition, it is sometimes necessary to establish
new strength theory, analytical method and experimental
technique. It requires a long cycle. The thin wall structure is
still the primary structure. Various new structures such as bulk
structure, jacketed structure, honeycomb structure and composite
material structure are mixed in on occasion..

In the past 20 years, people have been studying methods to
make breakthroughs away from the conventional methods for
increasing structure strength or adjusting structure parameters
in solving some serious structure problems especially for
spacecraft. Servo systems combined into the structure are
employed to avoid any weight increase. For example, in order to
reduce the random and gust load on the lift surface (wings and
tail) and to avoid flutter, an active modal control technique was
developed in the sixties. It relies on changing the aerodynamic
profile and aerodynamic elasticity of the lift surface to
suppress the undesirable effect. The introduction of an active
system must be tested for stability and reliability.

The situation in the eighties can be described in the
following. On one hand, the structure of a vehicle is facing
very complex problems which must satisfy the various requirements
(statics, dynamics, heat, fatigue and cracking, complicated
environment). On the other hand, a large number of revolutionary
technologies are emerging. The introduction of these
technologies can overcome certain problems. However, they also
frequently bring new endangering factors. Usually, it requires a
10-30 years or longer research cycle to perfect the process. The
following data can explain this situation. In the United States,
there were, on the average, 12 new aircraft introduced based on
revolutionary technologies each year between 1930-1940. However,
it is estimated to be not more than 2 in the eighties. New
technologies used in a new model must be considered in the

preliminary design 6-8 years before the initial flight. The cycle required between the introduction and the widespread use of a new technology is much longer than before.

In the area of design analysis, the traditional methods for checking the structure design and strength have been drastically changed since 1960, because of rapid development in computer technology, especially after the successful development of finite element methods and structure analysis systems suitable for complicated aeronautical structures. A computer video aided design method to integrate overall, structure, aerodynamic and technical design is gradually being developed. Furthermore, a comprehensive structure analysis technique based on the finite element method and a mathematical program is used to optimize the structure. Structure design is no longer a simple process which involves designing first and checking later. Instead, it requires the simultaneous consideration of a large number of complicated conditions. An intercorrelated, iterative flow chart is created by combining the knowledge in various aspects. It becomes an integral part of flight vehicle systems engineering. The structure designers not only are required to have considerable experience in the selection of an optimized overall plan but also must master advanced computer aided design techniques. They must be able to utilize various subroutines, including profile design, structure design, overall structure analysis, elastic and plastic analysis, servo system analysis, etc., in order to meet the structure reliability requirements and to achieve the objective of design optimization.

II. Modern Structure Design Programs

As described above, the performance of the vehicles drastically raised the complexity of the structure and the design cost. In order to reduce cost and design time, shorten the cycle, avoid design errors, CADAM (Computer-graphics Augmented Design and Manufacturing) systems were introduced to obtain

The calculations and experimental determination of the dynamic characteristics of a structure is another basis for aeroelastic analysis. In this area, an aeronautical structure dynamic analysis system named HAJIF-II was established. Furthermore, the multipoint excitation technique for the determination of state parameters which is based on the phase resonance theory and the state parameters identification technique were applied industrially.

Design optimization of the structure with aeroelastic constraints has already been applied in engineering. To achieve this objective, a system for structural optimization with multiconstraints based on nonlinear mathematics, YIDOYU-1, and a multiconstraint design optimization system, SAFDOP, were established.

Installation of various external stores is a problem facing modern aircraft. To this end, a systematic experimental study was carried out on the flutter of external stores with flexible support. Some patterns were recognized.

Suppression of flutter is a new subject. As we conduct theoretical studies on various control patterns, active flutter suppression experiments are also being carried out in a low speed wind tunnel using dynamic models of two and three-dimensional wings, as well as a small aspect ratio, large sweepback angle wing.

In the area of flutter experimentation, after the random decay and least square method was successfully used in wind tunnel tests, it has already been employed to analyze the data on flutter experiments.

Some aspects are briefly discussed in the following:

Guan De

(Shengyang Aircraft Corporation) *

Abstract

Some new developments in aeroelastic research in China were discussed in this work. Primarily they include the calculation of transonic unsteady aerodynamics, the aircraft structure dynamic analysis system HAJIF-II and its applications, the aircraft structure multiconstraint optimization program YIDOYU-I, experimental investigation on external stores flutter and active flutter suppression.

I. Introduction

As we know, aeroelastic requirements have an important effect on the design of high performance aircraft. For these aircraft, in order to satisfy these aeroelastic requirements, the consequence is not limited to changes of certain structural dimensions. As a matter of fact it was actually demonstrated that an intolerable weight penalty may result if aeroelastic requirements were not taken into account in the selection of the structure and aerodynamic layouts. The designers may be forced to reselect these fundamental layouts.

This objective requirement promotes the development of aeroelastic research in China. In recent years, some progress has been obtained in aeroelastics, a leading edge multi-discipline subject.

The calculation of unsteady aerodynamic forces is a basis for aeroelastic analysis. A transonic unsteady aerodynamic calculation method was initiated by developing and perfecting a method based on the linearization of lift surface. Some two-dimensional results were obtained.

*received in January 1984

Reliability Requirements, Repeated Load and Fatigue,
August 22, 1975; MIL-A-008867E (USAF), Aircraft
Strength and Rigidity-Ground Tests, August 22, 1975.

References

- [1] Hadcock, R.N., Introduction of New SDM Technology into Production Systems, J. Aircraft, V.17, N.9, (1980), PP. 609-617.
- [2] Smyth, S.J., CADAM Data Handling from Design through Product Support, J. Aircraft, V.17, N.10, (1980), PP. 753-760.
- [3] J. Sobieszczanski-Sobieski & Bhat, R.B., Adaptable Structural Synthesis using Advanced Analysis and Optimization Coupled by a Computer Operating System, J. Aircraft, V.18, N.2, (1981), PP. 142-149.
- [4] Schmit, L.A., Jr., A New Structural Analysis/Synthesis Capability-ACCESS 1, AIAA Journal, V.14, May(1976), pp. 661-671.
- [5] Zienkiewicz, O.C., The Finite Element Method, 3rd Edition, McGraw-Hill, London, (1977)
- [6] The NASTRAN Manuals, Theoretical, NASA SP-221[04]; User's, NASA SP-222[04]; Programmer's, NASA SP-223[04], (1978).
- [7] MAGIC, An Automated General Purpose System for Structural Analysis, AFFDL-TR-68-56, AD 685190, (1969)
- [8] Schrem, E. and Roy J.R., An Automatic System for Kinematic Analysis, Proceedings of IUTAM Tome 2, (1970), PP. 477-507. (Finite Element Method in Solid Mechanics, translated edition, Volume II, Science Publishing Co., (1977), 300-321.
- [9] Richard, S. Shevell, Technological Development of Transport Aircraft, J. Aircraft, V.17, N.2, (1980), PP. 67-80.
- [10] U.S. Air Force Damage Tolerance Design Manual (Vol. 1), translated by Huang Yushan et al, Northwest Polytech University, 1982, with U.S. Military Specification: MIL STD-1530(A), Outline of Structure Integrity of Aircraft, December 11, 1975; MIL-A-8344, Aircraft Damage Tolerance Requirement, July 2, 1975; MIL-A-008866B (USAF), Aircraft Strength and Rigidity Reliability Requirements, Repeated Load and Fatigue, August 22, 1975; MIL-A-008867B (USAF), Aircraft Strength and Rigidity

/111

loading points, several hundred measuring channels, and several thousand foil gages. Furthermore, there is a computer data acquisition and processing system to obtain results on-site. The number of measurements may reach several hundred thousands in a test.

Various countries built large scale laboratories. The largest in the world is located in Georgia by Lockheed. The main laboratory was built for the military transport C-5A. The dimensions are 189 x 148 x 43m³. The maximum load is 1300000 kg. Stress can be measured at 3850 points. The investment was 1,500,000 dollars. Large size equipment for fatigue, high temperature, vibration, sway and shock is available in various countries.

Measuring techniques have been revolutionized in development testing. In addition to electrical measurements, there are laser holography, the cloud pattern method, optical elastic freeze, optical elastic coating, x-ray acoustic emission and optical fiber detection.

IX. Conclusions

As described above, structure design and strength problems have become very complicated. A huge research team is required. In order to satisfy this need, all nations have established authoritative organizations to formulate strength specifications and to form advanced laboratories and research institutions. In order to solve major problems encountered, it is necessary to develop corresponding disciplines. Computer technology is widely used to build various data bases for data, reports, programs, manuals and literature so that the technological reserve is always ahead of production. New experience and methods are also obtained in the development of new models to perfect the structure design of the vehicle in order to promote continuous development of systems engineering of aerospace vehicles.

VII. Structure Reliability Analysis

Reliability design of electronic elements has already been extensively investigated. In the structure design of a flight vehicle, load environments of the structure, as well as material and structure characteristics, have random factors. It is especially true for fatigue fracture characteristics. Therefore, a rational analysis should employ a statistical method to predict the probability of structure destruction as a reliability analysis.

In early 1960, the concept of reliability design of the structure was introduced. In the reliability analysis on the structure, we must consider many factors such as the static strength of the structure, formation of fatigue cracking, propagation, loss of stability, residual strength of the structure, statistical distribution of load, crack inspection cycle and detection capability, initial damage, and structure changes. An optimized design aimed at reliability is significantly different from an optimized design based on static strength. Because a statistical distribution of a large amount of raw data is required in a reliability analysis and it is very difficult to analyze a complicated structure of vital importance, it is still far from being a practical tool for structure design.

VIII. Structure Testing

/110

With the development of aerospace technology, structure testing of a vehicle is required to be done more and more rigorously. Items to be tested also increase due to structure problems in statics, dynamics, heat, fatigue fracture and environment.

Between 1970-1980, computer controlled hydraulic servo-systems have been used to automatically adjust the loading system in full size structure tests. In thermal strength tests, heating systems are also included. There are several hundred loads and

Current experience is insufficient to formulate specifications for advanced composite materials and landing gear parts.

VI. Complex Environmental Conditions

Aerodynamic heating of the modern high speed aircraft can reach 200-800°C. The surface temperature of a spacecraft reentering the atmosphere will rise to above 1200°C. This brings about a serious thermal strength problem, technically called a thermal barrier. In addition, the heat released by the engine, solar radiation and high temperature radiation due to nuclear explosion will create a severe thermal environment. In order to break the thermal barrier, not only a thermal strength analysis including thermal flutter, thermal fatigue and thermal impact is required, but also high temperature resistant materials such as titanium alloys, stainless steel, ceramics and composite materials must be selected. Furthermore, appropriate structures such as wave, jacket and composite structures must be selected. Thermal protection design must be done for extreme temperatures. It is usually classified into absorption and radiation. The former uses a melting mechanism to disperse the heat by using materials such as resin, carbon, phenol and aldehyde dacron. In the latter case, materials such as molybdenum, titanium, ceramics, graphite, and boron-silicon composite are used to form a double or multiple layer structure which is radiating on the outside and insulating on the inside.

An aerospace structure must also be capable of surviving the vibration and impact during transport and launching, the thermal vacuum in space, high energy particle (electron, proton) radiation, ultraviolet radiation and electromagnetic fields. In a cold and hot alternating environment in space, materials and bonding agents will age and fatigue.

order to minimize the maintenance cost. Materials section, processing, inspection, design details, stress level and preventive measures are adopted to reach a good state of application. In the designed load environment, the structure lifetime of an aircraft should be greater than the design lifetime.

Damage tolerance is to eliminate the potential harmful effect due to defects in materials, manufacture and technique through materials selection, stress control, anti-fracture design concept, technical control of manufacturing processes and prudent inspection procedures. The analysis is to assume that the new structure has an initial damage to predict the time to reach critical cracking under a variable load by performing a fatigue fracture analysis. After taking the scatter into account, an inspection cycle is specified. The dimension of the initial damage is determined by the capability of the non-destructive testing equipment at the manufacturer. The probability of detection must also be considered. The dimension of the critical crack is determined by the rule that the residual strength of the structure should not be less than the fail-safe load. The latter is related to the detectability of the crack, which is specified in the strength specification. /109

A full size damage tolerance test usually uses available experimental parts, including those used in development testing, full size static test or durability test.

A great deal of progress has been made in fatigue and fracture. Hundreds of calculation models were mentioned in the literature. However, a breakthrough is still needed in mechanistic study. Miner Law and Paris equations are still mostly used in the structure design of freight vehicles, perhaps with some modifications. The accuracy and reliability of the analysis are still to be further improved. It may be concluded that design experience is more important than quantitative analysis, development testing is more important than full size verification, and fatigue fracture still needs long term studies.

separate the free decay response due to random input through statistical averaging in order to obtain the frequency and damping characteristics of the structure.

Direct parametric identification is to directly measure the structural response due to an input force. The mechanical resistance matrix of the structure is established to determine the modal parameters through characteristic analysis.

V. Applications of Fatigue and Fracture

Since the incidents of the Comet in 1954 and F-111 in 1970, fatigue and fracture is a key topic in the aerospace industry. U.S. Military specifications represent the advanced technical standards in the world. Relevant documents include ASIP (Aircraft Structure Integrity Program), durability requirements, damage tolerance requirements and ground testing.

ASIP was established by the United States in early 1970. Its objective is to ensure the combat readiness of military aircraft. The aircraft are required to have sufficient structure strength, rigidity, damage tolerance and durability. They are called structure integrity as a whole. ASIP requires that damage tolerance and durability should be included in the early design stage. Materials, weight, performance and cost should be investigated and development testing should be initiated. A full size test should be conducted in the development process in order to determine whether the structure design is appropriate. ASIP also requires that potential defects should be discovered in use as early as possible. Structure elements should be checked, replaced or repaired systematically. Furthermore, they should be measured to serve as the basis for improving future design methods and guidelines. ASIP exceeds the scope of conventional strength analysis. It is a comprehensive system from design to end use.

The objective of durability design is to reduce fatigue cracking and other deterioration of structures and materials in

parameters of the servo system are also included.

Some researchers also introduced plans to actively prevent the/108 sway of the front wheel.

Modal analysis is widely used in the dynamic analysis of a complicated aeronautical structure. Since 1970, modal analysis has been rapidly developed. Both analytical techniques and experimental methods are revolutionalized. It is still being further developed.

Currently, Guyan's condensed method and mode synthesis technique are commonly used in the analysis. Furthermore, analytical methods are used to improve the shape function. Dynamic analysis programs have been established in most structure analysis systems. Damping (complex mode analysis) and non-linearity are also considered in modal analysis.

In addition to the conventional single point excitation frequency analysis and multiple point excitation mode response method such as the semi-automatic MAMA (Manual-Apparatus) and automatic GRAMPA (Ground Resonance Automatic Multipoint Apparatus), many new experimental techniques have been developed. They include the instantaneous excitation method, random excitation method and parametric identification technique.

The Multipoint excitation frequency response method is a recently developed method. It combines the advantages of the two conventional methods mentioned above. In addition to solving the simultaneous equations, signal processing and measurement are similar to those in the single point method.

The Ibrahim time domain method does not require the instantaneous input from the measuring system. Modal parameters are determined by the free decay response in the time domain. However generalized mass or rigidity of the mode cannot be determined.

The random decrease technique was an experimental technique developed by Henry A. Cole Jr. in 1971. It only had qualitative requirements for the input and performs data processing with respect to the response. The fundamental principle is to

commercial software systems in the international market. Relatively famous aerospace structure analysis systems include the NASA's NASTRAN system, AFFOL's MAGIC system, and the ASKA system developed by Stogart University and ISD in Germany. In addition, the Chinese Aerospace Industry Ministry is also developing the HATIF system. A large scale structure analysis system usually contains several hundred thousand lines.

The capability of structure analysis systems continues to expand and improve toward the direction of graphics interaction. Man-computer dialogue is carried out through graphics display devices. The data input/output and processing techniques are perfected to be more closely coordinated with computer aided design.

IV. Active Modal Control and Modal Analysis

Because of the effect of dynamic load and elastic aerodynamics on the structure, particularly in the area of lift, serious overload or flutter may be induced at times. The conventional technique to overcome this type of problem is to adjust the rigidity and mass distribution. Sometimes certain aerodynamic parameters are also adjusted and dampers are used. These techniques are called PCT (Passive Control Technology).

In the sixties, ACT (Active Control Technology) was introduced. When serious overload or flutter is expected to take place, sensors will transmit signals to alter the aerodynamic profile of the lift surface through a servo system to reduce load and to avoid flutter. ACT can reduce the area of the tail and improve the structural efficiency.

ACT is still in the development stage. This new technology adds a control system which introduces the problems of servo system reliability and structure-system stability. A new branch discipline - Aero-Servo Elasticity-was thus created. In the analysis, in addition to the degree of freedom and characteristic parameters of the structure, variables and characteristic

III. Finite Element Method and Structure Method Analysis System /107

Between 1950-1960, Professor J.H. Argyris, M.J. Turner and R.W. Clough introduced the theoretical basis for analyzing a complicated aeronautical structure with a computer. In addition, they came up with specific programs and established a finite element method for engineering applications. Because of its suitability and effectiveness, this method has been rapidly developed since its inception. It has already become an independent discipline. Its application has greatly exceeded the domain of structure analysis. In analyzing the structure of flight vehicles, the finite element method had been successfully applied to large complicated structures such as the Apollo Lunar landing vehicle, Columbia space shuttle and Boeing 747 jumbo jet. In addition to linear elasticity problems, a great deal of progress has been made in elastic plasticity, stability, major deformation, viscoelasticity, thermal stress, creep, vibration, dynamic response, fracture, fatigue cracking, temperature field, fuel swaying in the tank, noise response and flutter analysis. The finite element method has already become a routine analysis for the structure design of vehicles. It provides data in the evaluation of airworthiness as well as the inspection of new planes. This method is still being developed. In the structure analysis of a flight vehicle, leading edge problems such as main strain, instantaneous response, fatigue and cracking, and interaction between the structure and other media are yet to be investigated.

In the early stage of development, computer programs used in the finite element method were compiled in response to specific problems. They are not generalized programs. As the scope of the finite element method broadened, computer programs were perfected due to accumulation of experience and improvement of computation methods. In addition, the finite element method is suited for standardization because it can be generalized. There are many small generalized programs available. Since the late sixties, some large generalized systems began to be created as

CADAM also includes a series of production and manufacturing programs.

Overall structure analysis was initially introduced in the early 1960's. A computer program system is created with advanced structural analysis and optimization. It includes:

- (1) a finite element analysis program
- (2) a generalized optimization program
- (3) user provided supplemental programs, including
 - (a) design variables - such as cross-section, overall geometric size
 - (b) target function - such as weight,
 - (c) constraints - such as stress, displacement, yield, and vibration.

For example, the PROSSS program at NASA-Langley center includes:

SPAR - a finite element analysis program

CONMIN - an optimization program with constraints

It is used on the CDC-NOS computer.

The use of the structural optimization method did not catch up with theoretical developments because specific programs are ineffective, inconvenient and not quite suitable. In the early seventies, it was discovered that the amount of computer time required to calculate the variables was too high. People turned to stepwise design optimization programs.

The ACCESS1 (Approximations Concept Code for Efficient Structural Synthesis) program developed by the University of California in the United States used an improved approximation concept. It includes specifying the relation between design variables, eliminating constraints and approximation analysis to obtain a series of small volume mathematical planning problems. However, the major design features are maintained. The final optimization is achieved through step-by-step improvements. In ACCESS1, in addition to CONMIN, NEWSUMT is also used. It is a frequently used program for optimization without constraints. It involves a penalty function and modified Newtonian method.

Currently, overall structure analysis must be extended to larger structures with more variables.

accurate results, as well as to facilitate iterative designs. This type of system is up to 40 times more effective economically as compared to a conventional design process.

Lockheed in the United States began in 1965 to establish the first software system which was put in place in March 1966. It was a design software package including many analytical systems. It could be used on-line in series as well as in batches. These systems could perform graphics design, structural analysis and data processing for certain steps. CADAM has a graphics terminal. It is equipped with light pen control, keyboard control, function key control or A/D control for input. As for output devices, X-Y plotters, microfilm, digital control tape, printed reports and forms are used. The areas to be developed include large color display and human-machine sound interaction.

/106

CADAM had been used in the development of the L-1011 TriStar, S-3A Viking and many spacecraft. Furthermore, it was used in the appearance design for more than one half of Lockheed's aircraft. The entire system has 90 displays, 4 main-frame computers, and 6 rooms. It includes IBM 2250, IBM 3250, Adages and Vector Generals. CADAM has already been used by 50 companies. Furthermore, independent studies and program development are still in progress, including SURFACE DESIGN, NETWORKS, KINEMATICS, etc.

In the conception design stage, the CADAM TRANSLATE program may be used to shift the relative positions of the wings, engines and tail within seconds. Many combinations are listed. An advanced overall technical evaluation program ASSET (Advanced Systems Synthesis and Evaluation Technique) can be used to determine the performance and cost of various layouts.

In the preliminary design stage, in addition to overall layout and geometry design, structure arrangement and detail design are also carried out to separate main structure components and their weight data. The program MESH is used to establish a finite element model and the program DETAIL is used to evaluate individual components.

In the transonic region, because of decreasing flutter rate (ram), a "transonic indentation" is created. For most modern aircraft, serious flutter occurs in the transonic region. Therefore, accurate analysis of transonic flutter is an urgent problem in the design of an aircraft.

Up to date, there is not a rigorous transonic unsteady aerodynamic wing. Designers are required to rely on empirical correction. Or, results of transonic wind tunnel experiments are directly used to determine the transonic flutter characteristics of an aircraft.

As computers are rapidly developed, the investigation of transonic unsteady aerodynamic calculation methods becomes feasible.

The studies on transonic unsteady aerodynamic calculation methods are progressing along two different, but inter-related avenues.

One approach may be called the "accurate method", which seeks the solutions to the transonic small perturbation equation, the full potential equation and even the Navier-Stokes equation. The problem of this method is the workload is too large. It will be very difficult to be rapidly used in the engineering flutter analysis of a three-dimensional wing. However, only this method can possibly treat the transonic problem rigorously, especially involving shock wave and viscosity. The other way is the "engineering method" such as the Cunningham's configuration method, Liu's mixed nuclear function method, and the integration method introduced by Voss and Hounjet. In summary, the idea is to find a transonic unsteady aerodynamic calculation method which has far less workload than the "accurate method" and can be quickly used in the engineering flutter analysis of three-dimensional wings.

The method adopted by the Institute of Aerodynamics of China is to use a time integration method to solve the transonic low

frequency small perturbation equation. Small perturbation theory is used to capture shock waves. In addition to the conventional ADI method, a new format is introduced in view of the fact that the accuracy will be affected because some added terms cannot be eliminated when the ADI method is used in three-dimensional cases.

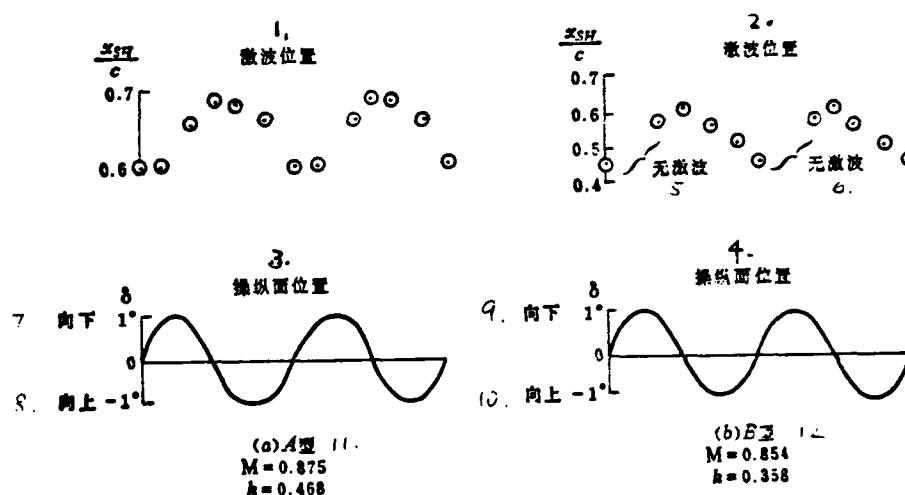


图1 后缘操纵面振荡时的激波运动

Fig.1 Shock movement on a NACA 64A006 airfoil

with oscillating trailing edge flap

13. x_{SH} —激波位置到前缘的距离; C—弦长; δ —操纵面偏度; M—马氏数; h —减阻效率。

Figure 1. Shock Movement on a NACA 64A006 Airfoil With Oscillating Trailing Edge Flap

- Key:
1. shock wave position
 2. shock wave position
 3. flap position
 4. flap position
 5. no shock wave
 6. no shock wave
 7. facing down
 8. facing up
 9. facing down
 10. facing up
 11. type A
 12. type B
 13. distance from shock wave position to leading edge

14. arc length
15. deviation of control plane
16. Mach number
17. decrement frequency

There is a frequency upper limit in the use of the low frequency small perturbation equation. In order to expand the allowable frequency range, terms related to k are maintained while those related to k^2 are omitted in the expressions for pressure coefficient as well as surface and trail conditions. / 114

Many actual cases were calculated using this method. Figure 1 shows the shock wave motion of the NACA 64A006 wing with a $1/4$ arc length trailing edge flap when the flap is oscillating sinusoidally. From the figure one can see that this method is capable of simulating two different shock waves (types A and B) observed experimentally by Tijdeman.

III. The HAJIF-II System and Its Applications

HAJIF-II is a dynamic analysis system for aircraft structures developed by the Institute of Aeronautics of China^[1]. It is capable of calculating the characteristic dynamic features of aircraft with active control systems, as well as the effect of flutter and gust. In the calculation, 99 substructures may be used. The number of degrees of freedom for each substructure can reach 7000. Each unsteady aerodynamic calculation can be divided into 300 blocks. 50 states may be used in calculating the response of flutter and gust.

The system allows the mixed use of topological descriptions created by manually collected and automatically generated data with flexibility. In order to improve the efficiency, a modified super matrix method is used to handle the rigidity and mass matrices. In addition, a new simultaneous iteration method was used to solve the real characteristic problem.

The system includes two major factions of morphological technology - the fixed boundary method and free boundary method. In the free boundary method, the "quasi-constraint form" and "quasi-

fixed boundary form" concepts were used to unify the free boundary method with the fixed boundary method. Furthermore, the "imaginary structure" concept was used to find the flexibility matrix for the free structure. The "characteristic direction" (i.e., approximate value obtained by a few iterations) was used to replace the precise major form of the substructure in order to improve the efficiency of the calculation.

This system was used to compare the efficiency and accuracy of the free boundary method with those of the fixed boundary method through 4 different models. Model 1 is a triangular wing with 858 degrees of freedom. It is divided into three substructures with 384, 294 and 252 degrees of freedom, respectively. Model 2 is a triangular wing with 2 external stores. There are 1200 degrees of freedom in total. It is also divided into 3 substructures with 858, 180 and 186 degrees of freedom, respectively. Model 3 is a simplified model consisting of a straight wing, fuselage, tail and external store. There are a total of 138 degrees of freedom. It is divided into four substructures with 33, 39, 39 and 36 degrees of freedom, respectively. Model 4 is a combination of a straight wing, fuselage and tail. There are 882 degrees of freedom. It is divided into 6 substructures with 180, 180, 180, 180, 150 and 150 degrees of freedom, respectively.

It was demonstrated that both methods have comparable accuracy. But, there is a large difference in efficiency, as shown in the following table:

1. 模 型		1	2	3	4
2.	总自由度数	858	1200	138	332
3.	子结构数	3	3	4	6
4.	总界面自由度数	66	24	9	114
5. CPU (秒)	6. 全结构	710	1109	56	517
	7 自由界面法, 使用“特征方向”	815	944	115	316
	8 固定界面法, 使用“特征方向”	438	585		191

Key: 1. model
2. total degrees of freedom
3. number of substructures
4. degrees of freedom on the boundary
5. CPU (sec)
6. total structure
7. free boundary method, using "characteristic direction"
8. fixed boundary method, using "characteristic direction"

Overall, the fixed boundary method is obviously more effective in cases compared.

IV. The YIDOYU-I System

/115

YIDOYU-I^[2] is a multiconstraint design optimization system based on non-linear mathematical planning developed by the Institute of Aeronautics of China. It is capable of performing full stress design optimization of a structure. A design can be optimized under the minimum dimensional constraint when conditions for stress, displacement, frequency, flutter and static aeroelastics are fully or partially met.

The system can optimize a design for the following airfoil: finite element model with ≤ 3000 degrees of freedom, static external load number ≤ 20 , degrees of freedom of the dynamic model ≤ 200 ,

flutter analysis statis ≤ 20 and design variables ≤ 100 .

The system uses an analytical method to calculate the generalized displacement, stress, flexibility coefficient, inherent vibrational characteristics, flutter velocity, and derivatives of static aeroelastic characteristics. The sequential unconstraint optimization method (SUMT) was used. The penalty function used is a second order expansion of the internal penalty function. The unconstraint extremum can be solved by either the gradient method, the conjugate gradient method, Newtonian method, DFP method, or BFGS method. One dimensional searching can be done by either the parabolic method or the gold division method.

V. Experimental Study of External Store Flutter

Modern aircraft are generally required to carry a large number of external stores. Therefore, external store flutter is an urgent problem.

In recent years, systematic experimental studies have been conducted on external store flutter. Shengyang Aircraft Corporation performed wind tunnel experiments on external stores located at the wing tip and under the wing using flexible hangers. Different span and chord positions as well as hanger pitches, yawing and sway flexibility were tested.

Experimentally, there are three different types of flutter, i.e., (1) flutter causing the bending and twisting of the wing, (2) flutter causing the bending of the wing surface and pitching of the external store, and (3) flutter causing the swaying of the external store and yawing.

For an external store under the wing at mid wing span, the wing is almost bent by the pitch frequency of the external store when the pitch rigidity of the external store is low. In this case, wing bending and twisting flutter begin to appear. The flutter rate is comparable to or higher than that without the external store (See Figure 2). When the pitch rigidity of the external store increases, under the pitch frequency the wing is near a twist type. The wing surface is bent and the external store flutters. The flutter rate is usually lower than that without an external store. Furthermore, the flutter rate will not increase significantly when the pitch rigidity increases.

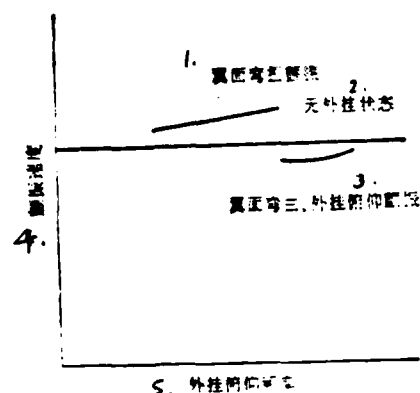


Figure 2. Transition of the type of external store flutter

- Key:
1. wing twisting flutter
 2. no external store
 3. wing bending and external store pitch flutter
 4. flutter rate
 5. pitch frequency

For an external store under the wing at an outside span, it is very difficult for the wing to bend and twist due to flutter at normal flexibility of the external store. There is only wing bending and external store pitch flutter.

With regard to external store yawing and sway, the external store will yaw and sway due to flutter in certain combinations of yawing and sway flexibility. However, new coupled flutter between the wing surface and the external store was not found in the experiment. The effect of external store yawing and sway flexibility on the wing bending and external store pitch flutter is generally not very apparent.

In the experiment, we also observed the effect of the shift of the center of gravity of the external store, as shown in Figure 3. In conclusion, the effect of a center of gravity shift is not obvious.

As for external stores at the wing tip, there are also similar flutter problems. The transition is also determined by the fact of whether the wing is bent or twisted at the pitch frequency. /116

VI. Active Flutter Suppression

Active flutter suppression is an active subject in aeroelasticity. There are large numbers of papers reporting the progress in this field each year. They include studies based on aerodynamic energy methods, classical and modern cybernetics, adaptive control systems and digital control systems. Americans and Europeans are still conducting wind tunnel experiments on these problems. In addition, there are manned and unmanned aircraft experiments.

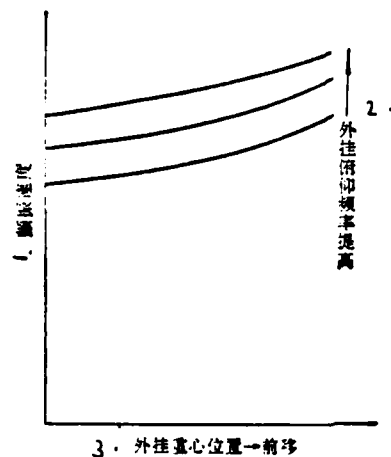


Figure 3. Effect of chordwise position of center of gravity of flexibly mounted external store

- Key:
1. flutter rate
 2. center of gravity of external store shift → forward
 3. increasing external store pitch frequency

The future of active flutter suppression is basically dependent on the reliability of the system. In this premise, it may first be used to suppress the flutter of an external store. As described above, a modern aircraft carries more types and combinations of external stores. In this case, certain external store combinations cannot satisfy the operational requirements. It is not cost effective to strengthen the wing structure for these specific combinations. Therefore, an active suppression technique is used to solve the flutter problem.

The use of an active suppression technique to increase the flutter rate of the wing may also be considered as use of the structural rigidity to ensure the flutter speed is not less than the maximum flying speed. Then, the flutter speed is increased

by 15% using an active suppression technique to satisfy the excess flutter speed requirement.

In summary, the flutter suppression system is used in very few flight conditions. Furthermore, the safety is assured by increased reliability of the system itself.

In recent years, many organizations in China are studying the active suppression of flutter. For example, Nanjing Institute of Aeronautics and Astronautics, Beijing Institute of Aeronautics and Astronautics and Northwest Polytech University are studying cybernetics, and Nanjing Institute of Aeronautics and Astronautics introduced an improved unsteady aerodynamic fitting method.

Chengdu Aircraft Corporation finished an active flutter suppression experiment on a dynamic model in a low speed wind tunnel. The model is a 60° triangular wing with a trailing edge for active control. The model is equipped with a dc torque motor /117 for active control. In order to ensure that the sensor can detect the flutter to the extent possible, the sensor is placed near an indifferent nodal line so that other irrelevant motion cannot be detected and new flutter will not be triggered. In addition, trap filters and low pass filters are used to further eliminate unrelated effects.

In the experiment, a gain adjuster and a phase adjuster were used. The Bode diagram was used to describe the Nyquist guideline. The gain and phase were adjusted to satisfy the stability requirements.

It was experimentally demonstrated that the active flutter suppression system could increase the flutter speed by 40%.

VII. Conclusions

This paper discussed new progress in aeroelastic research in China. Although there is a large gap as compared to advanced levels in the world, however, we are initiating studies in many areas. We worked hard, made some progress and reached a considerable standard. This paper is dedicated to the twentieth

anniversary of the Aeronautic Society of China. Furthermore, the authors of cited references are deeply appreciated.

References

- [1] Edited by Guan De, Manual for Dynamic Analysis System of Aircraft Structure-Theory of HAJIF-II, China Aeronautical Technical Literature HJL-83005.
- [2] Ye Gejia, Lin Fenhe and Liang Xiyu, Introduction to the Multiconstraint Design Optimization for Aircraft Structure-YIDOYU-I, International Aeronautics, 1983. 7.

NEW DEVELOPMENTS OF AEROELASTIC RESEARCH

Guan De

(Shengyang Aircraft Corporation)

Abstract

Some new developments of aeroelastic research in China are reviewed, which include calculation of unsteady transonic aerodynamic forces. HAJIF-II, a program system for dynamic analysis of aircraft structures and its application, YIDOYU-1, a program system for structural optimization with multiconstraint, experimental investigation on external stores flutter and active flutter suppression.

Scene Matching and its Application to Aerospace
Electronic Systems

/118

Sun Zhongkang *
(Changsha Institute of Technology)

Abstract

Several essential problems in scene matching technique are reviewed; measures of similarity (MAD, MSD, PROD, NPROD, Pair Functions etc.) are outlined; fast search methods (resolution from coarse to fine, quantization from coarse to fine, feature extraction, modified SSDA etc.) are introduced; probability of acquisition for max. or min. algorithm is given; preprocessing of images (filtering, restoration, whitening etc.) is considered; geometrical distortion (synchronization error, rotation, scale factor, perspective distortion) and its effects are analyzed, and the methods for overcoming such effects are presented.

I. Introduction

Following the guiding ideology of active defense, military aircraft may dodge the threat of the ground fire by utilizing mountains and the hilly terrain and slip into enemy territory at low altitude (several tens of meters) following concealed paths to avoid the detection of radar, and attack the fixed or moving targets on the ground surface. This approach improves greatly the survivability, the attacking ability and the unexpectibility of the military aircraft in the battle. The technique of following and dodging along the terrain contour using pre-stored topographic maps is the key factor for improving the survivability and the assault ability of the military aircraft^[1].

The inertial navigation system of the aircraft is a necessary instrument for long distance navigation^[2]. It is also

* Received in December 1983

the central portion of the weapon aiming and releasing system of the aircraft.

It has the advantages of independence, concealment, all weather, all seasons, anti-interference and high momentary precision. However due to the drift of the gyroscope and the error in accelerometer, the deviation of the inertial navigation system accumulates with time. According to the principle of navigation by ground objects, the deviation of the inertial navigation system or the gyroscope can be corrected instantly using such information as the ground terrain, maps, features of the ground objects, or the geophysical fields. This composite navigation system can eliminate the accumulative deviation of the inertial navigation system. It can also maintain the capabilities of independence, concealment and anti-interference. Utilization of the ground information is realized with a scene matching technique.

The development of the "hit and run" type target homing warheads can improve the survivability and the maneuverability of the aircraft during air-to-air or air-to-ground assault. During air-to-ground battle, it is necessary to identify or track the target among the ground objects. Due to serious cluttering of the ground objects, it is very difficult to use the general technique with radar for tracking the target. The scene (photographed by millimeter wave, infrared rays, laser or visible light) matching technique makes it possible to overcome the above mentioned difficulty. It can provide the ability of recognition, tracking and target homing and enables the aircraft to do "hit and run".

Obviously, the scene matching technique can greatly improve the survivability, assaultability and maneuverability of the aircraft, improve the navigation and increase the accuracy in releasing the weapons. This technique has been practically applied in guiding the cruise missile and ground-to-ground missile, locating the orbits of the satellites, and determining the changes of the targets on the remotely sensed pictures.

II. Principle and Technique of Location by Scene Matching /119

With the available topographic or surface scene maps of the flying area, which have one-to-one correspondence regarding the geographic position, the position of the map or the terrain contour recorded by the aircraft during flight can be located by comparison with the pre-stored topographic maps of the flying area. The actual geographic position of the aircraft during recording of the map can then be determined. This technique of position location is the scene matching technique.

There are two basic methods of scene matching for position location: terrain matching (one dimensional), and map matching (two dimensional). The former is actually a special case of the latter. Figure 1 illustrates the principle of both matching techniques. Figure 1(a) shows the topographic map of the flying area and the numerically coded topographic map which has been divided into $(M \times N)$ grids.

1. Feature Matching by Invariant Moments^[8]

With an amplitude distribution, $F(i, j)$, of the image the various step moments and the central moments can be defined as:

$$m_{pq} = \sum_i \sum_j i^p j^q F(i, j) \quad (18)$$

$$\mu_{pq} = \sum_i \sum_j (i - \bar{i})^p (j - \bar{j})^q F(i, j) \quad (19)$$

where $\bar{i} = \frac{m_{10}}{m_{00}}, \bar{j} = \frac{m_{01}}{m_{00}}$

With $\eta_{pq} = \frac{\mu_{pq}}{\mu_{00}^q}, r = \frac{r+q}{2}$, the seven invariant moments $I_k, k = 1, 2, \dots, 7$ can be obtained. An example of a set of the invariant moments is given in the following:

$$\left. \begin{aligned} I_1 &= \eta_{20} + \eta_{02} \\ \vdots \\ I_7 &= (3\eta_{12} - \eta_{13})(\eta_{30} - \eta_{12})[(\eta_{30} + \eta_{12})^2 - 3(\eta_{21} + \eta_{03})^2] \\ &\quad + (3\eta_{21} - \eta_{13})(\eta_{21} + \eta_{03})[3(\eta_{30} + \eta_{12})^2 - (\eta_{21} + \eta_{03})^2] \end{aligned} \right\} \quad (20)$$

The seven invariant moments of the image X and the corresponding subimage of $Y, I_{xk}, I_{yk}, k = 1, 2, \dots, 7$, are calculated. The similarity between the two groups of the invariant moments is then evaluated using the calculation method of similarity measure, that is

$$\phi(l, m) = \frac{\sum_{k=1}^7 I_{xk} I_{yk}(l, m)}{\left[\sum_{k=1}^7 I_{xk}^2 \right]^{1/2} \left[\sum_{k=1}^7 I_{yk}^2(l, m) \right]^{1/2}} \quad (21)$$

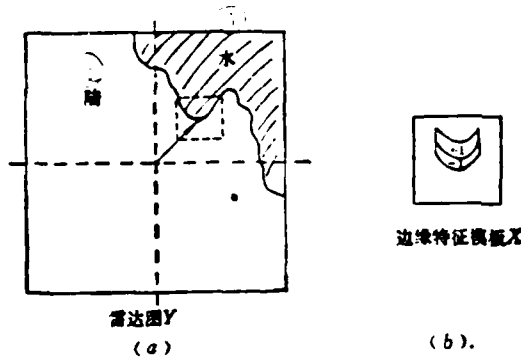


Figure 6. Edge Feature Template Matching

Key: 1. water
2. land

(a) radar image Y (b) Template X

squares or the method of generalized inverse matrix. With the matrix T available, geometrical restoration of the whole image can be processed.

3. Matching Calculation with Multiple Subimages^[7]

Since the influence of the geometrical distortion on the small scale is less than that on the large image, dividing the big image into small subimages for scene matching can reduce the influence of the geometrical distortion on the quality of the matching process. However, since the correlation peak of a small subimage is low and broad, the accuracy of the position matching will be affected. After the position values are obtained by matching with many subimages, the actual location can be estimated by the least squares method. This approach improves significantly the accuracy of the location matching.

III. Matching by Features

The sensed image X and the prestored image Y are usually recorded at different times, under different weather, season and geometrical positions and by different methods (such as radar, infrared and visible light). There is always some difference in quality of the images with geometrical distortion. It is difficult to carry out directly the scene matching between X and Y with good quality assurance. Matching by features which are not easily changed by the geometrical distortion or by the difference in the quality of the images has been widely employed recently. /126

The features of the image to be matched can be the amplitude distribution, the frequency spectrum or the geometrical features such as surface, lines, points, edges, apical points, laminations, etc. Several commonly used methods of matching by features are described in the following.

The methods for correcting the geometrical distortion are listed in the following:

1. Calculation with methods which are insensitive to the geometrical distortion such as Fourier phase spectrum calculation on low pass filtered wave.^[6]

With Fourier transformation, the calculation is insensitive to such geometrical distortions as rotation and scale factor.

2. Geometrical restoration

The distorted sensed image X can be restored geometrically to near the original image X . The similarity to the prestored image is then measured after the restoration. This method can preserve most of the original matching quality.

The linear correlation between the actual three dimensional coordinates of a known object (x_1, y_1, z_1) and the coordinates of the object under the conditions of synchronization error, rotation, scale factor and perspective distortion (x_2, y_2, z_2) can be written as follows based on the generalized coordinate system:

$$\begin{bmatrix} wx_2 \\ wy_2 \\ wz_2 \\ w \end{bmatrix} = \begin{bmatrix} T_{11} & T_{12} & T_{13} & T_{14} \\ T_{21} & T_{22} & T_{23} & T_{24} \\ T_{31} & T_{32} & T_{33} & T_{34} \\ T_{41} & T_{42} & T_{43} & T_{44} \end{bmatrix} \begin{bmatrix} x_1 \\ y_1 \\ z_1 \\ 1 \end{bmatrix} \quad (17)$$

where w is a scale factor. T_{44} in the transformation matrix T reflects the geometrical scale factor of the whole image. The 9 elements at the upper left corner of the matrix reflect the rotation distortion. T_{14} , T_{24} , T_{34} reflect the rotation distortion. T_{41} , T_{42} , T_{43} reflect the perspective distortion. If the values of the elements in the transformation matrix are available, the coordinates of the corresponding undistorted position of the object can be obtained from the geometrically distorted coordinates (x_2, y_2, z_2) by solving the above group of linear equations. With several recognition points or control points, the corresponding coordinates can be obtained manually or automatically and over 16 linear equations with the elements, T_{ij} , as unknowns can be listed using the relation (17). The values of the elements T_{ij} can be obtained by the method of least

$D(i, j)$ where

$$D(i, j) = \begin{pmatrix} \rho_o \rho_R & -\rho_o(1 + \rho_R^2) & \rho_o \rho_R \\ -\rho_R(1 + \rho_o^2) & (1 + \rho_o^2)(1 + \rho_R^2) & -\rho_R(1 + \rho_o^2) \\ \rho_o \rho_R & -\rho_o(1 + \rho_R^2) & \rho_o \rho_R \end{pmatrix} \quad (16)$$

The convolution output is the sharpened image.

Geometrical Distortion and Improvement

The sensed image X obtained from the aircraft is distorted from the corresponding subimage of the prestored image Y due to the influences of the posture of the carrier, the distance from the object and the angle of photographing. Figure 5 illustrates various distortions due to synchronization error, rotation, scale factor and perspective distortion. Some or the major portion of the distorted sensed image X exhibits inconsistency with the corresponding subimage of the prestored image Y , which broadened the correlation peak and reduces the probability of acquisition of the correct match, P_c and decreases the quality of matching. The extent of the loss of matching quality due to geometrical distortion increases with the size of the image. It is necessary to consider the effect of the geometrical distortion in practical applications.

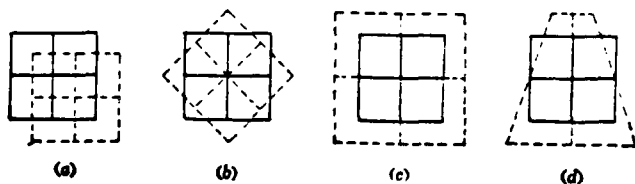


Figure 5. Geometrical Distortion

/125

Key: (a) synchronization error
(b) rotation
(c) scale factor
(d) perspective distortion

where the coefficient K is

$$\text{erf} K = 2 \left[\left(\frac{1}{2} \right)^{\frac{1}{G-1}} - \left(\frac{1}{2} \right) \right] \quad (15)$$

The expression of the probability of correct match P_c indicates that the probability increases with increasing values of the absolute difference $|\phi_M - \phi_{N.M}|$ of the average measures at the matched and the unmatched positions and with decreasing scattering of the measure, σ_0^2 , at the matched position. The distribution of the two dimensional measures is a two dimensional correlation function. The probability of the correct match, P_c , increases when the function is more close to the shape of a tack or an up-side-down tack, or with increasing sharpness of the correlation peak or valley. It is obvious that the shape of the correlation function depends on the characteristics of the images X and Y. The scattering variance σ_0^2 of the correlation peak also depends on σ_n^2, σ_y^2 , etc.

The probability P_c indicates the reliability of the matched position. The reliability may also be measured by the difference, $|\phi_M - \phi_{M.N}|$.

Preprocessing

If the correlation function of the sensed image X has a broader or flatter correlation peak and the image has high noise n, it gives a lower probability of correct match and lower reliability of matching. For increasing the probability P_c , the image X can be preprocessed by filtering to compress the noise. The image can also be treated with a whitening process to make the correlation function more similar to the shape of a tack and to sharpen the correlation peak.

The preprocessing methods of wave filtering can be "Wei Na" (Wigner ?) restoration filtering, Kalman filtering or mid-value filtering^[12]. The method for sharpening the correlation peak can be a statistical marginal checking treatment^[12]. Convolution calculations are carried out on the filtered image X (i,j) with the two dimensional pulse effect

random quantities and the event of obtaining the limit value of the measures is a random event. In the searching process, value at the matched position should be a maximum or minimum value and the values at the un-matched (G-1) positions should not be a limit value. The probability of correct match, P_c , is defined as follows:

Key: 1,2 calculation

$$\left. \begin{aligned} P_c &= \int_{-\infty}^{\infty} p(\phi/M) \left[\int_{-\infty}^{\phi} p(\phi'/N \cdot M) d\phi' \right]^{G-1} d\phi, \text{ max 算法 } (1) \\ P_c &= \int_{-\infty}^{\infty} p(\phi/M) \left[\int_{\phi}^{\infty} p(\phi'/N \cdot M) d\phi' \right]^{G-1} d\phi, \text{ min 算法 } (2) \end{aligned} \right\} \quad (13)$$

where $p(\phi/M)$ and $p(\phi'/NM)$ are the distribution functions of the measures of ϕ and ϕ' at the matched position (M) and the unmatched (N.M) positions respectively.

If the image Y is the equilibrated normal random field $N(0, \sigma_y^2)$ and the image X is the corresponding subimage in Y with the addition of noise n, where n is the normal random field $N(0, \sigma_y^2)$, the probability P_c of the correct match can be expressed as

$$P_c = \frac{1}{2} + \frac{1}{2} \operatorname{erf} \left\{ \frac{|\bar{\phi}_M - \bar{\phi}_{N.M}|}{\sigma_0} - K \frac{\sigma_j}{\sigma_0} \right\} \quad (14)$$

where $\phi_M \sim N(\bar{\phi}_M, \sigma_0^2)$ is the measure of ϕ at the matched position; and $\phi_{N.M} \sim N(\bar{\phi}_{N.M}, \sigma_j^2)$ are the measures of ϕ' at unmatched positions ($j \neq 0$). The average values, variances $\bar{\phi}_M, \bar{\phi}_{N.M}, \sigma_0^2, \sigma_j^2$ can be expressed by σ_y^2, σ_n^2 and the number of independent elements, N, of the image, as shown in the following equations:

Key:

$$\left. \begin{aligned} \sigma_0^2 &= \left(1 - \frac{2}{\pi}\right) \frac{\sigma_n^2}{N} \\ \sigma_j^2 &= \left(1 - \frac{2}{\pi}\right) \frac{2\sigma_y^2 + \sigma_n^2}{N} \end{aligned} \right\} \text{MAD 算法 } (1) \quad \begin{aligned} &1. \text{MAD calculation} \\ &2. \text{PROD calculation} \end{aligned}$$

$$\left. \begin{aligned} \sigma_0^2 &= \frac{\sigma_y^2}{N} (2\sigma_y^2 + \sigma_n^2) \\ \sigma_j^2 &= \frac{\sigma_y^2}{N} (\sigma_y^2 + \sigma_n^2) \end{aligned} \right\} \text{PROD 算法 } (2)$$

position having the accumulative sum less than the threshold T with a highest progressive number k . The search process is accelerated since the calculations on the unmatched positions are significantly reduced. If the absolute deviation of the corresponding subimage and the statistical characteristics of the sequential accumulative sum can be obtained and a monotonic increasing threshold series $T(k)^{[5]}$ of the matching target with fixed characteristics is available, the speed of the matching process will be further improved (Figure 4).

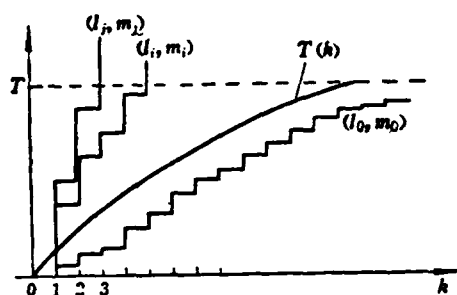


Figure 4. Sequential Similarity Detection With Threshold $T(k)$

The increase in searching speed depends on the reduction of the number of positions to be searched and the simplicity of the calculations. If the pretested information on the statistical characteristics of the position corresponding to the sensed image is available, the number of positions to be searched can be reduced by using the searching path starting from high probability to low probability with position matching determined by quantitative thresholds.

Probability of Acquisition of Correct Match

Since random errors exist in all elements of both the prestored image Y and the sensed image X , the measures of the similarities, ϕ , obtained from the searching process are all

The thresholds set for each level, T_i , $i = 1, 2, \dots, n$ are for the purpose of eliminating the positions having low similarities. The values of the thresholds should be selected to effectively reduce the searching range without missing any matched position. In general,

$$T_n > T_{n-1} > \dots > T_2 > T_1$$

In the n -th relation process, the matched location is the position having the maximum relation value, ϕ_n . Since the correlation calculations are carried out by addition and the screening process proceeds with the amplitude from coarse to fine, the searching speed is greatly improved.

3. Search with Regions having Special Features

If the prestored image Y ($M \times M$) can be divided into subregions having distinguishable characteristic values (such as /123 average altitude, gradation variance), the location of the sensed image X ($N \times N$) can be searched by matching the characteristic value of the X image with the corresponding values of the subregions in the Y image. The range of search is greatly reduced and the searching speed is increased.

4. Fast Search by Sequential Similarity Detection

With MAD calculation, the measure at the matched position (l_0, m_0) is a minimum, ϕ_{\min} , and the sum of the absolute deviations of other unmatched positions (l_i, m_i) should be larger than ϕ_{\min} , that is

$$\phi(l_i, m_i) = \sum_{i,j} |x_{ij} - y_{i+l_i, j+m_i}| > \phi_{\min} \quad (12)$$

An estimated value of ϕ_{\min} and a threshold $T = \phi_{\min}$ can be obtained from the statistical data of images X and Y . When the calculated accumulative absolute deviation on a particular position in image Y in regard to image X is larger than the threshold T , the position cannot be the matched position and another position should be selected for evaluating the similarity. The matched position is finally determined to be the

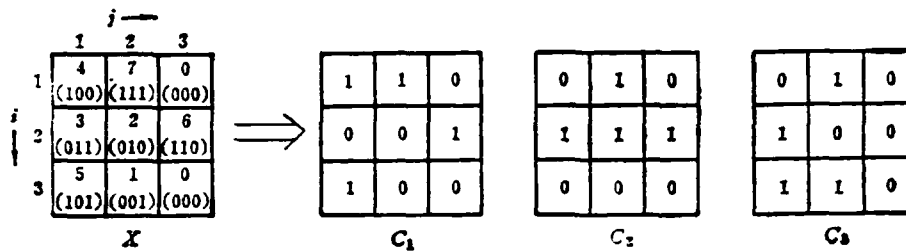


Figure 3. A Set of Subimages With Different Quantization

The subimages represent individually the structure of the amplitude distribution of the image X. Matching calculations between C_1 and image Y are carried out and the similar positions are determined based on the threshold T_1 , which gives the following equation:

$$\phi_1(l, m) = \sum_{i,j} y_{i+l, j+m} - \sum_{i,j} y_{i+l, j+m-1} > T_1 \quad (9)$$

$$C_1(i, j) = 1 \quad C_1(i, j) = 0$$

where the calculations are only carried on +1 (corresponding to binary 1) and -1 (corresponding to 0) by multiplication. It converts the multiplication into addition. The second level matching calculation is carried out on those positions (l, m) with $\phi_1 > T_1$ using the finer structure C_2 . The positions with higher similarity are determined by the threshold T_2 , and

$$\phi_2(l, m) = \phi_1(l, m) + \frac{1}{2} \left\{ \sum_{i,j} y_{i+l, j+m} - \sum_{i,j} y_{i+l, j+m-1} \right\} > T_2 \quad (10)$$

$$C_2 = 1 \quad C_2 = 0$$

The above process is repeated on the positions with $\phi_2 > T_2$ using the further finer structure C_3 . Similar calculations are continued for n times until the position having the highest similarity is obtained. The final measure of the correlation is:

$$\phi_n(l, m) = \sum_{k=1}^n \frac{1}{2^{k-1}} \left\{ \sum_{i,j} y_{i+l, j+m} - \sum_{i,j} y_{i+l, j+m-1} \right\} \quad (11)$$

$$C_k = 1 \quad C_k = 0$$

$$\begin{aligned} Y_k &: \left(\frac{M}{2^k} \times \frac{M}{2^k} \right) \\ X_k &: \left(\frac{N}{2^k} \times \frac{N}{2^k} \right) \end{aligned} \quad k = 0, 1, 2, \dots, L \quad (7)$$

With $k=0$, it gives the original images Y and X . Y_k and X_k are the k -th level low resolution images. The search starts from the images of level L which have the lowest resolution. The total number of positions to be searched are

$$\left(\frac{M}{2^L} - \frac{N}{2^L} + 1 \right)^2 \quad (8)$$

which is 2^{2L} times less than the number of positions to be searched in the original images X and Y , $(M-N+1)^2$. The "similarity" is calculated by a suitable method. Further matching calculations on images of higher level of resolution, Y_{L-1} and X_{L-1} are carried out only on those positions which have the measures of similarity higher than the threshold T_L . Positions of higher similarity are then determined by the new threshold T_{L-1} . The process is continued until the matched position of X in Y is obtained. This is a searching process starting from rough to precision. The precision is determined by the resolution of the /122 image or the band width of the frequency spectrum of the image. It obviously increases the searching speed. The number of levels of the resolution is determined by the frequency spectrum and width of the image (or pretreated image).

2. Stratified Search by Amplitude Quantization Starting from Rough to Precision^[4]

The amplitude of each small element of image X is quantized into n binary bits and the subimages C_1, C_2, \dots, C_n , are constructed as shown in Figure 3 ($n=3$) according to the high or low bit (0, 1) of each element. C_1 represents only the high bits of the binary amplitude values of the elements, while C_3 represents only the low bits of the amplitude of the elements.

influence when the scale of gradation of the image is not available.

The calculation with MAD or MSD is a measurement of "distance". The matched position with a minimum value of $\phi(l,m)$ is the position having the highest similarity. The calculation is quite simple. The calculation methods with PROD and NPROD are measurements of the "relative" values. The position with maximum $\phi(l,m)$ is the matched position. They require more calculations and have the capability of filtering in matching. They can be applied in conditions of low signal-to-noise ratio.

There are many other methods for calculating the similarity such as the measurement of the "pair function"^[3] of the subimage having equal amplitude, the calculation based on the concept of "estimation", etc.

Search for Matched Position

The similarity of the sensed image ($N_1 \times N_2$) with each sequential position on the prestored image ($M_1 \times M_2$) should be calculated. The matched position is the corresponding position (l,m) having an extreme value of $\phi(l,m)$. The following number of calculations have to be carried out on a total of G positions:

$$G = (M_1 - N_1 + 1) \times (M_2 - N_2 + 1) \quad (6)$$

There are only one matched position and $G-1$ unmatched positions. The search for matched position is obviously time consuming. A fast search is needed for reducing the duration of the matching process. Several methods of fast search are listed in the following:

1. Stratified Search by Frequency Bands Starting from Rough to Precision^[3]

Sequential low resolution images with decreasing resolution are obtained by filtering the prestored image Y ($M \times M$) and the sensed image X ($N \times N$) through low band pass, i.e.,:

(matching calculation) are listed in the following. The symbols used in the equations are shown in Figure 2.

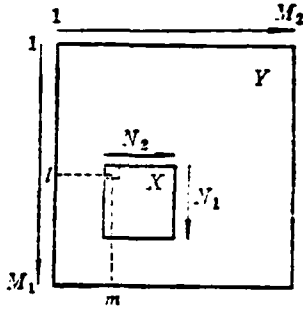


Figure 2. Prestored Image Y and Sensed Image X

Calculation by the mean absolute deviations (MAD):

$$\phi(l, m) = \frac{1}{N_1 N_2} \sum_{i=1}^{N_1} \sum_{j=1}^{N_2} |x_{ij} - y_{i+l, j+m}| \quad (2)$$

Calculation by the mean square deviations (MSD):

$$\phi(l, m) = \frac{1}{N_1 N_2} \sum_{i=1}^{N_1} \sum_{j=1}^{N_2} (x_{ij} - y_{i+l, j+m})^2 \quad (3)$$

Calculation by the product relations (PROD):

$$\phi(l, m) = \frac{1}{N_1 N_2} \sum_{i=1}^{N_1} \sum_{j=1}^{N_2} x_{ij} y_{i+l, j+m} \quad (4)$$

Calculation by the normalized product relations (NPROD)

$$\phi(l, m) = \frac{\sum_{i=1}^{N_1} \sum_{j=1}^{N_2} x_{ij} y_{i+l, j+m}}{\left[\sum_{i=1}^{N_1} \sum_{j=1}^{N_2} x_{ij}^2 \right]^{1/2} \left[\sum_{i=1}^{N_1} \sum_{j=1}^{N_2} y_{i+l, j+m}^2 \right]^{1/2}} \quad (5) / 121$$

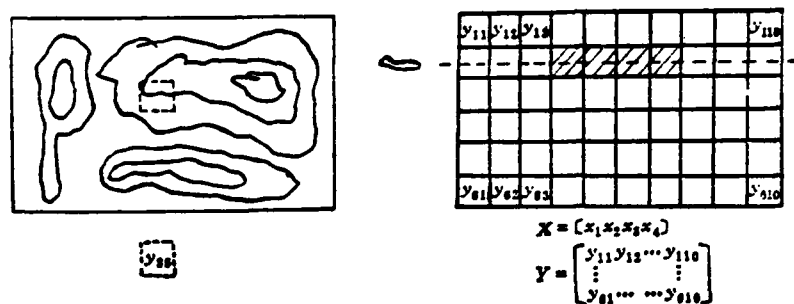
The above calculations can be applied in both one dimensional and two dimensional matching. With bias in the images, the similarity can be measured on the image after subtracting the mean value. The changed portion of the information on the image is utilized. The calculation by the normalized product relations can eliminate the

The vectors of the altitude contour (or real time map), $X = [x_1 x_2 x_3 x_4]^1$, can be measured using the altitude contour meter (consists of radar altimeter) during real time flying. Comparing the recorded vector, X , with the individual position in the prestored and numerically coded image Y , a region in Y which resembles mostly the vector X can be identified. The geographic position of the identified region is the actual position of the aircraft when the altitude contour X was recorded. This is position location by terrain matching. If the pre-stored image is a two dimensional, numerically coded, map of matrix $Y(M_1 \times M_2)$ with various gradations, and the recorded remotely sensed image is the numerical image $X(N_1 \times N_2)$, similar comparison of X with each position in Y can be carried out and the region in Y having the best resemblance to X can be identified. This is the technique of position location by scene matching for determining the actual geographic position of the aircraft when image X is recorded.

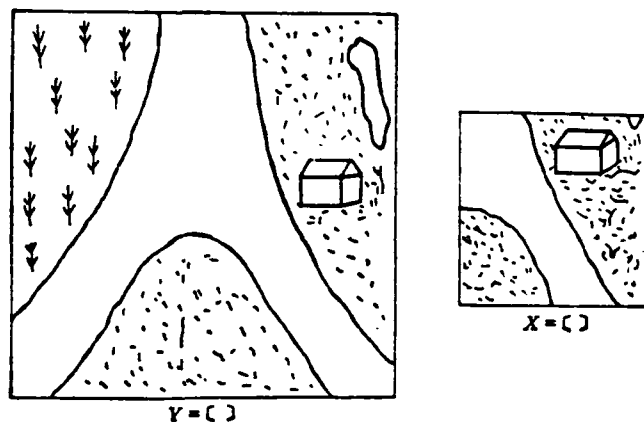
The basic principle of comparing the resemblance of two maps for position location is the same for both the terrain contour matching and the scene matching. The major difference is on the utilization of the surface information (terrain altitude, intensity of the surface radiation) as well as in the number of dimensions of the recorded information. However, various information of the ground surface can be used for position matching depending on the characteristics of the remote sensing equipment.

Measurement of the Similarity

The comparison of the sensed image X with the prestored image Y should be measured by "similarity". Since various errors are introduced in the recording process of the image, there is no perfect match of the image X and the region in image Y . The comparison of image X and the corresponding region in image Y (or to be referred to as subimage) can only be measured by the extent of "similarity". Several measurements of the similarity $\phi(l,m)$



(a)



(b)

Figure 1. Principle of Matching

- (a) Terrain Contour Matching
- (b) Scene Matching

The altitude of each element of the map is represented by the average altitude of the area within the grid, y_{ij} . Therefore the numerically coded topographic map can be represented by the Matrix Y with $(M \times N)$ elements:

$$Y = \begin{bmatrix} y_{11} & y_{12} & \dots & y_{1N} \\ y_{21} & y_{22} & \dots & y_{2N} \\ \vdots & \vdots & \ddots & \vdots \\ y_{M1} & y_{M2} & \dots & y_{MN} \end{bmatrix} \quad (1) \quad /120$$

This type of matching using invariant moments can provide good matching quality even with two images having 45° rotation or a scale ratio of 2:1. The method has been used in matching radar image with photo image.

/127

2. Edge Feature Template Matching [9]

The border of the water and the land is rather clear in radar images and photo images and the matching can be made with edge feature template as shown in Figure 6. Correlation matching calculation can be carried out between the radar image and the template made from a section of the intersection line between water and land. Since the geographical position of the template is available, the corresponding position of the radar carrier can be obtained by matching. The measure of correlation is

$$\phi(l, m) = \frac{\sum_{i=1}^N y_{l,m} - \sum_{i=1}^N y_{i,m}}{N y_{r.m.s.}(l, m)} \quad \text{Key:} \quad (22)$$

1. high
2. low

where the template of +1 region is the highland and the template -1 is the low ground. N_T is the total number of the elements of the edge template. $Y_{r.m.s.}$ is the root-mean-square value of the amplitude of the region in the image corresponding to the template.

3. Line Feature Matching [4]

If the contour of a ground feature can be described by linear lines as shown in Figure 7, the number, directions, lengths and end points of the lines can be used as characteristics for matching. The linear lines can be transformed to dots on a ρ - θ plane surface by Hough transformation. The number of the dots is the number of the lines. The positions of the dots on the plane surface ρ - θ represent the directions of the lines. By matching the dots, the dots of the lines of the ground subject on the prestored image will fall in the neighborhood of the dots of the subject of the sensed image on the ρ - θ plane. A "coarse" match is realized

when maximum number of pairs of dots is obtained. The correct match is then determined by the proportion of the lines of the feature overlapped. At a certain position the number of the corresponding dots on the ρ - θ plane for the lines of the object in both images is a maximum and the proportion of the overlapped lines is also a maximum. This position is the correct matched position.

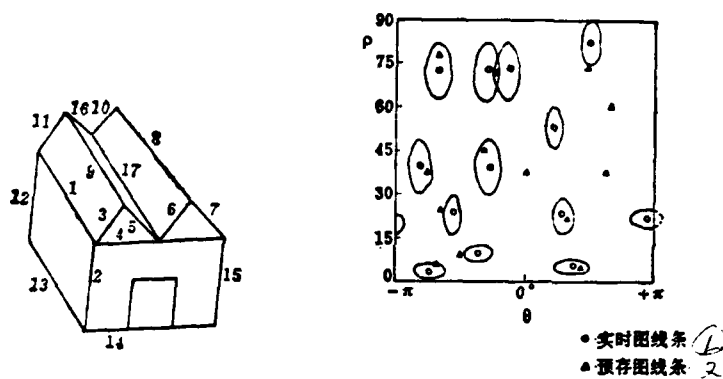


Figure 7. Line Feature Matching

Key: 1. line on the sensed image
2. line on the prestored image

4. Planar Feature Matching [10]

For locating a big building (target) in the image, the intersection point of the two adjacent walls, which are perpendicular to each other, with the ground surface can be employed as a positioning point for aiming. The position of the intersection point of three surfaces can be determined by locating the three surfaces. Using a laser ranging device to measure the distance with azimuth (β) and angle of pitch (ϵ), the distance data $R(\beta, \epsilon)$, which is function of β and ϵ , of any point on the ground object can be obtained. Each planar surface on the ground can be determined using a three dimensional Hough

transformation and the method of histograms. It can be represented by the following equation

$$(\cos \varepsilon_i \cos \beta_i) x_{pi} + (\cos \varepsilon_i \sin \beta_i) y_{pi} + (\sin \varepsilon_i) z_{pi} = D_i \quad (23) \quad /128$$

where x_p , y_p and z_p are the coordinates of a point on the plane surface, and the subscript i corresponds to the i -th planar surface. With more than three in-coplanar surfaces ($i > 3$), the following equation can be applied for estimating the coordinates of the intersection point (x_T, y_T, z_T) ,

$$TX_T = D \quad (24)$$

where $X_T = [x_T \ y_T \ z_T]'$
 $D = [D_1 \ D_2 \dots D_N]'$

and the matrix T is

$$T = \begin{bmatrix} \cos \varepsilon_1 \cos \beta_1 & \cos \varepsilon_1 \sin \beta_1 & \sin \varepsilon_1 \\ \cos \varepsilon_2 \cos \beta_2 & \cos \varepsilon_2 \sin \beta_2 & \sin \varepsilon_2 \\ \vdots & \vdots & \vdots \\ \cos \varepsilon_N \cos \beta_N & \cos \varepsilon_N \sin \beta_N & \sin \varepsilon_N \end{bmatrix}$$

The estimated value can be obtained as

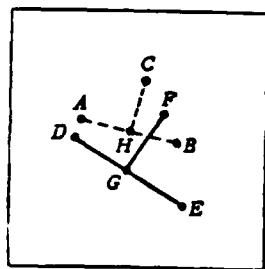
$$\hat{X}_T = T^- D = (T' T)^{-1} T' D \quad (25)$$

where T^- is the pseudo-inverse matrix or the generalized inverse matrix of T .

This method of position location, which utilizes the distance data, the planar surfaces and the apex of the surfaces to determine the position of the aiming point X_T , is basically not influenced by the frequency spectrum of the gradation distribution of the image, the changes of weather and daylight and the geometrical distortions (rotation, scale enlargement.....).

IV. Correlation Tracking with Map Matching^[11]

The accuracy of target homing weapons can be greatly improved by using the technique of correlation tracking with map matching for navigation at the last stage of homing control near the target. Previously, tracking with energy homing was usually employed in air-to-ground battles. Since the clutter noise of the background is usually stronger than the energy of the signal

$$K_1 = \frac{HB}{AB} \quad (26)$$


When the target is being approached, the feature points move as follows:

With fixed proportional relation, it gives

$$K_1 = \frac{GE}{DE} \quad (27)$$

$$\frac{GF}{HC} = \frac{DE}{AB} \quad (28) \quad /129$$

53

At such condition, continuous correlation tracking and matching should be carried out for tracking location. Selection, update and replacement of the features are carried out during the entire process of homing. Referring to Figure 9, there are 7 clear features in Figure 9(a) and the feature (2) can be used as a prestored image for matching since it has a larger $|\phi M - \phi N.M|$ value.

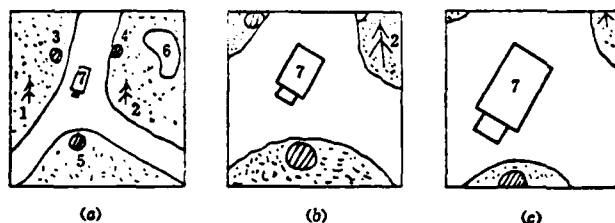


Figure 9. Feature Selection, Update and Replacement

Key: (a) Select Feature 2
 (b) Update 2
 (c) Feature Replacement

When the target is approached, the size of feature (2) increases and the reliability of matching decreases. At this moment the sensed image of feature (2) can be employed to replace the original prestored image. This is the process of feature update. When the target is more closed, feature (2) jumps out from the vision range and the feature (7) can be used to replace feature (2). The feature selection, update and replacement are carried out continuously during the entire target homing process for assuring the accuracy of target matching and tracking.

In the process of correlation tracking, the signal for tracking and homing is the geometrical distribution of the energy of the target and the surroundings but not the energy of the target alone. The indirect position location, which utilizes the

surrounding background features of the target, can be applied in long distance tracking. When the target is approached, the image of the target may exceed the scope of the vision and a local feature of the target in the image may be selected for carrying out the correlation tracking. The correlation tracking technique is very useful in tracking a target with a cluttered background.

V. Applications of the Matching Technique

The scene matching technique can be applied to recognize and locate the target. It has the clear advantage of the capability of locating the target from air-to-ground under the condition of cluttered background. The accuracy of navigation and guidance of a composite guiding system can be improved to within 10 meters by utilizing the auxiliary signals from ground (ground features, maps and ground targets) for position location. Figure 10 shows the block diagram of a combined optimum aided navigation system. The consecutive signals from the correlation matching device and the position signal outputs from the inertial navigation system, after Kalman filtering for optimum combination, can be used to correct the errors of position, speed, gyro draft and the bias of the accelerometer of the inertial navigation system. This type of combined navigation system can be employed in long distance navigation as well as short distance navigation for assault in regions with mountains and hills.

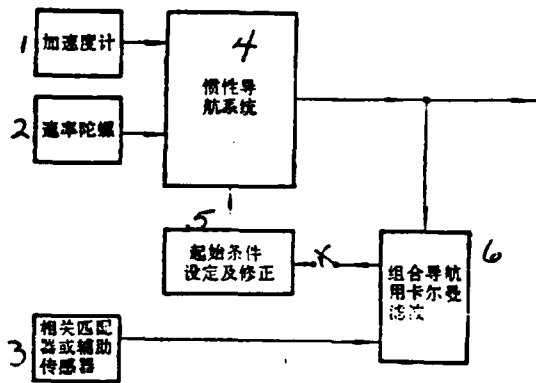


Figure 10. Combined Optimum Aided Navigation System

- Key:
1. accelerometer
 2. speed gyro
 3. inertial navigation system
 4. setting of initial conditions and modification
 5. correlation matching device or auxiliary transmitter
 6. Kalman filtering for combined navigation

With prestored topographic maps of the large flying range, the hidden and sneaking cruise following the ground features with dodging can be accomplished.

With target homing weapons, the tracking of a homing seeker /130 to the target can be controlled by utilizing the scene matching technique for determining the deviation of the aiming point from the target. Figure 11 shows the block diagram of the homing seeker using the map matching technique with millimeter wave radiometer for recording the image of the target.

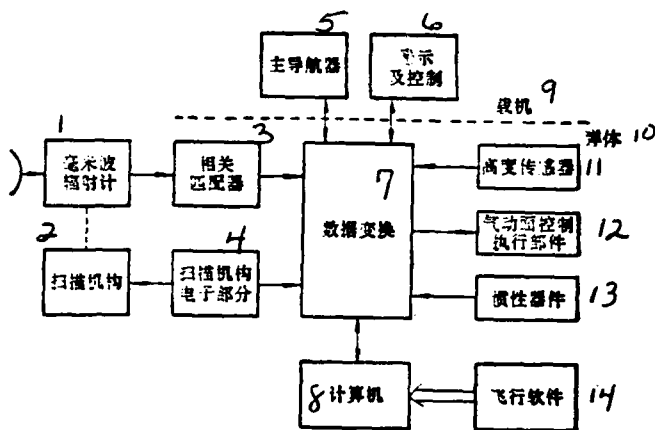


Figure 11. Homing Seeker With Map Matching

- Key:
1. millimeter wave radiometer
 2. scanning mechanism
 3. correlation matching device
 4. electronic portion of the scanning mechanism
 5. main navigation system
 6. display and controls
 7. data exchanger
 8. carrier
 9. homing seeker body
 10. altitude sensor
 11. control mechanism of aerodynamic surfaces
 12. inertial device
 13. computer
 14. software for flying

Additional to numerous applications in aviation and space flight, the scene matching technique can also improve the performance of the navigation and homing system. It can also be applied in industry for variety classification, quality control and improvement of the performance of the visual recognition of robots.

References

- [1] "New Developments in Feature Tracking and Dodging Techniques" International Aviation, Vol. 2 (1983).
- [2] Xu Guo-Zhen, The Development of the Inertial Navigation System of the Aircraft, International Aviation Technology of Carrier Equipment, Vol 2, (1983).
- [3] Wong, R.Y., Sequential Scene Matching Using Edge Features, TIEEE Vol. AES-14, No. 1, Jan., (1978).
- [4] Ormsby, C.C., Advanced Scene Matching Technique, NAECON, (1979).
- [5] Dai, Le-ping, Shen Zhenkang, Sun Zhongkang, A Modified Sequential Similarity Detection Algorithm for Fast Registration, NAECON, (1983).
- [6] Kuglin, C.D., Blumenthal, A.F., Pearson, J.J., Terminal Homing Technology with Scene Matching Using Fourier Phase Signals, Proc. of S.P.I.E., Vol. 186, May 22-26, (1979).
- [7] Lo, T.K., Gerson, G., Position Modification of the Homing System Using Correlation of Multiple Subimages, Proc. of S.P.I.E., Vol. 186, May 22-26, (1979).
- [8] Wong, R.Y., Scene Matching with Invariant Moments, Computer Graphics and Image Processing, 8, (1978).
- [9] Hiller, E.R., Synthetic Aperture Radar Map Matching for Navigation, NAECON, (1979).
- [10] Bjorklund, C.M., Loe, R.S., Li, R.Y., Matching of Planar Surfaces for 3-D Terminal Homing, NAECON, (1983).
- [11] Pridgen, J.H., Choate, W.C., Correlation Tracking Concepts for THASSID, NAECON, (1979).
- [12] Pratt, W.K., Digital Image Processing, John Wiley & Sons Inc., (1978).

SCENE MATCHING AND ITS APPLICATION TO AEROSPACE ELECTRONIC SYSTEMS

Sun Zhongkang

(Changsha Institute of Technology)

Abstract

This paper describes the principles and implementation of scene matching used in position location systems in brief. Several essential problems in scene matching technique are reviewed; measures of similarity (MAD, MSD, PROD, NPROD, Pair Functions etc.) are outlined; fast search methods (resolution from coarse to fine, quantization from coarse to fine, feature extraction, modified SSDA etc.) are introduced; probability of acquisition for max. or min. algorithm is given; preprocessing of images (filtering, restoration, whitening etc.) is considered; geometrical distortion (synchronization error, rotation, scale factor, perspective distortion) and its effects are analyzed, and the methods for overcoming such effects are presented.

After then, two noticeable important techniques for homing seeker, the feature matching and the correlation tracking, are remarked. Several methods of feature extraction are introduced for such features in scene matching as invariant moments, edge features, line features, planar features, vertex features etc.. The emphasis is put on feature selection, update and replacement in terminal target homing.

Finally, the block diagrams of a combined optimum aided navigation system and a homing seeker using correlation tracking are given.

Strengthening The Study on The Usability of Aircraft Materials^{*} /132

Wu Yunshu (Beijing Institute of Aeronautics and Astronautics)

Abstract

This paper tentatively defines the usability of an aircraft^{*} material. The usability of a material is defined as the material properties which meet the fabrication and the functional requirements.

In order to catch up with the current standard of aircraft design, the author, based on international research and development experience, commented on the improvement of the usabilitys of the conventional aircraft materials, such as low density materials and high temperature alloys.

I. Usability of Aircraft Material

It is a well known fact that the structural material for a structural part has to fulfill its requirement to perform its particular function. Briefly, the usability of a material is defined as the material properties which can fulfill the required function of a particular part.

Aircraft are different from other machines. First of all aircraft materials are required to be low density, high strength and high stiffness, i.e., high specific strength and high specific rigidity which are respectively represented by σ_b/ρ and E/ρ , where ρ represents density. Experience has shown that a material with high specific strength alone cannot fulfill the requirement of many structural parts. For instance, from Table I, if we select a bulkhead material only considering its specific strength, we can easily select the superstrength aluminum alloy 7178-T6. However 7178-T6 has low fracture ductility, and low critical crack length. During maintenance inspection it is more difficult to discover a crack in a 7178-T6 structure than a crack

^{*}Received in October 1983

in a 2024-T4 structure. Because of this 7178-T6 is '8-T almost obsolete now. Even for high tensile structure parts, the designers rather select 2024-T4 instead of 7075-T6.

Table 1 Properties of Extruded Aluminum Alloys^[1]

① 合 金 牌 号 与 状 态②	② σ_b 兆帕	$\sigma_{0.2}$ 兆帕	δ %	K_{IC} 兆帕 $\sqrt{\text{米}}$	④ 裂纹尺寸 毫米
2024-T4	428	321	12	49.4	25
7075-T6	593	538	7	30.7	3.5
7178-T6	628	579	5	27.5	2.3

⑤ 2024和7075分别相当于我国LY12硬铝和LC9超硬铝。

Key:

1. Alloy designation and temper
2. MegaPascal, MPa
3. MPa M, meter
4. Crack dimension, millimeter
5. 2024 and 7075 are equivalent to Y12 high strength aluminum alloy and LC9 super-strength aluminum allow respectively

In the early 1950's, explosions occurred in the jet transport Comet of the U.K. and the missile Polaris of the U.S. The investigation of the Comet accident revealed that it was caused by the intergranular corrosion in the aluminum alloy sheet of the pressurization cabin which leads to a fatigue failure.

From this discovery, the designers began using the fatigue strength within the endurance limit as a criterion to replace the static strength. In the Polaris accident, the initial failure occurred around a weld. Hence, the designers emphasized the importance of damage tolerance, and residue stress problems. Because of these experiences, numerous practices, and objective observations, the usability of a material is emphasized. However, there is still no precise conception or definition of usability.

/133

The usability of an aircraft material includes the following properties: mechanical properties at high and low temperature, fatigue and fracture properties, stability in the service environment, reaction to the environment, fabricability, and other required physical properties. For different parts, the material requirements are also different due to their different working conditions, different functions, and different fabrication techniques. Therefore, the "usability" of a material is defined as the material properties for fabrication and service of a certain structural part.

II. Designers Should Properly Specify the Usability of a Material

The usability of a material is recommended by the designer according to the working characteristics of a structural material. Before making recommendations, the designer should thoroughly understand the working environment of the structural part, its required properties as well as its fabricability, and should not tolerate any inaccuracies. Let us discuss the heating problem of the skin of a jet aircraft as an example.

If the air in the boundary layer is an ideal gas, then the streamline flow would proceed as an adiabatic process, i.e., no energy exchanged or lost. Then the relation between the arrest point temperature and the Mach number (M) should be expressed as: [2]

$$T = T_0 \left(1 + \frac{\gamma - 1}{2} M^2 \right) \quad (1)$$

which means that the arrest point temperature increases as a parabolic function of the Mach number. In Equation (1), T represents the arrest point temperature at the leading edge, in °K; γ is an adiabatic function, i.e., $\gamma = C_p / C_v = 1.4$; T_0 , air temperature at the specific altitude, °K. In reality, air has its viscosity. The energy in the boundary is continuously transferred and exchanged with viscosity loss through heat transfer. The main heat transfer occurs from the inside to the outside of the boundary layer. Therefore, the actual air

temperature near the skin is not the same as the arrest point temperature but lower. The actual temperature is called recovery temperature T_r which can be expressed as

$$T_r = T_0(1 + 0.2rM^2) \quad (2)$$

in which "r" is the recovery coefficient. When the boundary layer is a laminar flow, $r = 0.85$ substituting this value in (2), we obtain

$$T_r = T_0(1 + 0.17M^2) \quad (3)$$

Let the flying altitude = 11,000 meters, static air temperature = 216.5°K, then for $M = 2, 2.2,$ and 2.5 , the recovery temperature can be calculated from equation (3) as 90, 123, and 173°C, respectively^[2]. In equation (3), heat transferred to the skin or radiated to the static air is not considered. When we include these conditions, and paint the surface with enamel which makes the relative radiation coefficient 0.9, the average equilibrium temperature at a point two meters from the leading edge will be only 53, 65, and 107°C respectively for $M = 2, 2.2,$ and 2.5 at an altitude of 25,000 meters. Therefore, a precise calculation should be conducted for the skin temperature problem in the air stream. When the skin temperature data obtained from the wind tunnel test are used, we have to consider the difference between the air stream in the tunnel and the actual atmospheric condition. We should not specify a higher requirement for the material just because we could not make a precise estimation. For instance, when the actual temperature is 110°C, but the designer calls for a material to stand for a temperature of 150°C*, this overly specified aluminum alloy would cause great waste of man-power, material and time in searching for a new material.

III. Strengthen the Usability Research of Existing Materials /134

In addition to providing proper specifications for materials, we should also improve the properties of the existing materials, especially aircraft material, so that their

*Above 110°C, the strength of the super-strength aluminum alloy will drop drastically.

lift surfaces is allowed. A shock wave is inserted as a transition from a supersonic to a subsonic region.

In this work, the load distribution was expanded as a polynomial series with weighted functions and unknown complex coefficients. Linear equations needed to determine the coefficients were obtained from the boundary conditions at a control point. Results obtained in this work are in good agreement with the calculated and experimental values reported in references [1,8]. However, the time required by this method is shorter. Hence, this method is economic and practical.

II. Transonic Kernel Function Method

1. The integral equation correlating downwash to load distribution is

$$\frac{\omega_p^*(x, y, z)}{U} = \frac{1}{4\pi\rho U^2} \sum_{q=1}^Q \int_{S_q} \Delta P_q(\xi, \eta, \zeta) K(x_0, y_0, z_0, k, M) dS \quad (1)$$

where Q is the total number of lift surface elements on the wing, $\omega_p^*(x, y, z)$ is the downwash perpendicular to the p^{th} lift surface at the control point (x, y, z) , $\Delta P_q(\xi, \eta, \zeta)$ is the load distribution of the q^{th} lift surface at the integration point (ξ, η, ζ) which is unknown, and $K(\)$ is the kernel function. The integral equation (1) can be solved by allocation.

The method to connect subsonic and supersonic linearization /141 is based on the following two assumptions:

(1) When the downwash at a point is calculated, the M number at that point is used to compute the kernel function. If M is supersonic, the supersonic kernel function will be used. If it is subsonic, the subsonic kernel function will be used.

(2) The oscillation frequency ω remained unchanged by correcting the decrement frequency with local velocity.

A Kernel Function Method for Computing Unsteady Load on /140
Three-dimensional Wings in Transonic Flow*
Wu Yizhao (Nanjing Aeronautical Institute)

Abstract

A kernel function method for computing unsteady load on three-dimensional wings in a transonic flow and some calculations were presented in this paper. This method is based on the linearization of the lift surface which employs a kernel function to correlate load distribution to the downwash integral equation in subsonic and supersonic conditions. A local linearization method was used to treat transonic unsteady flow about the wings. Linear shock wave doublets and the appropriate normal shock wave boundary conditions were introduced into the calculation.

Beginning with supersonic and subsonic kernel function expressions, we conveniently treated the numeric integration in the subsonic region. Numeric integration of the supersonically induced downwash in the supersonic zone was presented. Three examples were given and the numerical values are in good agreement with those in the literature.

I. Introduction

In a transonic flow about the wing, the steady flow will affect the unsteady aerodynamics. There are shock waves over the wing and the velocity gradient is no longer small. Furthermore, shock wave oscillation creates an additional lift. It is inadequate to use a simple linearization theory to find the transonic unsteady aerodynamic force.

We believe that it is feasible to use a kernel function method to treat the transonic flow about the wing by local linearization. The idea is to consider the wing as several lift surfaces and mutual interference between subsonic and supersonic

*received in June 1983

References

- [1] James W. Mar, Fracture Prevention and Control, ASM (1974), 6.
- [2] Fang, Bao-Shan, Thermal Barriers of Supersonic Aircraft, (Guo-Fang Gony Yei Press), 1960, p 45.
- [3] Wu Yun-Shu, Ti-alloy: Present Status and its Future, (Guo Oji Hang Kung), 8, 1982, pp. 40-44.
- [4] John, A. Wert, Paton, N.E., et al., Grain Refinement in 7075 Aluminum by Thermo-Mechanical Processing, Metall. Trans. ASM-AIME, 12A, (1981), pp. 1267-1276.
- [5] Wood, R.A., Beta Titanium Alloys, Metals and Ceramics Information Center, (1972).
- [6] Metallurgical and Mechanical Properties of an Advanced High Toughness Alloy Ti-10V-2Fe-3Al, Timet Titanium Data, p. 5.
- [7] Metals Handbook, Vol. 2, 9th Edition, ASM, (1979), pp. 129-138.
- [8] Wu Yun-Shu, A Study of Using Aluminum to Substitute Steel, Beijing Institute of Aeronautics & Astronautics, Report BH-B181, 1964, 8.

STRENGTHENING THE STUDY ON THE USABILITY OF AIRCRAFT MATERIALS

Wu Yunshu

(Beijing Institute of Aeronautics and Astronautics)

Abstract

An exact definition of the usability of aircraft materials is discussed in this paper. The usability of an aircraft material means its necessary properties which qualify it for a specified aircraft structure part both in manufacturing and service.

Optimal measures and approaches for improving the usability of conventional aircraft materials (aluminum and titanium alloys), materials with low density (Al-Li alloys, Ti_3Al and $TiAl$ alloys and composites) and superalloys both metallurgically and technologically are put forward.

In the 1940's and 1950's, the temperature before the turbine was limited by the heat resistant property and the stability of the material. In order to increase heat resistance the turbine blade of high temperature cast alloy was developed to replace forged alloys (including nickel, and cobalt based alloys). The operating temperature increased at a rate of 10°C a year. At the end of the 1950's the maximum tolerable temperature reached 930°C. The most recently developed direct solidification single crystal blade could only stand up to 940 to 980°C. Directionally /139 solidified eutectic blades could be used at 1040°C. The rapid solidification powder nickel based alloy, or the tungsten fiber reinforced nickel alloy could be used at 1100°C. In other words, in spite of sophisticated fabrication techniques, it is not possible to make the service temperature above 1250°C, because the melting points of these alloys are all between 1300 to 1350°C. To increase the material service temperature, the course of developing high melting point metal (e.g., Mo, Nb, Ta, etc) base alloys or ceramic material has to be followed. Since there are still plenty of problems for the application of these metals, it is not possible to put them into application in the near future.

Since the early 1960's, the temperature before the turbine has been increased to about 1000°C by means of cooling the turbine blade. As mentioned above, after 1960, although there has been development of high temperature alloys, the main temperature increasing technique before the turbine still relies on the cooling technique.

VII. Comments

In conclusion, in order to advance our aircraft industry standard to the proper level before the year 2000, it is necessary for us to consolidate the international research and fabrication experience and to avoid any deviation so that the material usability can be promoted to the highest standard aiming at meeting the functional and fabricating requirements of aircraft structural parts.

performance which depends on the design parameters such as the pressure ratio of the compressor, and the temperature before the turbine. The promotion of the sub-assembly performance depends on the improvement of the structure which in turn depends on the improvement of the material and the fabrication method.

Back in 1940, the pressure ratio of a compressor ranged between 4:1 to 5:1. Currently, it reaches 25:1. The high pressure ratio will enhance the effect of the temperature before the turbine. Therefore, future development will follow the trend of increase of the temperature before the turbine.

The relation among the specific thrust, the pressure ratio of the compressor, and the temperature before the turbine of a single axial and dual-axial turbo-engine can be expressed as follows:

$$R_d = 0.45\phi_c \left\{ \frac{C'_p}{A} T_z \left[1 - \left(\frac{1}{\gamma \pi_{K_0}} \right)^{\frac{K'-1}{K'}} \right] - 102.5 T_0 \frac{\pi_{K_0}^{0.251} - 1}{\eta_K \eta_T} \right\}^{1/2} \quad (4)$$

where, R_d = specific thrust, second; ϕ_c = tail speed coefficient, about 0.98; A = heat equivalent, 1/427; T_z = temperature before the turbine, °K; γ = combustion chamber total pressure recovery coefficient, about 0.92; π_{K_0} = compression ratio; K' = combustion gas adiabatic index, 1.33 when T_z between 1000 - 1300°K; 1.27, between 1700 to 2000; C'_p = specific heat of constant pressure, 0.277 when $K' = 1.33$, 0.323 when $K' = 1.27$; η_K = compressor efficiency, about 0.78; η_T = turbine efficiency, 0.88; T_0 = temperature at altitude °K. Generally speaking, the ground thrust is used as a design criterion. When the engine is tested at sea level, $T_0 = 288^\circ\text{K}$. When all the above parameters are substituted into equation (4), we obtain

$$R_d = 0.441 \left\{ 427 C'_p T_z \left[1 - \left(\frac{1}{0.92 \pi_{K_0}} \right)^{\frac{K'-1}{K'}} \right] - 43000 (\pi_{K_0}^{0.251} - 1) \right\}^{1/2} \quad (5)$$

From equation (4), we can see that the increase in temperature before the turbine is more effective than the increasing of the pressure ratio. Therefore, in the engine hot section, the main concern of the usability is how to make a material stand higher temperatures.

Table 5 Typical Properties of Aircraft Materials

/138

① 材料类别	② ρ 克/厘米 ³	③ σ_b 兆帕	④ σ_b/ρ 米 ³ × 10 ³	⑤ E 兆帕 × 10 ³	⑥ E/ ρ 米 ³ × 10 ³	⑦ 抗蚀性	⑧ 最高使用温度 ℃
⑨ LC9超硬铝, 棒材	2.85	647	23	70.6	2500	须防护⑭	110
⑩ Ti-10V-2Fe-3Al, 锻件	4.65	1103	24.2	106	2260	优秀⑮	315
⑪ AF1410结构钢⑬, 锻件	8.0	1755	22.3	206	2625	良好⑯	260
C/环氧准各向同性板⑫	1.6	422	26.9	49	3130	吸湿⑰	150
C/6061-T6⑬ 铝基复合材料板⑬	2.3	765	33.9	125	5560	优良⑱	400

⑭ ① AF1410的名义成分为Fe-0.16C-14Co-2Cr-10Ni-1.0Mo-0.15Mn.

⑮ ② 6061铝合金的名义成分为Al-1Mg-0.6Si-0.25Cu-0.25Cr, T6表示固溶处理与人工时效.

Key:

1. materials
2. ρ g/ml
3. σ_b MPa
4. σ_b/ρ M x 10³
5. E MPa x 10³
6. E/ ρ M x 10³
7. corrosion resistance
8. max. service temperature °C
9. LC9 super Al rod
10. Ti-10V-2Fe-3Al, forging
11. AF1410 structural steel, forging
12. C/epoxy, different direction plate
13. C/6061-T6 aluminum-base composite plate
14. need protection
15. excellent
16. good
17. absorb moisture
18. good
19. The nominal composition of Af1410 is Fe-0.16C-14 Co-2Cr-10Ni-1.0Mo-0.15Mn.
20. The nominal composition of 6061 aluminum is Al-1Mg-0.6Si-0.25Cu-0.25Cr, T6 represents solution treatment and artificial aging.

VI. How to Improve Material Usability to Enhance Engine Performance

With regard to fighters, the engine enhancement mainly depends on the thrust-weight ratio. At present, for the advanced engines, the thrust-weight ratio is 8. It is projected that in the 1990's, this ratio can reach 11 for the augmented turbo-fan engine or variable-thermo-cycle engine. The increase of the thrust-weight ratio depends on the increasing of the sub-assembly

Table 4 Properties of Carbon Fiber/Epoxy Composite Plates

性 能 ①	② 单向 (0°)	0°/±45°/90°	0°/±45°	Lc9cs	LY12CZ
	③ 板	④ 板	⑤ 板	⑥ 超硬铝板	⑦ 硬铝板
⑧ σ_1 , 兆帕	1098	422	647	540	352
⑨ σ_2 , 兆帕	62	422	276	540	392
⑩ $E_1 \times 10^3$, 兆帕	126.5	49	721	70.6	70.6
⑪ $E_2 \times 10^3$, 兆帕	9.2	49	21.6	70.6	70.6
⑫ T_{12} , 兆帕	69	275	275	324	253
⑬ $G_{12} \times 10^3$, 兆帕	5.2	18.6	18.6	26.5	26.5
⑭ 密度, 克/厘米 ³	1.6	1.6	1.6	2.8	2.8

⑮ 注内, 注脚 1 指 0° 方向; 注脚 2 指 90° 方向。

Key:

1. properties
2. unidirectional (0°)
3. plate
4. 0°/+45 plate
5. 0°/+45 plate
6. Lc9cs super-strength Al-plate
7. LY12CZ high strength Al-plate
8. σ_1 , MPa
9. σ_2 , MPa
10. $E_1 \times 10^3$, MPa
11. $E_2 \times 10^3$, MPa
12. T_{12} , MPa
13. $G_{12} \times 10^3$, MPa
14. density g/ml
15. subscript 1 denotes 0° direction; 2, 90°

However, resin composites tend to absorb moisture, are brittle and have low interlayer shear strength (Table 4). Since 1970, the metallic base composites have been widely studied. Among these composites, some, such as B/Al and C/Al, have been used in aeronautical and astronautical vehicles. For room temperature and high temperature applications, these materials have higher strength and lower density, and rigidity, than the conventional materials (Table 4). The metal based composite has good dimensional stability, fabricability, and joinability, similar to the metals. At the same time, it has many applicable properties similar to resin composites. Therefore, the metallic composite has the potential to replace titanium alloy for high temperature structural parts.

consolidate rapidly solidified powder. The test of the Al-Li alloys for aircraft application is in progress in other nations. For titanium alloy systems, the alloys adopting intermetallics Ti Al and TiAl as bases have been developed in many nations. Their densities are 4.2 and 3.85 g/ml respectively, about 6% and 14% respectively lower than the current titanium alloys. The characteristics of these alloys are similar to the high temperature alloy, and can be used up to 800 to 900°C, yet their densities are about 45 to 49% lower than the high temperature alloys (around 8.5 g/ml). The performance of the jet engine will be improved when these materials are used for the parts in the hot section, especially for the rotating parts such as turbine blades. Therefore, other nations are interested in developing these types of alloys.

Among the low density non-metallic materials, the most commonly used material is carbon-fiber/epoxy composite material. Table 4 shows that its strength is similar to the super-strength aluminum, but its density is only 60% of aluminum. To meet the aerodynamic requirements, the strength and the elastic modulus of the material can be modified by changing its layer direction, number of layers and the cutting direction. This function makes it possible to build sweep-forward wing aircraft. This composite belongs to the static meta-stable mechanics system. Therefore, its fatigue and fracture properties are superior to metallic material. This composite material can be formed into complicated forms, hence the number of parts and fasteners can be decreased. It is predicted that for a great number of aeronautical and astronautical structure parts, conventional material will be replaced by composite material.

7. forged parts

V. Strengthen the Research of Low Density Materials to Further Lower Aircraft Structure Weight

As mentioned before, the specific strength and the specific rigidity are represented by σ_b/ρ and E/ρ respectively. These two terms are used for simple tensile loads only. For a plate under bending, they will be represented by $\sigma_b^{1/2}/\rho$ and $E^{1/3}/\rho$ respectively; for a shape under bending, $\sigma_b^{2/3}/\rho$ and $E^{1/2}/\rho$; and for slender column under compression, $E^{1/2}/\rho$.^[8] From these terms, we can see, from the aspect of decreasing the structure weight, that it is more effective to decrease the material density than to increase the material strength. From this point of view, the history of aeronautical material development is in fact a history of decreasing the material density. A low density material is a material with a density below 4.5 gram/milliliter (g/ml). At present low density alloys include magnesium alloy (1.8 g/ml), aluminum alloy (2.8 g/ml), and titanium alloy (4.5 g/ml). Low density non-metallic materials include directional graphite fiber resin composite plate (1.6 g/ml). /137

The application of magnesium alloys, which have low densities, yet poor corrosion resistance, has been reduced recently. One method to reduce the specific weight of aluminum is to develop Al-Li alloy system with the addition of magnesium or copper as alloying elements. The density of Al-2.84Li is 2.49 g/ml, about 11% less than that of the super-strength alloy. The elastic modulus is 80.6×10^3 MPa, about 26% higher. But, the strength remains about the same. This alloy has good corrosion resistance and can be used in sea-water without cladding. For aircraft applications, it can save the structure weight by up to 15%. However, when Al-Li alloy is fabricated by the conventional method, its malleability becomes very poor and its fracture ductility decreased. These disadvantages can be corrected by powder metallurgical methods to

Key:

1. alloy
2. semi-finished
3. parts
4. plate, rod, edging
5. all products
6. MPa
7. MPa
8. MPa \sqrt{M}
9. hardenability
10. diameter
11. strength difference
circumference and center

Therefore, we should develop different types of titanium alloys to meet different requirements. In China, we have an abundant supply of titanium ores. We should strengthen the research and development effort on titanium in order to meet the demand in the national economical construction.

The widely used aluminum alloys are LY12 LC4 and LC9. These alloys usually contain high impurity contents (about 0.5% Fe and 0.5% Si). Consequently, their corrosion resistance and fracture ductility are greatly impaired. In other nations, they precisely control the impurity levels, and made high purity super-strength aluminum alloy which is widely used in new airplanes.

Table 3 Fracture Toughness of Super Dural Plates [7]

① 合金名称 及状态	② 名义成分 ③ %重量	④ 主要杂质含量 ⑤ %重量	K _{IC} , 单位 $\sqrt{kg/cm^2}$		
			LT	TL	SL
7075-T651	5.6Zn-2.5Mg-1.6Cu-0.23Cr	0.5Fe, 0.5Si	28.6	24.2	17.6
-T7351			33.0	31.9	22.0
7175-T736●	5.6Zn-2.5Mg-1.6Cu-0.23Cr	0.2Fe, 0.15Si	33.0	28.6	28.6
7475-T651	5.7Zn-2.3Mg-1.5Cu-0.22Cr	0.12Fe, 0.10Si	42.9	37.4	29.7
-T7651			47.3	38.5	30.8
-T73651			43.0	41.8	35.2

⑦ ● 承板件。

1. alloy designation and temperature
2. nominal composition
3. % weight weight
4. main impurities
5. % weight weight
6. K_{IC}, MPa \sqrt{M}

requirements. The advantages of this alloy are: 1) it has a body centered cubic structure (after quenching or air cooling) which makes the alloy possess better plasticity, and formability at room temperature; 2) after being fabricated the alloy can be aged to attain high strength; 3) after being properly treated, it has the best combination of strength-malleability-ductility; 4) it has good hardenability which can make a part with a thick cross-section uniform in property; 5) it can be fabricated by isothermal forging, hot die forging, super-plasticity forming, and diffusion joining; 6) it maintains high temperature stability (up to 350°C) and chemical stability; and 7) from the aspect of tensile, yield strength, and fracture ductility, it is better than Ti-6Al-4V alloy (Table 2). Therefore, β -titanium alloy is suitable to make any structural parts in which service temperatures do not exceed 350°C, and whose thicknesses do not exceed 150 mm. Among these alloys, the usability of Ti-10V-2Fe-3Al (near β -titanium alloy) is the best. It obtains the advantages of sub-stability β -titanium alloy, yet maintains the characteristics of $\alpha + \beta$ titanium alloy. It is suitable for making aircraft parts due to the following advantages; at 315°C its creep property is similar to Ti-6Al-4V alloy. It has good ductility and corrosion resistance in atmosphere and in sea-water, and superior forgability.

Table 2 Comparison of Properties Between β -titanium Alloys and Ti-6Al-4V (quenched and aged)

① 合 金	② 半 成 品 ③ 类 型	σ_b 兆帕 ⑥	$\sigma_{0.2}$ 兆帕 ⑦	δ %	K_{IC} 兆帕 $\sqrt{米}$ ⑧	⑨ 淬 透 性	
						直径 mm ⑩	圆棒与中心 硬度差, MPa ⑪
Ti-8Mo-8V-2Fe-3Al	板、棒、锻件	1310	1211	8	70	150	94
Ti-3Al-8V-6Cr-4Zr-4Mo	板、棒、锻件	1448	1378	7	60	150	35
Ti-11.5Mo-6Zr-4.5Sn	板、锻件	1300	1230	6	66	150	50
Ti-10V-2Fe-3Al	板、棒、锻件	1241	1172	10	80	125	48
Ti-6Al-4V	⑤ 各类成品	1000~1155	925~1030	10	51	150	133

Another common aircraft material is the LC4 (or LC9) super-strength aluminum alloy. Recent thermal-mechanical process research (or strain-aging treatment)^[4] showed that its crystal size can be reduced to 6 - 10 microns- about 10 to 30 times smaller than the conventional alloy. After this treatment, this alloy can obtain the super-plasticity property at 450 to 480°C. This property makes it possible to produce complicated parts at low cost, yet still obtaining improved fatigue properties and anti-corrosion properties at light weight.

Therefore, in order to meet the current requirement, we should apply different manufacturing technologies, especially new fabrication methods to research the usability of the existing materials.

IV. Strengthen the Usability Research with "Definite Purpose"

We solve the problem from only one aspect if we strengthen the usability of the conventional aircraft material. When we utilize a material for multi-purpose applications, we sometimes emphasize one property at the expense of the other properties of the same material. It is difficult to fully utilize the material's inherent properties.

For example, for a long period of time, the Ti-6Al-4V titanium alloy has been widely used in the aeronautical and astronautical industries. As mentioned before, with proper recrystallization treatment, the room temperature and high temperature stability cannot match the alpha type titanium alloy. Therefore, the compressor blades of the current combustion turbine are always made with α -titanium alloy which is stable at high temperature. For aircraft structures the strength of Ti-6Al-4V alloy is not high enough. This alloy has low fracture ductility, and low hardenability. In addition, it has to be fabricated at high temperature. Therefore, many β -titanium alloys have been developed in different nations to meet these

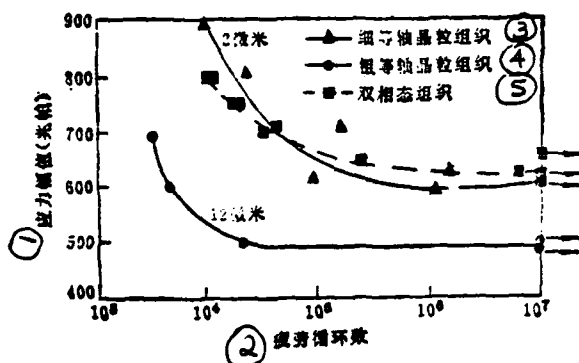


Figure 2. The Effect of Microstructures on Fatigue Life for Unnotched Ti-6Al-4V Specimen (aged at 500°C, in 3.5% NaCl solution, $R = -1$)

- Key:
1. Stress range, MPa
 2. Fatigue cycle
 3. Fine equiaxial crystal structure
 4. Coarse equiaxial crystal structure
 5. Bi-modal microstructure

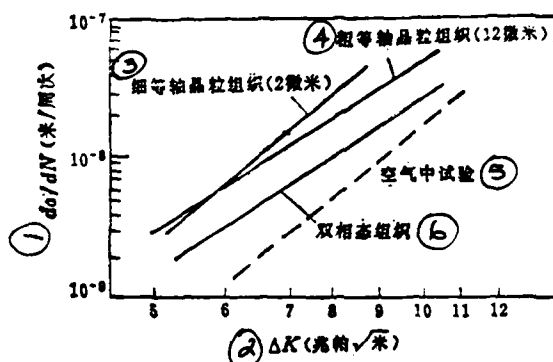


Figure 3. The Effect of Microstructures on Crack Growth Rate for Unnotched Ti-6Al-4V Specimen (aged at 500°C, in 3.5% NaCl solution, $R = 0.2$)

- Key:
1. da/dN (M/cycle)
 2. ΔK (MPa \sqrt{M})
 3. Fine equiaxial crystal structure (2 microns)
 4. Coarse equiaxial crystal structure (12 microns)
 5. Test in air
 6. Bi-modal structure

usability can meet the requirement of different structural parts.

For instance, one of the most widely used materials is $\alpha + \beta$ type titanium alloy Ti-6Al-4V. To make the compressor blade, this alloy is fabricated in the two-phase zone and then annealed at 700°C to assume the service structure as well as property stability under the service condition. However, this treatment process does not fully utilize the alloy usability for the compressor blade. Neither its mechanical properties at room temperature are fully utilized nor its creep resistance at high temperature is fully achieved. For improvement, a new recrystallization technique is adopted. This technique can be create a microstructure composed of a controlled amount of equiaxial α -crystals, and balanced with plate-type $\alpha + \beta$ structure, i.e., a bimodal structure (Fig. 1).

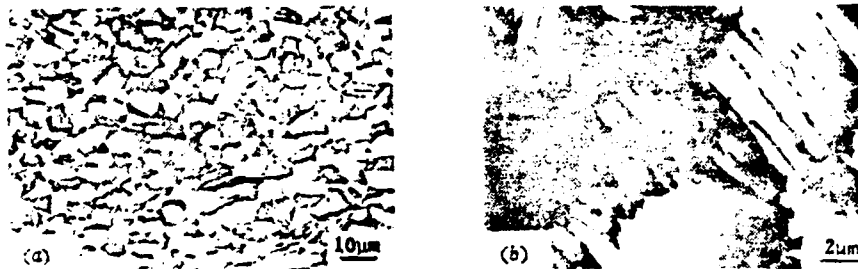


Figure 1. Bi-modal Microstructure

- a. LM
- b. TEM

After being aged, the fine $TiAl_3$ phase precipitates from the α phase; at the same time, the very fine α phase precipitates from the β phase. This distribution can achieve the best combination of mechanical properties, fatigue properties and creep (Fig. 2 and 3).

$$k_L = k_\infty \frac{U}{U_L} \approx k_\infty \frac{M}{M_L} \quad (A)$$

where k is the decrement frequency. The subscript "L" represents the local value and " ∞ " represents the incoming flow value.

When the wing oscillates in small amplitude, the following integral equation can be obtained:

$$\left(\frac{\partial z}{\partial x} + ik_{xy} z \right) = -\frac{1}{8\pi} \iint \Delta C_p K(x_0, y_0, k_{xy}, M_{xy}) d\xi d\eta \quad (2)$$

where ΔC_p is the load amplitude.

2. Numerical Integration Technique

Numerical integration of eq (2) in the span and chord directions is obtained:

$$\frac{\bar{\omega}^*(x, y)}{8} = \frac{\pi}{S} \sum_{s=1}^S \frac{(1 - \eta_s)^2 G(\xi_s, \eta_s)}{(\xi_s - \eta_s)^2} - \pi SG(\xi_s, \eta_s) \quad (3)$$

The optimum position of the downwash chord is

$$\xi_r = -\cos\left(\frac{r\pi}{R_1 + 1}\right), \quad r = 1, 2, \dots, R_1 \quad (B)$$

R_1 is the number of downwash chords over the entire wing span.

The optimal position of the integration chord is

$$\eta_s = -\cos\left(\frac{2s-1}{2S} \pi\right), \quad s = 1, 2, \dots, S \quad (C)$$

S is the number of integration chords over the entire wing span,
 $S = R_1 + 1$

$$+ \frac{1}{a} \frac{2\pi}{2J+1} \sum_{j=1}^J (1 - \xi_j^2)^{1/2} [\sin a R_j - i \cos a R_j] \quad (6)$$

$$\phi(x, y) = \left[g_0(y) \left(\frac{1-x}{1+x} \right)^{1/2} + g_1(y) (1-x^2)^{1/2} + \dots \right] \quad (7)$$

$$\Phi_z(x, y) = \frac{1}{\sqrt{1-x^2}} \left[-g_0(y) \frac{1}{1+x} - g_1(y)x + \dots \right] + ib(y) k \left(1 - \frac{1}{\beta^2} \right) \phi(x, y) \quad (8)$$

In equation (9)

$$\begin{aligned} G(y, y) = & \frac{2\pi}{2J+1} \sum_{j=1}^J [g_0(y)(1 - \xi_j) + g_1(y)(1 - \xi_j^2) + \dots] \left(1 + \frac{x - \xi_j}{|x - \xi_j|} \right) \\ & \times e^{-ik \left[(x - \xi_j) \left(1 - \frac{1}{\beta^2} \right) + M(x - \xi_j)/\beta^2 \right]} + \phi(x, y) \left\{ H_0(x, y, y) \right. \\ & \left. - \frac{2\pi}{2J+1} \sum_{j=1}^J (1 - \xi_j^2)^{1/2} \left(1 + \frac{x - \xi_j}{|x - \xi_j|} \right) e^{-ikM|x - \xi_j|/\beta^2} \right\} \\ & + \phi_z(x, y) \left\{ H_1(x, y, y) \frac{1}{b(y)} - \frac{2\pi}{2J+1} \frac{1}{b(y)} \sum_{j=1}^J (1 - \xi_j^2)^{1/2} (\xi_j - x) \right. \\ & \left. \times \left(1 + \frac{x - \xi_j}{|x - \xi_j|} \right) e^{-ikM|x - \xi_j|/\beta^2} \right\} \quad (9) \end{aligned}$$

$$H_0(x, y, y) = \frac{2}{b(y)} \{ \sin a(x - x_{LE}) + i [1 - \cos a(x - x_{LE})] \} \quad (10)$$

$$H_1(x, y, y) = \frac{2}{b(y)} \left\{ \frac{1}{a} (x_{LE} - x) \sin a(x - x_{LE}) + \frac{1}{a^2} [1 - \cos a(x - x_{LE})] - \frac{i}{a} (x_{LE} - x) \cos a(x - x_{LE}) - \frac{i}{a^2} \sin a(x - x_{LE}) \right\} \quad (11)$$

The subscripts "LE" and "TE" represent the leading edge and trailing edge values.

(2) Calculation of Self-induced Downwash in Supersonic Region

A detailed description of this calculation was given in reference [2] using a sweptback wing as an example. It will not be repeated here.

(3) Calculation of Downwash Induced by Supersonic Region

From eq (2), we get

$$\frac{\bar{\omega}^*(x, y)}{8} = \int_{-1}^1 \frac{1}{(y-\eta)^2} \left[\int_{-1}^1 P(\xi, \eta) \sum_{j=1}^{NC \times NS} a_j U_{f(j)}(\eta) U_{f_1(j)}(\xi) e^{-ikx_0} \times \left(\left(\frac{x_0}{R} + 1 \right) e^{-ikx_1 r} - I_{11} \right) b(\eta) d\xi \right] d\eta \quad /143 \quad (12)$$

The numerical integration for each j in the chord direction is

$$G_j(y, \eta) = U_{f(j)}(\eta) b(\eta) - \frac{\pi}{J} \sum_{s=1}^J (1 - \xi_s^2)^{1/2} P(\xi_s, \eta) U_{f_1(j)}(\xi_s) K_1 \quad (13)$$

where $U_{f(j)}(\eta)$, and $U_{f_1(j)}(\xi_s)$ are Chebyshev polynomials of the second kind, $P(\xi_s, \eta)$ is the weighted load function, K_1 is the kernel function, N_c is the number of chord control points and N_s is the downwash chord number.

The spanwise numerical integration of eq (12) is similar to the calculation of self-induced downwash in a supersonic region.

(4) Calculation of Downwash in Subsonic Region Induced by Shock Wave Doublets

$$\omega_D^*(x, y) = -\frac{1}{S} \sum_{r=1}^S \frac{(1 - \eta_r^2) G(y, \eta_r)}{(y - \eta_r)^2} + G(y, y) S \quad (14)$$

where

$$G(y, \eta_r) = \left(1 + \frac{x - x_r}{[(x - x_r)^2 + \beta^2 r^2]^{1/2}} \right) \sum_{j=1}^{NS-1} b_j U_{f(j)}(\eta_r) \quad (15)$$

$$G(\underline{y}, \underline{y}) = \left(1 + \frac{x - x_r}{|x - x_r|}\right) \sum_{j=1}^{NS-1} b_j U_{j(\underline{y})}(\underline{y}) \quad (16)$$

$$\underline{\eta}_r = -\cos\left(\frac{2r-1}{2S} \pi\right) \quad r = 1, 2, \dots, S$$

S is the total number of spanwise integration chords and x_s is the chordwise position of the shock wave at $\underline{\eta}$.

III. Normal Shock Wave Boundary Conditions

The intensity of shock wave doublets is similar in form to that of the linear lift strength. It can be expressed as

$$\Delta L(\underline{\eta}) = \frac{4\rho U^2}{b_{AVG}} S_0 l(\underline{\eta}) [b_0 U_0(\underline{\eta}) + b_1 U_1(\underline{\eta}) + \dots] \quad (17)$$

where $l(\underline{\eta})$ is the spanwise weighted function, b_n is the unknown coefficient and b_{AVG} is the average geometric chord length of the wing.

The boundary condition to satisfy the shock wave is

$$\phi_x^+ - K^* \phi^+ = -\mu \phi_x^- - K^* \phi^- - i\nu \phi^- \quad (18)$$

where

$$K^* = \frac{\phi_{ix}^+ + \mu \phi_{ix}^- + i\nu \phi_{ix}^- - \frac{2ik}{r+1} \left(1 + \frac{1}{M_\infty^2}\right)}{\phi_{ix}^+ - \phi_{ix}^-} \quad (19)$$

$$\nu = \frac{2(r-1)}{r+1} k \quad (20)$$

$$\mu = \frac{r-1}{r+1} + \frac{2}{(r+1)M_\infty^2} \quad (21)$$

ϕ_1 is the average velocity potential of the steady flow and ϕ is the perturbed velocity potential caused by shock wave displacement. The superscripts "-" and "+" represent the upstream and downstream shock wave parameters, respectively.

IV. Procedures to Solve Transonic Kernel Function

/144

In a transonic flow, a "transonic pair" of lift surfaces is used to express the physical model of a flow about the wing. Figure 1 shows a simple example which divides the wing surface into a supersonic (Wing Surface 1) and a subsonic (Wing Surface 2) region according to the shock wave position in a steady flow. The "transonic pair" aerodynamic matrix structure is shown in Figure 2. Matrices A_{11} and A_{22} represent the self-induced downwashes in the supersonic and subsonic regions, respectively. A_{12} and A_{1D} (which are zero) are the downwashes in the supersonic region induced by the subsonic region and the shock wave doublets, respectively. A_{21} and A_{2D} are the downwashes of the subsonic region induced by the supersonic region and shock wave doublets, respectively.

$$\begin{aligned} B_{,1} &= \mu \phi_1^- + k \phi^- \\ B_{,2} &= \phi_1^+ \\ B_{,D} &= -k \phi^+ \end{aligned} \quad (A)$$

w_1 and w_2 are the downwash velocities at the control points in the supersonic and subsonic regions, respectively. They are given as boundary conditions. a_1 and a_2 are coefficients of the load distribution series in the supersonic and subsonic regions, respectively. b_D is the coefficient of the shock wave doublet distribution series, which is yet to be determined.

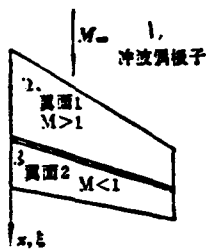


Figure 1. Geometric Arrangement for a "Transonic Pair" of Lifting Surfaces

Key:

1. shock wave doublets
2. Wing Surface 1
3. Wing Surface 2

A_{11}	A_{12}	A_{1D}
	0	0
A_{21}	A_{22}	A_{2D}
B_{S1}	B_{S2}	B_{SD}

a_1
a_2
b_D

 $=$

w_1
w_2
0

Figure 2. Matrix Construction for a "Transonic Pair"

IV. Results and Analysis

1. An oscillating trapezoidal wing is shown in Figure 3.

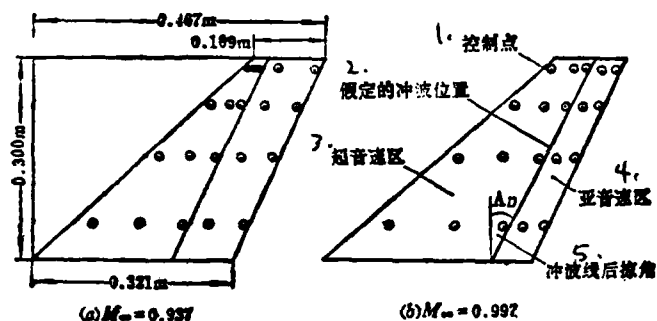


Figure 3. Shock and Planform Geometry for the Trapezoidal Wing

- Key:
1. control point
 2. assumed shock wave position
 3. supersonic region
 4. subsonic region
 5. shock wave sweptback angle

(1) $M_{\infty} = 0.937$. The results of this work are in good agreement with the calculated values given in reference [1], as shown in Figure 4. The calculated value of ΔC_{pIM} deviates quite significantly from the experimental value in front of the shock wave which is caused by strong wall interference^[1].

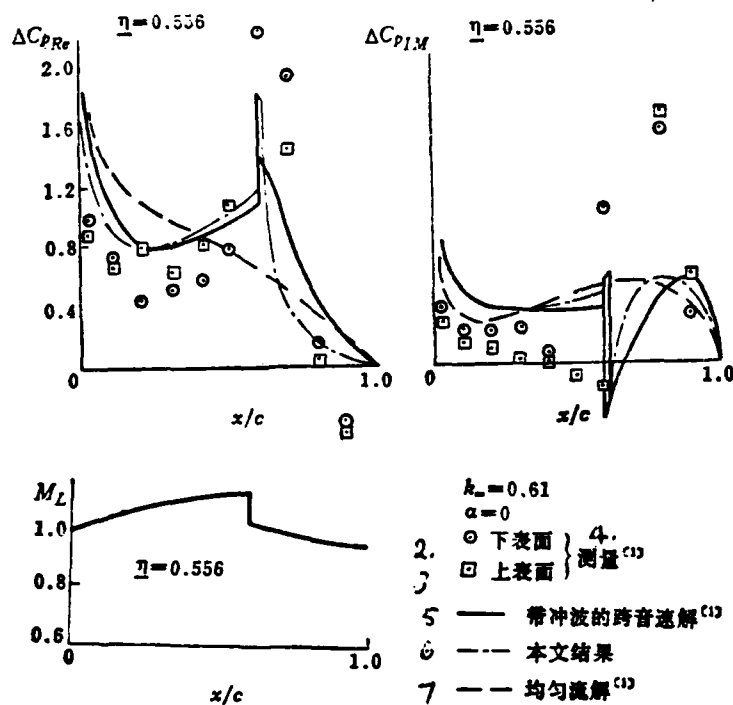


Figure 4. Results for the Oscillating Trapezoidal Wing at $M_\infty = 0.937$

Key:

1. chordwise distribution of M_L
2. \circ bottom surface
3. \square top surface
4. measured^[1]
5. — transonic solution with shock wave^[1]
6. --- this work
7. --- homogeneous flow^[1]

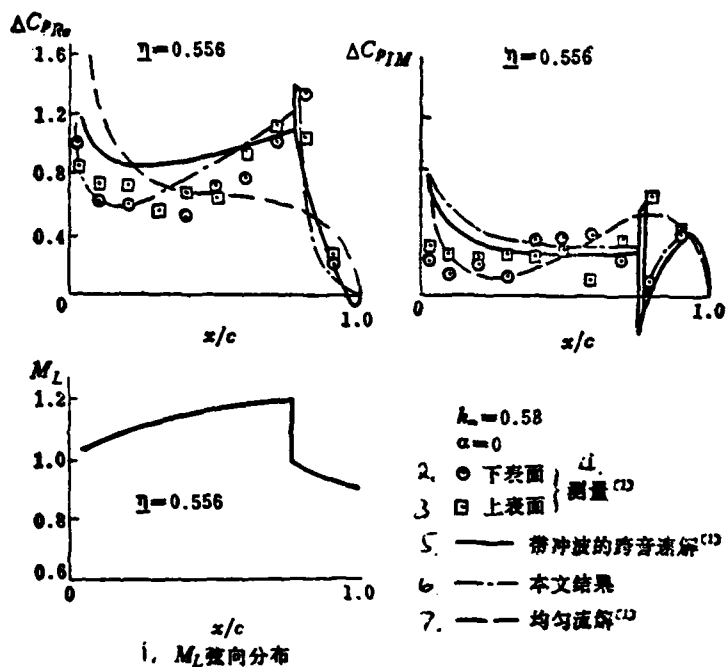


Figure 5. Results for the Oscillating Trapezoidal Wing at $M_\infty = 0.997$

- Key:
1. chordwise distribution of M_L
 2. \circ bottom surface
 3. \square top surface
 4. measured [1]
 5. transonic solution with shock wave [1]
 6. this work
 7. homogeneous flow [1]

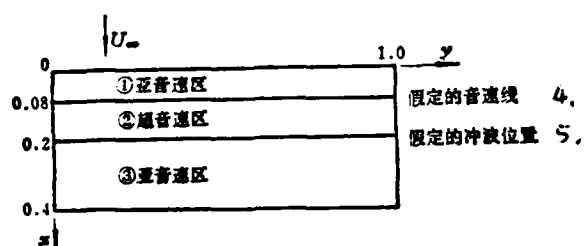


Figure 6. Model for Calculation of Rectangular Wing

- Key:
1. subsonic region
 2. supersonic region
 3. subsonic region
 4. assumed sonic line
 5. assumed shock wave position

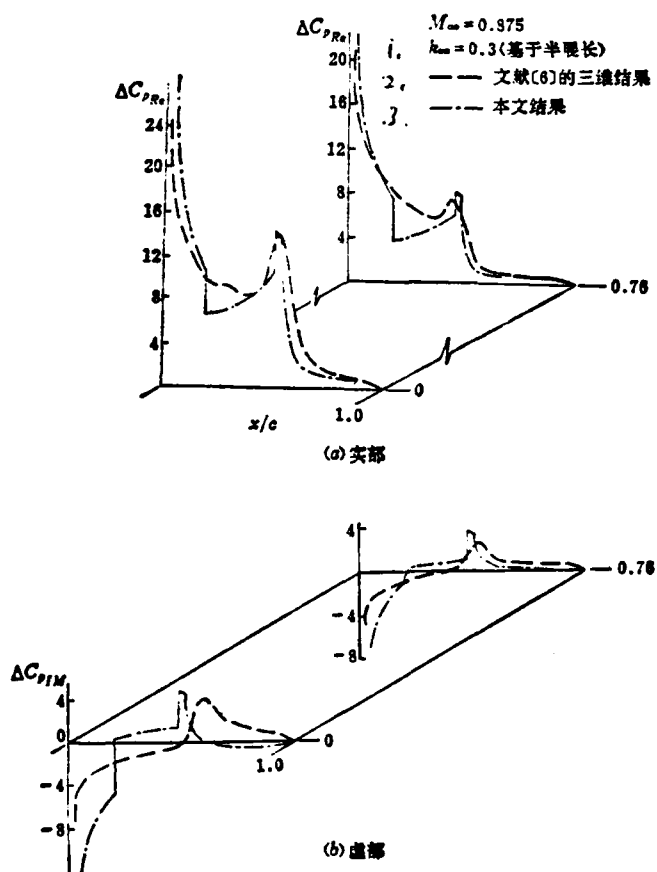


Figure 7. Pressure Coefficient Distribution for a Rectangular Wing Oscillating in Pitch

Key: a. Real Part b. Imaginary Part
 1. (based on half span)
 2. three-dimensional results in reference [6]
 3. — this work

(2) $M_\infty = 0.997$. The results of this work are in good agreement with the calculated and experimental values given in reference [1], as well as the values of ΔC_{pRe} and ΔC_{pIM} in front of and behind the shock wave, as shown in Figure 5.

2. Rectangular Wing Oscillating in a Pitch Around the Leading Edge /147

To facilitate the calculation, we divided the wing surface roughly into three rectangular areas by the steady M distribution as shown in Figure 6. The results are shown in Figure 7. They are basically in agreement with the results obtained by the finite difference method. However, there are inadequacies such as the discontinuities of load values in the trailing edge of zone ① and leading edge of zone ②. It is expected that better results can be obtained by more accurately dividing the sub-super-subsonic regions based on the wing surface steady M number distribution and by increasing the chordwise control points in the supersonic region.

A review of the three examples above shows that this method is better. The cost for computation is less. Therefore, it is a practical approximation to analyze the transonic wing flutter and dynamic response characteristics to provide information on unsteady load distribution.

The work was enthusiastically guided by Professor Yang Zuosheng. The author wishes to express his gratitude.

References

- [1] Cunningham, A.M., Jr., A steady and oscillating kernel function method for interfering surface in subsonic, transonic and supersonic flow. NASA CR 144895.
- [2] Nanjing Institute of Aeronautics and Astronautics, Numerical Computation of the Aerodynamic Linearization Theory (1977).
- [3] Yang Zuosheng, Kernel Function for the Computation of Steady and Unsteady Load Distribution of Supersonic Sweptback Wings (1977), p. 119.
- [4] Landahl, M.T., Unsteady Transonic Flow (1961).
- [5] Liu, D.D., and Winter, B.A., Towards a mixed kernel function approach for unsteady transonic flow analysis, AD A 054028.
- [6] Warren H. Weatherill, James D. Sebastian and F. Edward Ehlers, The practical application of the finite difference method for analyzing transonic flow over oscillating airfoils and wing, NASA CR-2933.

A KERNEL FUNCTION METHOD FOR COMPUTING UNSTEADY LOAD ON THREE-DIMENSIONAL WINGS IN TRANSONIC FLOW

Wu Yizhao

(Nanjing Aeronautical Institute)

Abstract

A kernel function method and the results of computing unsteady load on three-dimensional wings in transonic flow are presented in this paper. The method is based on linearized lifting surface theory. Local linearization is used for treatment of unsteady transonic flow about wings. A line doublet which represents the additional lift induced by shock movement is adopted in simulating the presence of a normal shock, and the appropriate shock boundary conditions are embedded.

A new method dealing with the subsonic chord wise integration is introduced, and the procedures of numerical integration is simplified greatly. We also present procedures for calculation of downwashes. Both the

AD-A158 454

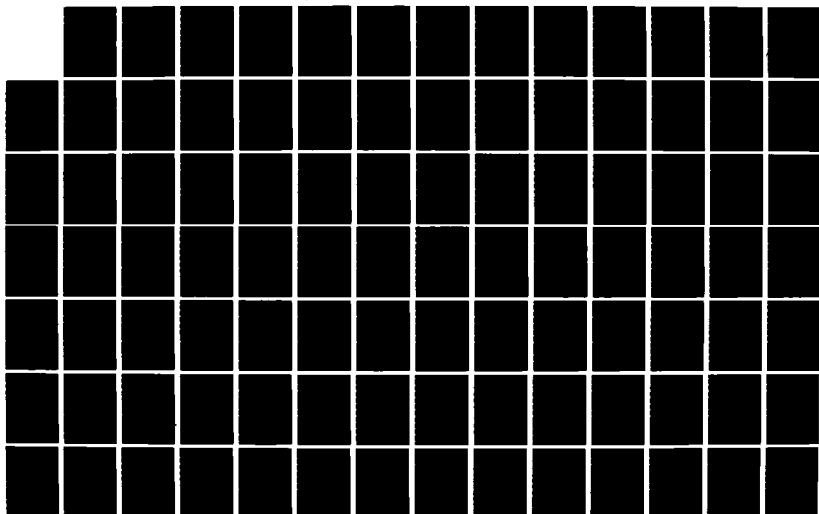
ACTA AERONAUTICA ET ASTRONAUTICA SINICA (SELECTED
ARTICLES)(U) FOREIGN TECHNOLOGY DIV WRIGHT-PATTERSON
AFB OH W JI ET AL. 85 AUG 85 FTD-ID(R5)T-1515-84

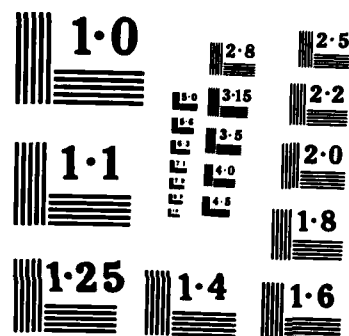
2/3

UNCLASSIFIED

F/G 1/3

NL





NATIONAL BUREAU OF STANDARDS
MICROCOPY RESOLUTION TEST CHART

Chinese Society of Aeronautics Held 1983 Academic
Activity Workshop

The Chinese Society of Aeronautics held its 1983 academic activity workshop on January 5, 1984 in Beijing. Vice President Dong Xiao delivered the spirits of the national scientific workshop. Twenty local secretaries of special field committees attended the meeting. Academic activities in 1983 were summarized. Suggestions to improve the quality of such activities were presented.

In addition to the Third National Meeting, the Chinese Society of Aeronautics also sponsored 29 academic exchange meetings, 7 workshops and 1 technical inquiry in 1983. It also held 3 technical training classes. A total of 1756 academic papers were received and 1248 of them were read in meetings. 3190 people attended various academic activities. As compared to 1982, there are significant increases in items and people. The quality is improved and the format is more flexible. There is an "open" atmosphere in academic discussion. Through academic activities, accomplishments and experience in scientific research, production, management, teaching and applications were exchanged. Future trends of worldwide technological development were investigated. Some suggestions were made to the relevant authorities in the areas of technological development, technical policy and exploitation. A healthy academic organization was built and future activities were planned.

Looking back into the academic activities in 1983, there are several special characteristics:

1. More than 80% of the academic activities belonged to medium and small scale special topic activities which tightly

combined the actual needs of the present aeronautic industry in research, production, management, teaching and applications.

2. Academic activities were concentrated on weak links and key subjects in the development of aeronautic and astronautic industries in China.

3. In addition to paying attention to the development of science, activities were initiated around the production and development of major equipment such as aircrafts and engines.

4. Activities in management were strengthened and good results were obtained.

After a year's work, everybody believes that academic activity is a good vehicle to train the technical staff. It is a good place and form to initiate technical inquiries. It encourages the technical collaboration among research, production, application and teaching outfits and promotes progress in scientific research. Especially in this "information explosion" era, strengthening academic activities is obviously significant.

Finally, everyone agreed that various activities of the Society in 1984 should be even better prepared for the 20th anniversary of the Society. Especially, we must thoroughly organize the "Scientific Report Conference in Honor of the 20th Anniversary of the Chinese Society of Aeronautics and Astronautics" which is focused on the prediction of aeronautic development in China by the year 2000.

Root Locus Method and Automatic Identification of Modes in Flutter Analysis

/149

Yang Xingjian (Institute of Aeronautical Computation
Technique)

Li Guangquan (Institute of Aircraft Structural Mechanics)

Abstract

In this work a program based on the root locus method for the analysis of wings with an active flutter suppression system was compiled. An automatic flutter mode identification method was investigated on an efficient, simple and easy to compile program for identification. The feasibility was demonstrated through examples.

Symbols

b_0	reference chord length
ρ	atmospheric density
ω	oscillating circle frequency
V	incoming flow velocity
k	($=b_0 \omega/V$) decrement frequency
s	Laplace variable
$\{q\}$	main mode coordinate matrix
$\{\beta\}$	generalized coordinate matrix of rotational mode on the active control surface
$[\bar{M}]$	generalized mass matrix
$[\bar{K}]$	generalized rigidity matrix
$[\bar{A}_1]$	real coefficient matrix of quasi-generalized aerodynamic force matrix
$[\hat{A}]$	generalized aerodynamic force matrix
$[\bar{A}]$	approximate aerodynamic force matrix on the Laplace plane

$[I_{\beta s}(S)]$ numerator matrix of the rational transfer function S between NB control surface rotating angles and N_s sensors

$[D(S)]$ denominator of rational transfer function S between NB control rotating angles and N_s sensors

$[\phi_{sq}]$ mode matrix at N_s sensor positions

subscripts:

q represents a generalized value related to the NQ major modes

β represents a generalized value related to the NB control surface rotating angles

s represents a value related to a displacement of NS sensors.

I. Introduction

/150

Over a long period of time, the most common method used to study flutter problems in unsteady aerodynamics is the V-g method. Because an imaginary damping is used in the V-g method, it is, in principle, not possible to provide any real attenuation information below the flutter velocity. However, computation formulas or numerical methods must be established for the so-called unsteady aerodynamic force (or instantaneous aerodynamic force) in order to estimate the actual attenuation in a subcritical state. A great deal of progress was made when a frequency domain simple harmonic aerodynamic force method was developed. The unsteady aerodynamic expression established by this method can be used in the stability analysis of aeroelastic systems by the widely used root locus method. The major feature of the root locus method is that the primary modes affecting flutter can be identified from the root locus curves. The real portion of the root can be used to determine the stability of the system. In addition, the effect of parameters can also be determined from these curves.

Furthermore, the so-called "dangerous mode determination" problem is often encountered when using the V-g method. Because the mode order is determined according to ω in the V-g method, the V-g mode will have to be interchanged after the cross-over of the ω -V curves. If two ω -curves cross over the ω -V diagram, then the sequence of the modes is simply determined by the numerical value of ω . In this case, errors such as Figures 1(a) and 1(b) will occur. The accurate curves should be Figures 1(c) and 1(d). These problems were noted in using the root locus method in this work. Several methods were studied to identify a simple, feasible way to determine the dangerous mode. A computer program for the root locus method was compiled on the 7760 computer to verify the feasibility using examples. Satisfactory results were obtained.

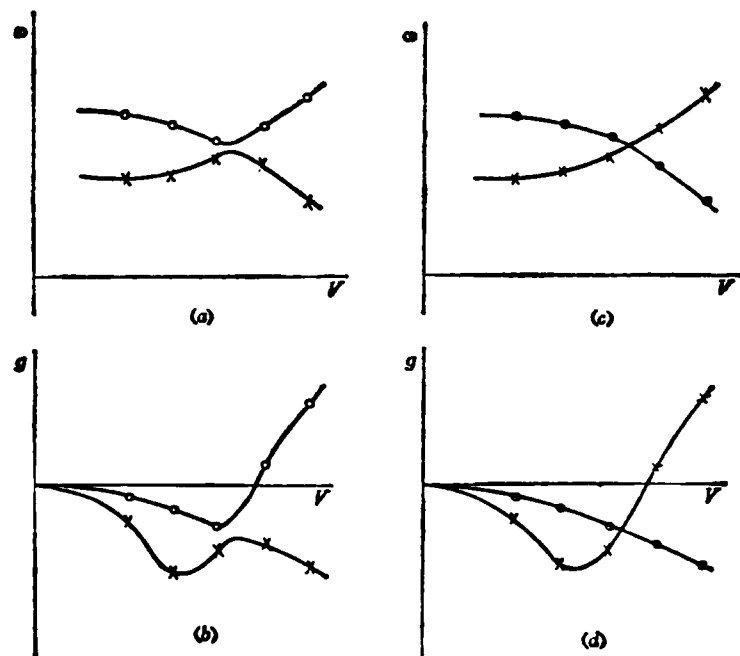


Figure 1. g - V - ω curves

(a), (b) wrong extensions
(c), (d) correct extensions

II. Computation Formulas for Unsteady Aerodynamic Force

/151

The effect of the motion of the control plane on the wing is usually expressed by a transfer function which is a polynomial of s . In order to extend the unsteady aerodynamic force to the

entire plane under a simple harmonic motion, it can be approximated by the following polynomial of s :

$$[\hat{A}(s)] = [\bar{A}_0] + [\bar{A}_1]s + [\bar{A}_2]s^2 + \sum_{m=3}^6 \frac{[\bar{A}_m]s}{s + \beta_{m-2}} \quad (1)$$

It is required that the aerodynamic coefficients of s at certain given points on ik be equal to the unsteady aerodynamic coefficients of the simple harmonic motion

$$[\bar{A}(k)] = [\bar{A}_0] + [\bar{A}_1](ik) + [\bar{A}_2](ik)^2 + \sum_{m=3}^6 \frac{[\bar{A}_m](ik)}{(ik) + \beta_{m-2}} \quad (2)$$

The approximate expression of the generalized aerodynamic torque matrix on the s plane, $[\hat{A}]$, can be obtained by using the least square iteration method to determine the coefficient matrices $[\bar{A}_0]$, $[\bar{A}_1]$, ..., $[\bar{A}_6]$. Where

$$[\bar{A}_i] = \begin{bmatrix} \bar{A}_{i,qq} & \bar{A}_{i,q\beta} \\ \bar{A}_{i,\beta q} & \bar{A}_{i,\beta\beta} \end{bmatrix} \quad i = 0, 1, 2, \dots, 6 \quad (A)$$

β_{m-2} is a given constant to be selected in the range of the decremental frequency range k in calculating the generalized aerodynamic matrix $[\bar{A}(k)]$.

III. Establishing the Flutter Equation

The flutter equation in this domain can be written as:

$$[\bar{K}_{qq}]\{q\} + s^2[\bar{M}_{qq}]\{q\} + \frac{1}{2} \rho V^2 [\hat{A}_{qq}]\{q\} + s^2[\bar{M}_{q\beta}]\{\beta\} + \frac{1}{2} \rho V^2 [\hat{A}_{q\beta}]\{\beta\} = 0 \quad (3)$$

where

$$\{\beta\} = \frac{[T_{\beta q}(s)][\phi_{q,q}]\{q\}}{D(s)} \quad (4)$$

$[T_{\beta q}(s)]/D(s)$ is a transfer function in the form of a rational polynomial of s . $[T_{\beta q}(s)]$ may be written as

$$[T_{\beta}(s)] = [T_r]s' + [T_{r-1}]s'^{-1} + \dots + [T_1]s + [T_0] \quad (B)$$

where $[T_r], [T_{r-1}], \dots, [T_0]$ are constant matrices. $D(S)$ is a polynomial of s :

$$D(s) = D_r s' + D_{r-1} s'^{-1} + \dots + D_1 s + D_0 \quad (C)$$

By substituting equations (1) and (4) into equation (3), the flutter equation is established:

$$\begin{aligned} (D(s)(A_0(s)[\bar{A}_q]s^2 + [\bar{B}_q]s + [\bar{C}_q]) + A_1(s)[\bar{D}_q] + A_2(s)[\bar{E}_q] \\ + A_3(s)[\bar{F}_q] + A_4(s)[\bar{G}_q]) + (A_0(s)[\bar{A}_\beta]s^2 + [\bar{B}_\beta]s \\ + [\bar{C}_\beta]) + A_1(s)[\bar{D}_\beta] + A_2(s)[\bar{E}_\beta] + A_3(s)[\bar{F}_\beta] \\ + A_4(s)[\bar{G}_\beta])[T_{\beta}][\phi_q]\{q\} = 0 \end{aligned} \quad (5)$$

where $A_i(s)$ ($i = 1, 2, \dots, 4$) is a function of s and V , $[\bar{A}_q]$ and $[\bar{A}_\beta]$ are functions of ρ , and $[\bar{B}_q], [\bar{C}_q], \dots, [\bar{G}_q], [\bar{B}_\beta], [\bar{C}_\beta], \dots, [\bar{G}_\beta]$ are functions of ρ and V .

Systems with and without an active flutter control unit are discussed separately in the following:

(1) without control ($[T_{\beta s}(S)] = 0$).

From equation (5) we know that the equation becomes the following where there is no control: /152

$$\begin{aligned} [A_0(s)([\bar{A}_q]s^2 + [\bar{B}_q]s + [\bar{C}_q]) + A_1(s)[\bar{D}_q] + A_2(s)[\bar{E}_q] + A_3(s)[\bar{F}_q] \\ + A_4(s)[\bar{G}_q]]\{q\} = 0 \end{aligned} \quad (6)$$

After expanding the above equation and combining the coefficients of the same order, it can be re-written as:

$$[[F_6]s^6 + [F_5]s^5 + \dots + [F_0]]\{q\} = 0 \quad (7)$$

The coefficient matrix $[F_i]$ ($i = 0, 1, 2, \dots, 6$) is a function of dynamic pressure and velocity at a given Mach number. By using the following relation

$$\{x\} = \begin{Bmatrix} s^5\{q\} \\ s^4\{q\} \\ \vdots \\ s^0\{q\} \end{Bmatrix}$$

equation (7) can be simplified as a first order equation series with 6 x NQ elements as follows:

$$s \{x\} = [A] \{x\} \quad (8)$$

The eigenvalue of equation (8) is the root of the flutter eigenfunction. Because the elements of the matrix $[F_i]$ are functions of dynamic pressure at a given Mach number, therefore, the variation of eigenvalue with dynamic pressure can be calculated for a specific Mach number to prepare the root locus plot.

2. With Control

When there is control, equation (5) can be rewritten as:

$$([H_m]s^m + [H_{m-1}]s^{m-1} + \dots + [H_1]s + [H_0])\{q\} = 0 \quad (9)$$

where $m = r + 6$. Similarly, equation (9) can be simplified and expressed as the following first order equations:

$$s \{x\} = [A_c] \{x\} \quad (10)$$

where

$$\{x\} = \begin{Bmatrix} s^{m-1}\{q\} \\ s^{m-2}\{q\} \\ \vdots \\ s^0\{q\} \end{Bmatrix}$$

$[A_c]$ is a $(m \times NQ) \times (m \times NQ)$ matrix. Similarly, if the variation of eigenvalue of equation (10) with dynamic pressure is solved then the root locus of the active control system can be plotted.

III. Automatic Identification of Flutter Mode and Flutter Point

From equations (8) and (9), one can see that additional roots are introduced because the order of the equation increases. These roots must be separated from the eigenvalues in computation. In this work, a Taylor expansion projection method

and a parabolic extrapolation projection method were used:

1. Taylor Expansion Projection Method:

The Taylor expansion method was used in references [6,7]. The major procedure is to project the eigenvalue $s'_{1,i+1}$ at a velocity $V_{i+1} = V_i + \Delta V$ by using the eigenvalue at $V \approx 0$ as the initial value and using a velocity increment ΔV as a step.

$$s'_{1,i+1} = s_{1,i} + (s_{1,i})_V \Delta V + \frac{1}{2} (s_{1,i})_{VV} \Delta V^2 \quad (11)$$

where the subscript 1 represents the 1th eigenvalue. The subscripts V and VV represent the first and second derivatives of the eigenvalue with respect to V, respectively. The difference between the calculated eigenvalue $s'_{1,i+1}$ and the projected eigenvalue $s'_{1,i+1}$ is restricted in a specific range by adjusting ΔV for automatic tracking. The point at which the eigenvalue is zero is the flutter point. /153

2. Parabolic Extrapolation Method

The parabolic extrapolation method is to fit root locus points with parabolic curves. The projected eigenvalue $s'_{1,i+1}$ on the fitted curve at V_{i+1} is compared with the eigenvalue $s'_{1,i+1}$ of equation (8) or (10) at V_{i+1} to track the mode. Essentially, the root locus is predicted by extrapolation. In practice, this is feasible when the step ΔV is not very large. As compared to the Taylor expansion method described before, its reliability is also comparable. The computation formula is as follows:

Assuming these points on the 1th root locus are $(V_{i-2}, s_{1,i-2})$, $(V_{i-1}, s_{1,i-1})$ and $(V_i, s_{1,i})$, then the projected eigenvalue at V_{i+1} is

$$s'_{1,i+1} = s_{1,i} + F_{32}(V_{i+1} - V_i) + F_{321}(V_{i+1} - V_i)(V_{i+1} - V_{i-1}) = s_{1,i} + F_{32} \Delta V_i + F_{321} \Delta V_i (\Delta V_i + \Delta V_{i-1}) \approx s_{1,i} + F_{32} \Delta V_i + 2F_{321} \Delta V_i^2 \quad (12)$$

where

$$\begin{aligned}
V_{i+1} &= V_i + \Delta V_i \\
V_i &= V_{i-1} + \Delta V_{i-1} \\
F_{32} &= (s_{1,i} - s_{1,i-1}) / (V_i - V_{i-1}) \\
F_{31} &= (F_{32} - F_{21}) / (V_i - V_{i-1}) \\
F_{21} &= (s_{1,i-1} - s_{1,i-2}) / (V_{i-1} - V_{i-2})
\end{aligned} \tag{A}$$

From equation (12) one can see that the parabolic extrapolation method is equivalent to using the difference quotient to replace the derivative in the Taylor expansion method. In the Taylor expansion method, the calculation of the derivatives of the eigenvalue s with respect to the velocity V , i.e., $(s_{1,i})_V$ and $(s_{1,i})_{VV}$, involves the first and second derivatives of the matrices in the eigenfunction of equation (8) or (10), as well as the eigenvector product. Hence, the work load is considerable. Results showed that the parabolic extrapolation method could accurately make predictions when the root locus is relatively smooth and the step is appropriate. Moreover, the efficiency of computation is significantly improved. Other steps in the identification process are similar to those in the Taylor expansion method.

IV. Example

A root locus program was compiled on the 7760 computer in order to compare these two mode identification methods. The NASATR 450 wing model^[3,4] was used as an example for computation. Figures 2-4 are the printouts of root locus curves (reduced). Figure 2 is the root locus curves without mode identification. We noticed that the third order mode (denoted as O) and the fourth order mode (denoted as X), as well as the fifth order mode (denoted as V) and the sixth order mode (denoted as M), are interchanged, which leads to confusion. Figure 3 shows the root locus curves obtained by mode identification

using Taylor expansion. Figure 4 shows the root locus curves obtained by parabolic extrapolation. We can see that the third and fourth order, as well as the fifth and sixth order, are apparently separated by mode identification. Furthermore, the effect of Taylor expansion and parabolic extrapolation was found to be identical. The computation by parabolic extrapolation took 561.31 seconds. The efficiency of the parabolic extrapolation method is thus three times better.

In this work, we received beneficial instruction from Professor Zhao Lingcheng and assistance from comrades Yang Yongnian and Mao Zhenghu. Their contribution is acknowledged.

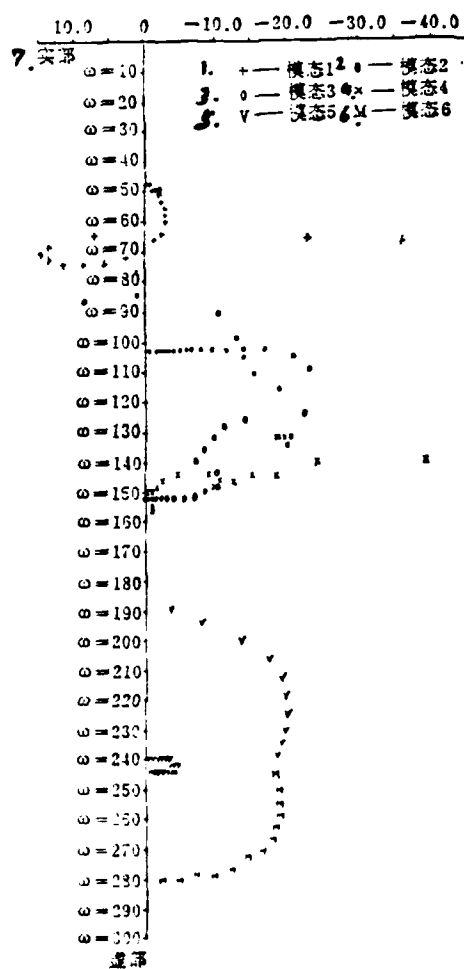


Figure 2. Root Locus Curve: without mode identification

- Key:
1. mode 1
 2. mode 2
 3. mode 3
 4. mode 4
 5. mode 5
 6. mode 6
 7. real part

- [5] Yang Guozhu, editor, Structure and Design of Aircraft Landing Gear, printed by Beijing Institute of Aeronautics and Astronautics, (1982).
- [6] Ling Xiaoling and Zhang Qixian, Retractable Landing Gear, Its Complicated Mechanism and Collision Detection, Journal of Beijing Institute of Aeronautics and Astronautics, No.2, (1982).

DETERMINATION OF THE AXIS AND THE ANGLE OF ROTATION FOR A RETRACTABLE LANDING GEAR

Zhang Qixian

(Beijing Institute of Aeronautics and Astronautics)

Abstract

The present paper deals with the analytical determination of the axis and the angle of rotation for a retractable landing gear. To facilitate the use of computer, the so-called rotation matrix $[A]$ about a skew axis PP is worth applying. If the coordinates of three points, say A , B and C , of a rigid body before and after rotation about an axis through point P are known, the rotation matrix $[A]$ can be easily calculated as follows:

$$[A] = \begin{bmatrix} x_{A_2} - x_P & x_{B_2} - x_P & x_{C_2} - x_P \\ y_{A_2} - y_P & y_{B_2} - y_P & y_{C_2} - y_P \\ z_{A_2} - z_P & z_{B_2} - z_P & z_{C_2} - z_P \end{bmatrix} \begin{bmatrix} x_{A_1} - x_P & x_{B_1} - x_P & x_{C_1} - x_P \\ y_{A_1} - y_P & y_{B_1} - y_P & y_{C_1} - y_P \\ z_{A_1} - z_P & z_{B_1} - z_P & z_{C_1} - z_P \end{bmatrix}^{-1}$$

where subscripts 1 and 2 stand for points before and after rotation respectively. Here a simple technique for obtaining the third point C from the two given points A and B of a rigid body is introduced. Any arbitrary point on the line passing through P and perpendicular to the plane formed by two given straight lines PA and PB can be taken as the point C .

In addition, some improvement in calculating the axis and the angle of rotation has been made. A numerical example of landing gear problem is included at the end of the paper.

The results obtained may be applied to design of retractable mechanisms for antennas and sensors on spacecraft as well.

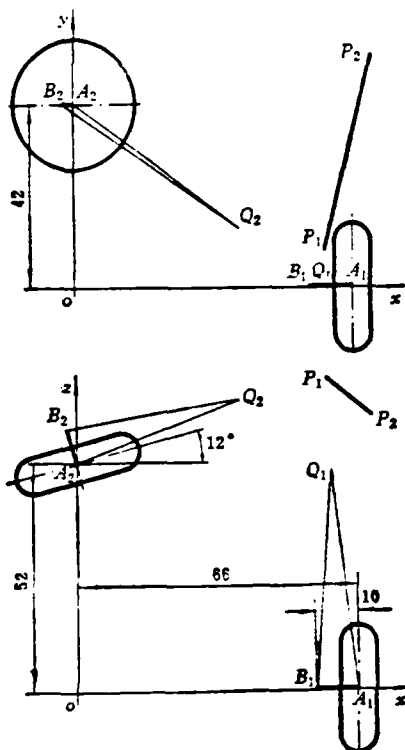


Figure 3. Numerical example of landing-gear problem

References

- [1] Garvey, S.J. and Hetzel, K.W., Analytical Geometry in Common Layouts 1. The Case of Retraction of an Under-carriage About a Single Axis, Aircraft Engineering, May, (1943), pp132-134.
- [2] Liming, R.A., Analytic Definition of a Retractable Landing Gear Axis of Rotation, J. of Aeronautical Science, Vol. 14, Jan. (1947), pp19-23.
- [3] Bisshopp, K.E., Finite Rotations of a Rigid Body and the Airplane Landing-Gear Problem, J. of Mechanisms, Vol. 3, (1968), pp203-208. /162
- [4] Suh, C.H. and Radcliffe, C.W., Kinematics and Mechanism Design, John Wiley & Sons (1978).

be 0: 8.09783:25.74018 and 25.17769:-8.09784:5.35168. Hence, $\phi = \cos^{-1} 0.09913 = 84.31104^\circ$.

When we calculated the coordinate of Q_2 , the rotation matrix [A] was first obtained from equation (4). Finally, equation (6) was used to get $x_{Q_2} = 38.85079$, $y_{Q_2} = 13.37336$ and $z_{Q_2} = 66.39205$. /161

$$[A] = \begin{bmatrix} 0.20791 & 0.56002 & 0.80197 \\ 0.00000 & 0.81988 & -0.57253 \\ -0.97815 & 0.11904 & 0.17046 \end{bmatrix} \quad (A)$$

Finally, it is worthwhile to point out that equations (7) and (8) may also be used to find the solution of this example. In this case, if $z_P = 0$ then the coordinates of P are $x_P = 147.53878$ and $y_P = 233.17999$. Then, the rotation matrix [A] can be obtained using equations (8) - (11) as

$$[A] = \begin{bmatrix} 0.20791 & 0.56009 & 0.80224 \\ 0 & 0.81997 & -0.57273 \\ -0.97815 & 0.11901 & 0.17052 \end{bmatrix} \quad (B)$$

Then, $\phi = 84.30678$, $u_x = 0.34758$, $u_y = 0.89460$ and $u_z = -0.28143$ from equation (7). Both methods brought very close results.

where the subscripts 1 and 2 represent the directional cosines relating to \overrightarrow{HN}_1 and \overrightarrow{HN}_2 , respectively. The directional coefficients of \overrightarrow{HN} can be calculated in analogy to equation (9). For example, the subscripts P_2 and P_1 can be used to replace A and P in line 2, and B and A instead of B and P in line 3.

If the position of any other point on the landing gear support (e.g., roller support, upper lock latch or center of gravity of support) must be determined, the rotation matrix [A] can be calculated first and then proceed with equation (6).

IV. Example

For ease of comparison, the landing gear used in reference [3] was used as an example. As shown in Figure 3, when the wheels are lowered, the coordinate for the center of wheel A_1 is $[66 \ 0 \ 0]^T$, and the directional cosine of $\overrightarrow{A_1B_1}$ is $[-1 \ 0 \ 0]^T$; when the wheels are retracted, A_2 is $[0 \ 42 \ 52]^T$ and the directional cosine of $\overrightarrow{A_2B_2}$ is $[-\sin 12^\circ, 0 \ \cos 12^\circ]^T$. It is also known that the coordinate of a point Q_1 on the support when the landing gear is lowered is $[60 \ 0 \ 50]^T$. It is required to determine the rotational axis P_1P_2 , the angle of rotation ϕ and the coordinate Q_2 on the support when the landing gear is retracted.

Arbitrarily, let us choose AB to be 10 in length. Then, the coordinates of B_1 and B_2 are $[56 \ 0 \ 0]^T$ and $[-2.07912 \ 42 \ 61.78148]^T$ respectively. Using equations (1) and (2) we get

$$-66x_p + 42y_p + 52z_p = 56$$

$$-58.07912x_p + 42y_p + 61.78148z_p = 1224.6370$$

In order to conveniently show the axis of rotation P_1P_2 on paper, we arbitrarily choose $x_{p_1} = 60$ and $x_{p_2} = 70$. Therefore, $y_{p_1} = 7.85363$, $z_{p_1} = 70.88745$, $y_{p_2} = 33.59381$, and $z_{p_2} = 62.78962$. Hence, the directional cosines of the axis of rotation P_1P_2 are $u_x = 0.34750$, $u_y = 0.89446$ and $u_z = -0.28140$.

In order to find the angle of rotation ϕ using equation (12), the directional coefficients of \overrightarrow{HN}_1 and \overrightarrow{HN}_2 were found to

(4) Specifying 3 coordinates for A_1 , 2 coordinates for A_2 and B_2 , length of AB, directional cosines of A_1B_1 , and projection of A_2B_2 on a certain coordinate plane.

In the design, all coordinates of A_1 , A_2 , B_1 and B_2 are determined using equations (1) - (3). Then, C_1 and C_2 are /160 obtained from equations (9) - (11). Finally, the rotation matrix $[A]$ is calculated using equation (8). The axis and angle of rotation can then be calculated using equation (7).

2. Point P to Be Determined

Because of equations (1) and (2), an arbitrary coordinate can be assigned to P when this point is still to be determined. As for A_1 , A_2 , B_1 and B_2 , because equation (3) must be satisfied, not only 11 coordinates but also the 6 coordinates of A_1 and A_2 , the length of AB (arbitrary) and the directional cosines of A_1B_1 and A_2B_2 can be obtained.

In the design, if the plane of the rotation axis is already known, then one coordinate of P can be specified and the other two can be found. If there is no special requirement, it is possible to make $x_{P_1} = 0$ and $y_{P_2} = 0$ when we determine the axis of rotation from P_1 and P_2 to simplify the computation. The direction and coefficients of P_1 and P_2 are: $x_{P_2} - x_{P_1}$, $y_{P_2} - y_{P_1}$ and $z_{P_2} - z_{P_1}$. The directional cosines of the axis of rotation and the angles between the projections of the axis of rotation on the coordinate planes with various axes can be further determined. For example, the angle between the projection of the rotational axis on the xz plane and the x axis $\alpha = \text{tg}^{-1} (z_{P_2} - z_{P_1}) / (x_{P_2} - x_{P_1})$.

In order to determine the angle of rotation ϕ , we suggest to use the minimum distance line HN (common normal line) between the rotational axis PP and straight line AB. The computation formula is

$$\phi = \cos^{-1}(n_{x_1}n_{x_2} + n_{y_1}n_{y_2} + n_{z_1}n_{z_2}) \quad (12)$$

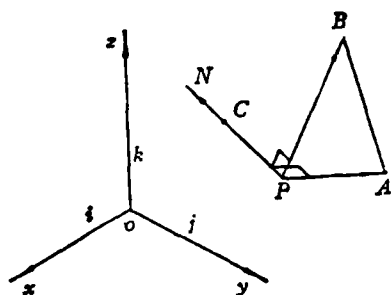


Figure 2. Determination of point C from points P, A & B

III. Determination of Axis and Angle of Rotation of Retractable Landing Gear

1. Pre-determined P point Design

When the aforementioned rigid body rotation is used in the design of a retractable landing gear, the straight line AB is equivalent to the center line of the aircraft wheels. The so-called pre-determined point P is the intersect of the axis of rotation with the beam, web plate, reinforcing rib or skeletal plane. From equations (1) - (3) we know that the designer can freely specify 9 out of the 12 coordinates for points A_1 , A_2 , B_1 and B_2 . The procedures are as follows:

(1) Specifying 5 coordinates for points A_1 and A_2 and 4 coordinates for B_1 and B_2 (or vice versa);

(2) Specifying 5 coordinates for A_1 and A_2 , 1 coordinate for B_1 , length of AB, projection of A_1B_1 on a certain coordinate plane and projection of A_2B_2 on another coordinate plane;

(3) Specifying all 6 coordinates of A_1 and B_1 , 2 coordinates of A_2 and B_2 , and projection of A_2B_2 on a certain plane;

3. Determination of Rotational Matrix [A]

Let us assume that P is a point on a rigid body. If the coordinates of three points, A, B and C, on the rigid body before and after rotation are known, then the matrix [A] can be obtained from equation (6).

$$[A] = \begin{bmatrix} x_{A_2} - x_P & x_{B_2} - x_P & x_{C_2} - x_P \\ y_{A_2} - y_P & y_{B_2} - y_P & y_{C_2} - y_P \\ z_{A_2} - z_P & z_{B_2} - z_P & z_{C_2} - z_P \end{bmatrix} \begin{bmatrix} x_{A_1} - x_P & x_{B_1} - x_P & x_{C_1} - x_P \\ y_{A_1} - y_P & y_{B_1} - y_P & y_{C_1} - y_P \\ z_{A_1} - z_P & z_{B_1} - z_P & z_{C_1} - z_P \end{bmatrix}^{-1} \quad (8)$$

In reality, if the point P is on the axis of rotation of the rigid body, then the coordinates of two points A and B before and after rotation are required. In this case, we should find the coordinates of another point C on the rigid body before and after rotation. As for the method to determine point C from points A and B, it was introduced here. As shown in Figure 2, a line \vec{PN} normal to the plane formed by PA and PB is drawn through point P. An approximate length l is selected on this normal line (such as 1 or 10) to locate the point C. The directional coefficients N_x , N_y and N_z of \vec{PN} can be obtained from the following determinant. /159

$$\vec{PN} = \begin{vmatrix} i & j & k \\ x_A - x_P & y_A - y_P & z_A - z_P \\ x_B - x_P & y_B - y_P & z_B - z_P \end{vmatrix} = N_x i + N_y j + N_z k \quad (9)$$

The corresponding directional cosines of PN are:

$$(n_x, n_y, n_z) = (N_x, N_y, N_z) / \sqrt{N_x^2 + N_y^2 + N_z^2} \quad (10)$$

Hence, the coordinate of point C can be calculated as follows:

$$x_c = x_P + l n_x, \quad y_c = y_P + l n_y, \quad z_c = z_P + l n_z \quad (11)$$

2. Rotational Matrix of a Rigid Body about a Skew Axis

In order to facilitate matrix operation, the rotational matrix $[A]$ of a rigid body about a skew axis can be written as the following according to rigid body kinematics^[4].

$$[A] = \begin{bmatrix} u_x^2 V\phi + C\phi & u_x u_y V\phi - u_x S\phi & u_x u_z V\phi + u_y S\phi \\ u_x u_y V\phi + u_x S\phi & u_y^2 V\phi + C\phi & u_y u_z V\phi - u_x S\phi \\ u_x u_z V\phi - u_y S\phi & u_y u_z V\phi + u_x S\phi & u_z^2 V\phi + C\phi \end{bmatrix} \quad (4)$$

where u_x , u_y and u_z are the directional cosines of the skew axis and ϕ is the angle of rotation of the rigid body about the axis, $V\phi = 1 - \cos\phi$, $C\phi = \cos\phi$, and $S\phi = \sin\phi$.

In practice, the rotation matrix $[A]$ is sometimes expressed as follows:

$$[A] = \begin{bmatrix} u_x^2 & u_x u_y & u_x u_z \\ u_x u_y & u_y^2 & u_y u_z \\ u_x u_z & u_y u_z & u_z^2 \end{bmatrix} + C\phi \begin{bmatrix} 1 - u_x^2 & -u_x u_y & -u_x u_z \\ -u_x u_y & 1 - u_y^2 & -u_y u_z \\ -u_x u_z & -u_y u_z & 1 - u_z^2 \end{bmatrix} + S\phi \begin{bmatrix} 0 & -u_z & u_y \\ u_z & 0 & -u_x \\ -u_y & u_x & 0 \end{bmatrix} \quad (5)$$

The first two terms are symmetric matrices and the third one is asymmetric.

The position of any point on the rigid body after rotation can be determined by the rotation matrix $[A]$. Let us assume that \vec{r}_p is the coordinate vector of a point on the axis of rotation, and \vec{r}_1 and \vec{r}_2 are respectively coordinate vectors of the same point on the rigid body before and after rotation. Then, there is the following relationship.

$$[\vec{r}_2] = [\vec{r}_p] + [A][\vec{r}_1 - \vec{r}_p] \quad (6)$$

If the rotation matrix $[A]$ of the rigid body is known, the angle of rotation and the directional cosines of the rotational axis can be directly calculated from the matrix elements a_{ij} if the angle of rotation is not too small, i.e.,

$$\left. \begin{aligned} \phi &= \cos^{-1}[(a_{11} + a_{22} + a_{33} - 1)/2] \\ u_x &= \frac{a_{32} - a_{23}}{2S\phi}, \quad u_y = \frac{a_{13} - a_{31}}{2S\phi}, \quad u_z = \frac{a_{21} - a_{12}}{2S\phi} \end{aligned} \right\} \quad (7)$$

II. Finite Rotation of Rigid Body

1. Relation of a straight line on a Rigid Body before and after Rotation

In Figure 1, a straight line AB on a solid body is rotated about a skew axis PP by an angle ϕ from

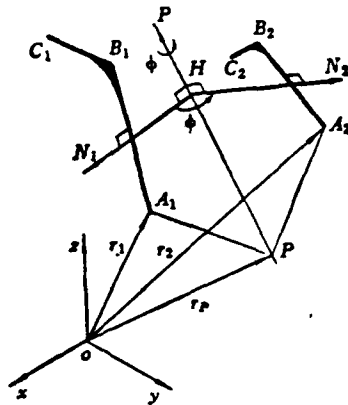


Figure 1. A finite rotation of rigid body ABC about skew axis PP

A_1B_1 to A_2B_2 . Obviously, $PA_1 = PA_2$, $PB_1 = PB_2$, $A_1B_1 = A_2B_2$. The following expressions can be obtained by the coordinates of relevant points

$$\begin{aligned} (x_{A_2} - x_{A_1})x_P + (y_{A_2} - y_{A_1})y_P + (z_{A_2} - z_{A_1})z_P \\ = 0.5[(x_{A_2}^2 + y_{A_2}^2 + z_{A_2}^2) - (x_{A_1}^2 + y_{A_1}^2 + z_{A_1}^2)] \end{aligned} \quad (1)$$

$$\begin{aligned} (x_{B_2} - x_{B_1})x_P + (y_{B_2} - y_{B_1})y_P + (z_{B_2} - z_{B_1})z_P \\ = 0.5[(x_{B_2}^2 + y_{B_2}^2 + z_{B_2}^2) - (x_{B_1}^2 + y_{B_1}^2 + z_{B_1}^2)] \end{aligned} \quad (2)$$

$$\begin{aligned} (x_{A_2}x_{B_2} + y_{A_2}y_{B_2} + z_{A_2}z_{B_2}) - (x_{A_1}x_{B_1} + y_{A_1}y_{B_1} + z_{A_1}z_{B_1}) \\ = 0.5[(x_{A_2}^2 + y_{A_2}^2 + z_{A_2}^2) + (x_{B_2}^2 + y_{B_2}^2 + z_{B_2}^2) \\ - (x_{A_1}^2 + y_{A_1}^2 + z_{A_1}^2) - (x_{B_1}^2 + y_{B_1}^2 + z_{B_1}^2)] \end{aligned} \quad (3)$$

Determination of Axis and Angle of Rotation of Retractable*
Landing Gear

Zhang Qixian

(Beijing Institute of Aeronautics and Astronautics)

Abstract

In this work, the axis and rotation of retractable landing gears was determined analytically. In addition to solving the rotational matrix of a rigid body about a skew axis, some improvements were made in solving the rotational axis and angle of rotation. An example of aircraft landing gear was included. The contents might also be used in the design of retractable antennas and sensors in aircraft.

I. Introduction

The design of retractable landing gear, antennas and sensors on aircraft and space craft very frequently involves the determination of the axis and angle of rotation. For example, the orientation of the axis of rotation, the angle of rotation, and the position of the support point must be known. These problems can generally be solved by analytical geometry or vector operation methods^[1-3]. In this work, the rotational matrix of a rigid body about a skew axis was used to solve these problems in order to facilitate the use of computers. Furthermore, two points on the axis of rotation were used to determine the axis of rotation and to calculate the angle of rotation by using the cosine in the normal direction (to satisfy structural requirements or to facilitate the computation). The method used here is also different from the one reported in reference [6].

*received in June, 1983

ROOT LOCUS METHOD AND AUTOMATIC IDENTIFICATION OF MODES IN FLUTTER ANALYSIS

Yang Xingjian

(Aeronautical Computation Technique Institute)

Li Guangque

(Aircraft Structural Mechanics Research Institute)

Abstract

A flutter analysis based on root locus method is programmed. It can be applied to a wing equipped with an active flutter suppression system. An automatic identification method of flutter modes is proposed which has the advantages of high efficiency in computation, brief algorithms and simplicity in programming. Numerical examples show that the method is feasible.

- [1] William, P. Rodden et al. Aeroelastic Addition to NASTRAN, Final Report, NASA CR-3094 (1979).
- [2] Lotze, A., Sensburg, O. Uuhn, M., Flutter Investigation of a Combat Aircraft with a Command and Stability Augmentation System, J. Airc., (1977), 4, pp368-374.
- [3] Maynard C., Sandford, Irving Abel, and David L. Gray, "Development and Demonstration of A Flutter-Suppression System Using Active Controls", NASA TR450, (1975).
- [4] Yang Xingjian and Li Guanquan: "Solving Flutter Equation by P-K Method", Research Report of Aircraft Structural Mechanics Research Institute, (1983), 3.
- [5] Irving Abel, "An Analytical Technique for Predicting the Characteristics of a Flexible Wing Equipped with an Active Flutter-Suppression System and Comparison with Wind-Tunnel Data" NASA Technical paper 1367.
- [6] Lu Shuquan, Spatial Aeroelastic Model and Its Application in Flutter Computation, Technical Report of Nanjing Institute of Aeronautics, (1982), 6.
- [7] Rudisill, C.S. and Bhatia, K.G., Second Derivatives of the Flutter Velocity and the Optimization of Aircraft Structures, AIAA.J., Vol. 10, No. 12, (1972).
- [8] Rudisill, C.S. and Yee-Yeen Chu, Numerical Methods for Evaluating the Derivatives of Eigenvalues and Eigenvectors, AIAA, J., Vol. 13, No. 6, (1975).

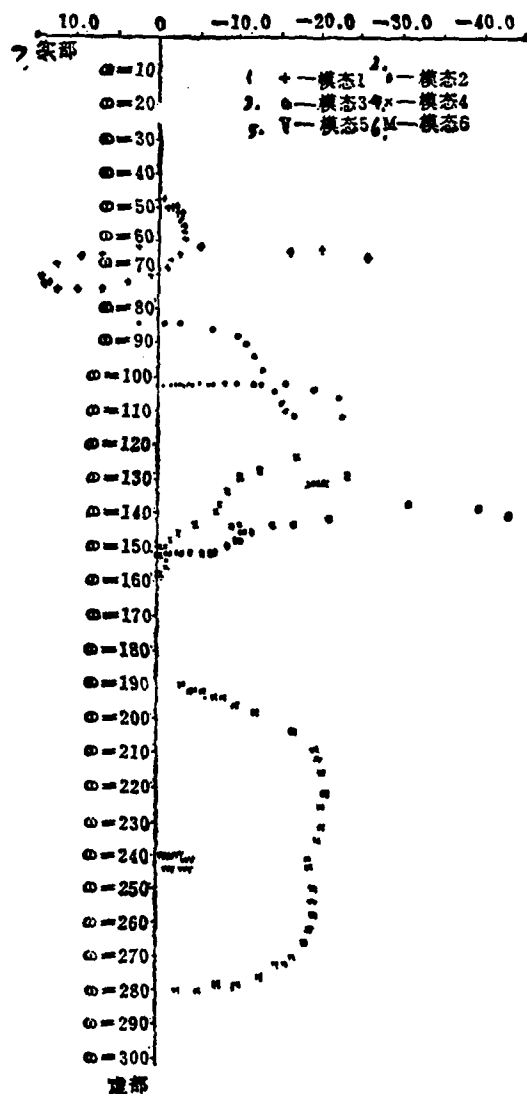


Figure 4. Root Locus Curves for the parabolic identification method of modes

Key:

- 1. mode 1
- 2. mode 2
- 3. mode 3
- 4. mode 4
- 5. mode 5
- 6. mode 6
- 7. real part

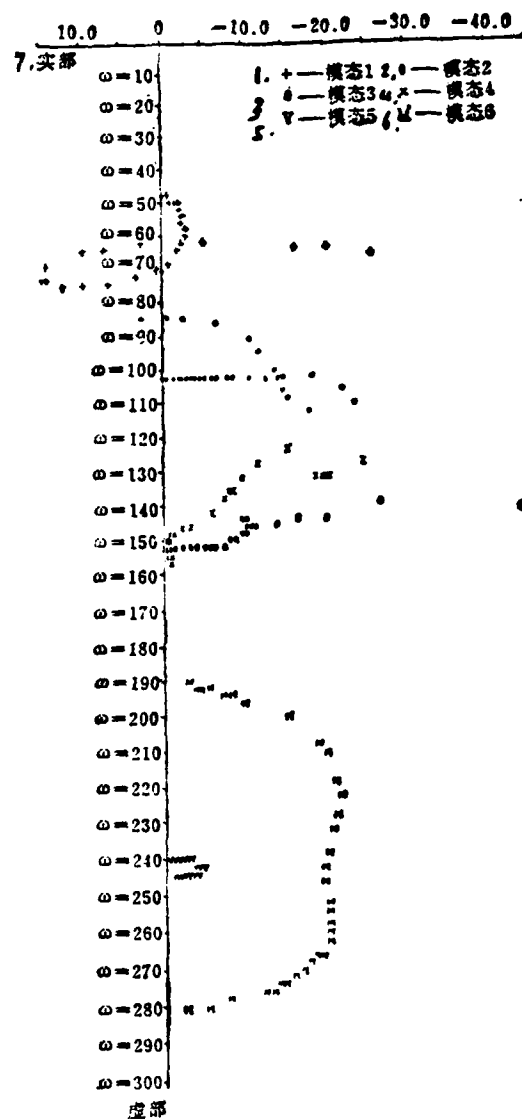


Figure 3. Root Locus curves for the Taylor identification method of modes

Key:

1. mode 1
2. mode 2
3. mode 3
4. mode 4
5. mode 5
6. mode 6
7. real part

δ Function and Generalized Tables of Thermodynamic Properties
of Combustion Products of $C_n H_m$ -Air System*

Fan Zuomin

(Gas Turbine Research Institute)

Fu Xunquan

(Power Plant Research Laboratory, Beijing Research Institute)

Abstract

In this work, a new thermodynamic property - δ function was introduced. $\delta = \theta_2 - \theta_1$, where θ_1 and θ_2 are δ functions of two arbitrary reference fuels.

The δ function is only dependent on temperature for the $C_n H_m$ -air system. It is independent of hydrogen-carbon ratio of the fuel and the fuel-air ratio. With the aid of the δ function, generalized tables of thermodynamic properties of combustion products for fuels of any hydrogen to carbon ratio were generated. These tables could be conveniently used in the accurate calculation of the thermodynamic properties of combustion products of the $C_n H_m$ -air system. Samples of such tables were given in this paper.

Introduction

It was pointed out in references [1] and [2] that the thermodynamic properties of complete combustion products of a specific fuel and air mixture at any mixing ratio could be expressed as functions of the thermodynamic properties of air and the so-called θ function (which was not called the θ -function in reference [1]) when the effect of thermal decomposition was neglected. This θ -function is only dependent on temperature and independent of the fuel mixing ratio. Therefore, as long as the thermodynamic properties of pure air and the θ function are given in the table, the thermodynamic properties of the combustion products at any fuel ratio can be calculated. Such tables were

*received in Nov. 1983

given in references [1] and [3]. But, the θ function is still dependent on the hydrogen to carbon ratio of the fuel. In this work, it is pointed out that the θ function of any hydrocarbon fuel can be expressed in terms of the θ function of a specific fuel (baseline θ function) and the δ function. The baseline function, however, is only a function of temperature. It is independent of the carbon to hydrogen ratio of the fuel. The thermodynamic properties of the combustion products of a fuel of any hydrogen to carbon ratio at any fuel to air ratio can be tabulated by using this δ function. It is more convenient to use the δ function than the thermodynamic properties of two reference fuels (referring to reference [4]) to calculate the thermodynamic properties of the combustion products of a fuel of an arbitrary composition.

II. The δ Function Using Weight as the Unit

The products of complete combustion of 1 kg of air and f kg of $C_n H_m$ can be considered as being composed of pure air and the theoretical combustion products of two reference fuels $C_{n_1} H_{m_1}$ and $C_{n_2} H_{m_2}$ (equivalent ratio $\phi = 1$) with pure air. Assuming that the appropriate stoichiometric fuel to air ratios are $f_{st,1}$ and $f_{st,2}$, then we can write the following:

$$\begin{aligned} & 1 \text{ kg Air} + f \text{ kg } C_n H_m \rightarrow (\alpha \text{ kg Air} + \alpha f_{st,1} \text{ kg } C_{n_1} H_{m_1}) \\ & \text{combustion gas} + (\beta \text{ kg Air} + \beta f_{st,2} \text{ kg } C_{n_2} H_{m_2}) \text{ combustion gas} + \\ & (1-\alpha-\beta) \text{ kg Air} \end{aligned} \quad (1)$$

and

$$\alpha f_{st,1} C_{h,1} + \beta f_{st,2} C_{h,2} = f C_f \quad (2)$$

$$\alpha f_{st,1} H_{h,1} + \beta f_{st,2} H_{h,2} = f H_f \quad (3)$$

where C_f and H_f are the carbon and hydrogen weight in the fuel, respectively.

From equations (2) and (3), we get

$$\alpha f_{st,1} + \beta f_{st,2} = f \quad (4)$$

$$\beta = \frac{f}{f_{st,2}} \frac{C_f - C_{h,1}}{C_{h,2} - C_{h,1}} \quad (5)$$

and

$$\alpha = \frac{f}{f_{st1}} \frac{C_f - C_{h2}}{C_{h1} - C_{h2}} \quad (6)$$

From equation (1) we get

$$(1 + f)y = (1 - \alpha - \beta)y_a + \alpha(1 + f_{st1})y_{st1} + \beta(1 + f_{st2})y_{st2} \quad (7)$$

where y represents a thermodynamic property (e.g., specific heat c_p , internal energy u , enthalpy h or entropy $\phi = \int_0^T C_p/T dT$) of a combustion product.

The subscripts a , 1 and 2 correspond to air, first reference fuel and second reference fuel, respectively. The subscript st represents the stoichiometric fuel to air ratio.

By substituting equations (4), (5) and (6) into equation (7), we get

$$y = y_a + \frac{f}{1 + f}(\theta_1 + a\delta) \quad (8)$$

where

$$\theta = \frac{1 + f_{st}}{f_{st}}(y_{st} - y_a) \quad (9)$$

$$\delta = \theta_2 - \theta_1 \quad (10)$$

and

$$a = \frac{C_f - C_{h1}}{C_{h2} - C_{h1}} \quad (11)$$

y_a , θ_1 , and δ are independent of the hydrogen to carbon ratio of the fuel and the equivalence ratio of the combustion products. Hence, equation (8) shows the thermodynamic property of an arbitrary fuel at any equivalence ratio can be determined by three thermodynamic parameters, i.e., y_a , θ_1 and δ , which only depend on temperature.

For a given fuel composition, the thermodynamic properties of its combustion products are independent of the reference fuel. If we choose this fuel as the first reference fuel and omit the subscript 1 from θ_1 to distinguish it from the θ_1 in equation (8), then

$$y = y_a + \frac{f}{1 + f} \theta \quad (12)$$

From equations (8) and (10), we get

$$\theta = \theta_1 + a\delta \quad (13)$$

Equation (13) shows that the θ function of an arbitrary fuel composition can be expressed as a function of the reference function and the δ function.

The choice of the reference fuel should satisfy the following principles:

1. The hydrogen to carbon ration difference between the two reference fuels should be as large as possible to minimize possible error.

2. The calculation of the value of a should be done as simply as possible.

3. The first reference fuel should be a commonly used one because the computation of the thermodynamic properties of the first reference fuel is simple ($a = 0$).

/165

For gasoline or kerosene type of fuels, C_nH_{2n} and H_2 were chosen as the first and second type reference fuel, respectively, in order to satisfy the above requirements. In this case, we can get the following from equation (11)

$$a = 1 - \frac{C_1}{C_{h1}} = \frac{m-2n}{m+rn} = \frac{x-2}{x+r} \quad (14)$$

where $x = m/n$ and r is the carbon to hydrogen atomic ratio ($r = 11.9162$).

III. The δ Function Using Mole as the Unit

We shall use Y , Θ , Δ and ϕ to represent the thermodynamic properties (corresponding to y , θ , δ and ϕ , respectively using weight units) using molar units. From equation (1), we get

$$Y = \frac{m_g}{1+f} (N_s Y_s + N_{m1} Y_{m1} + N_{m2} Y_{m2}) \quad (15)$$

where m_g is the molecular weight of the combustion product, and

$$N_s = \frac{1+f}{m_g} - N_{m1} - N_{m2} \quad (16)$$

$$N_{m1} = \frac{a(1+f_{m1})}{m_{m1}} = f(1-a) \frac{1+f_{m1}}{m_{m1}f_{m1}} \quad (17)$$

and

$$N_{m,2} = \frac{\beta(1+f_{m,2})}{m_{m,2}} = f_a \frac{1+f_{m,2}}{m_{m,2}f_{m,2}} \quad (18)$$

are the molar numbers of the combustion products as divided according to equation (1).

By substituting equations (16) to (18) into equation (15), we get

$$Y = Y_s + C(\Theta_1 + a\Delta) \quad (19)$$

where

$$\Theta = \frac{m_{m,1}}{m_{m,2}} \frac{1+f_{m,2}}{f_{m,2}} (Y_{m,2} - Y_s) \quad (20)$$

$$\Delta = \Theta_2 - \Theta_1 \quad (21)$$

$$C = \frac{m_s}{m_{m,1}} \frac{f}{1+f} \quad (22)$$

Equation (19) may also be rewritten as

$$Y = Y_s + C\Theta \quad (23)$$

$$\Theta = \Theta_1 + a\Delta \quad (24)$$

Equations (19) and (8) are identical in form. But, calculating the coefficient C in equation (19) is more complicated than calculating the corresponding coefficient in equation (8). The computation can be reduced by tabulating the coefficient C. However, the value of C is dependent on the hydrogen to carbon ratio and the equivalence ratio. Therefore, a large table will be needed. Otherwise, we will have to interpolate which leads to additional error. On the other hand, it is more convenient to use thermodynamic properties of combustion products with weight units in energy and combustion equations. Therefore, it is generally better off to use thermodynamic properties of combustion products using weight units. However, the entropy equation is in the form of

$$\frac{p_2}{p_1} = e^{(\bar{s}_2 - \bar{s}_1)} \quad (25) \quad /166$$

where $\bar{\psi} = \psi/R = m_g \phi/R$ and $R = 1.9858 \text{ kcal}/(\text{kgmol.K})$ is the generalized gas constant. For this reason, it is more convenient to use $\bar{\psi}$ in the entropy equation. However, it is more involved to calculate the value of $\bar{\psi}$ using equation (19) than calculating the value of ϕ using equation (8). Therefore, the amount of computation is more or less the same in calculating the entropy equation with $\bar{\psi}$ as with ϕ . When the hydrogen to carbon ratio $m/n = 2.0$, the value of C can be accurately calculated according to $f/(1 + f)$. Under such conditions, it is more convenient to use $\bar{\psi}$ in the calculation. According to equation (19), we get

$$\bar{\psi} = \bar{\psi}_s + C(\bar{\theta}_{s,1} + a\bar{\Delta}_s) \quad (\text{A})$$

where

$$\bar{\psi}_s = \psi_s/R, \quad \bar{\theta}_{s,1} = \theta_{s,1}/R \text{ 及 } \bar{\Delta}_s = \Delta_s/R. \quad (\text{B})$$

IV. Generalized Table of Thermodynamic Properties of Combustion Products of the C_nH_m -Air System

With the aid of the δ function, we prepared a series of generalized tables of thermodynamic properties of combustion products for the C_nH_m -air system. These tables are applicable to fuels of any hydrogen to carbon ratio. The first and second reference fuels are C_nH_{2n} and H_2 ($m_{st,1} = 28.9050 \text{ kg/mol}$), respectively. The entropy was calculated from a starting temperature of 298.15K. In addition to providing the thermodynamic properties of air, θ function and δ function, isothermal combustion enthalpy difference $d^{[5]}$ and the thermodynamic properties of steam such as $c_{p,w}$, h_w and ϕ_w are also given. The first part can be calculated by a simplified combustion equation. In the latter part, the effect of the initial moisture content in the air could be included. Table 1 shows a portion of the main table. To simplify the situation, the subscript 1 under the reference θ function is omitted.

Table 1. Specimen of Thermodynamic Properties Table for C_nH_m -air System Combustion Products

T K	$c_{p,a}$ kcal/(kg·k)	$\theta_{c,p}$ kcal/(kg·k)	$\delta_{c,p}$ kcal/(kg·k)	h_a kcal/kg	θ_h kcal/kg	δ_h kcal/kg	α kcal/kg	ψ_a kcal/(kg·k)
1000	0.27254	0.4632	2.0814	178.62	252.6	1301.6	431.2	1.90364
1001	0.27258	0.4634	2.0823	178.89	253.0	1303.6	431.9	1.90391
1002	0.27263	0.4637	2.0833	179.16	253.5	1305.7	432.7	1.90418
1003	0.27267	0.4639	2.0842	179.43	254.0	1307.8	433.4	1.90445
1004	0.27272	0.4642	2.0851	179.71	254.4	1309.9	434.1	1.90472

T K	θ_ψ kcal/(kg·k)	δ_ψ kcal/(kg·k)	$\bar{\psi}_a$	$\bar{\theta}_\psi$	$\bar{\Delta}_\psi$	$c_{p,w}$ kcal/(kg·k)	h_w kcal/kg	ψ_w kcal/(kg·k)
1000	0.4223	10.8085	27.7655	5.248	-13.122	0.54645	344.42	3.08375
1001	0.4228	10.8106	27.7695	5.254	-13.116	0.54661	344.97	3.08430
1002	0.4232	10.8127	27.7734	5.261	-13.110	0.54678	345.51	3.08484
1003	0.4237	10.8148	27.7774	5.268	-13.104	0.54695	346.06	3.08539
1004	0.4242	10.8168	27.7813	5.274	-13.098	0.54712	346.60	3.08593

Example: Find the entropy function ψ and dimensionless entropy function $\bar{\psi}$ of complete combustion products of H_2 and air at $\phi = 1.0$ and $T = 1000K$ (for the combustion products, $f_{st} = 0.0291619$, $m_{st} = 24.6458\text{kg/kgmol}$, $C = 0.024160$ and $R/mg = 0.080575\text{kcal/(kg.k)}$).

Solution: From equation (14) we get $a = 1$. Hence

/167

$$\psi = 1.90364 + \frac{0.0291619}{1.0291619}(0.4223 + 10.8085) = 2.22187\text{kcal/(kg.K)}$$

and

$$\bar{\psi} = 27.7655 + 0.024160(5.248 - 13.122) = 27.5753$$

The value of $\bar{\psi}$ can be calculated through ψ

$$\bar{\psi} = \frac{m_s \psi}{R} = \frac{2.22187}{0.080575} = 27.5752$$

We can see that these two calculations are consistent.

References

- [1] Wu Zhonghua, Table of Thermodynamic Properties of Combustion Gases, Science Publishing Co., (1957).
- [2] Fielding, D. and Topps. J.E.C., Thermodynamic Data for the Calculation of Gas Turbine Performance, ARC R & M, No. 3099, (1959).
- [3] Chappell, M.S. and Cockshutt, E.P., Gas Turbine Cycle Calculation, Thermodynamic Data Tables for Air and Combustion Products, National Aeronautical Establishment, Ottawa, Ontario, Jan. (1969), (AD-690716).
- [4] Yang Donghua, Computation and Analysis of Thermodynamic Properties of Combustion Products, Journal of Mechanical Engineering, Vol. 16, No. 4, (1980).
- [5] Fan Zuomin, Enthalpy Table and Its Applications, Defense Industry Publishing Co., Beijing, (1976).

δ FUNCTION AND GENERALIZED TABLES OF THERMODYNAMIC PROPERTIES FOR C_nH_m - AIR SYSTEM COMBUSTION PRODUCTS

Fan Zuomin

(Gas Turbine Research Institute)

Fu Xunquan

(Power Plant Research Laboratory, Beijing Research Institute)

Abstract

A new kind of thermodynamic properties is proposed which is designated by the name of δ function

$$\delta = \theta_2 - \theta_1$$

where θ_1 and θ_2 are θ functions of two reference fuels which can be selected arbitrarily.

The δ function is dependent only on temperature and independent of hydrogen-carbon ratio of the fuel and fuel-air ratio for C_nH_m -air system. With the aid of the δ function a set of generalized tables of thermodynamic properties has been worked out, which can be applied to obtaining the thermodynamic properties of C_nH_m -air system combustion products at any fuel-air ratio easily and exactly. A specimen of the generalized tables is given in this paper.

Multi-rate Digital Flight Control System
Guo Buofeng (Nanjing Institute of Aeronautics)

/178

Abstract

Considering the multi-rate sampling capability of the digital flight control system, the equivalent transformation method and the process to transform into a single-rate system were analyzed. Furthermore, the performance and design method of a multi-rate system were also discussed.

I. Multi-rate Capability of Digital Flight Control System

The feedback circuit of a flight control system usually consists of multiple loops because of different functions such as damping stabilization, attitude maintenance and altitude control. For digital flight control systems, most practical systems employ multi-rate sampling by taking the frequency bandwidth and signal variation rate into consideration. The reasons for using multi-rate sampling are as follows:

1. The computation rate of the computer can be effectively lowered to reduce the work load.
2. The error and phase shift due to digitization can be minimized by choosing a high sampling rate based on the high frequency end of the wide band feedback compensator. The insensitive area and hysteresis of the compensator can be reduced by choosing a low sampling rate corresponding to the low frequency end of the narrow band feedback compensator.

In order to facilitate the realization of multi-rate sampling and computer timing, the ratio of sampling rates is usually an integer, besides using synchronous sampling.

For aircraft control, the pitch rate gyroscope feedback circuit is usually set at 80 Hz. The stick force and normal

acceleration feedback circuit is either at 80 or 40 Hz. The attitude stabilizing feedback circuit is at 20 Hz. The altitude stabilizing feedback circuit is at 10 Hz. The throttle control lever is at 5 Hz. The lateral feedback circuit is set at 40 Hz. In some cases, the pitch rate feedback circuit uses 40 Hz and only the wave trap is at 80 Hz. The rudder feedback circuit is, in most cases, a simulated feedback circuit. In recent years, digital compensators are used as digital rudder feedback circuits. The sampling rate is the highest in the entire system, approximately at above 100 Hz.

It is possible to independently analyze several unrelated feedback circuits at different sampling rates. A multi-rate systems analysis is only required when different sampling rates are used for several feedback circuits, or when different sampling rates are used for different compensators on the same feedback circuit, or when cross-linking exists at various sampling rates.

The analysis and design of a multi-rate sampling system has some special features. If a multi-rate system can be transformed into an equivalent single-rate system, the usual design methods for digital systems can be applied.

There are three equivalent transformation methods:

1. decomposition time domain sample;
2. mixed attitude transformation;
3. decomposition of frequency domain sampling signal.

/179

The 3rd method^[1] is simple. It can be directly described by the Z transfer function, which is easy to process by computer and more appropriate for a digital flight control system.

II. Equivalent Transformation of Multi-rate Digital Control System

As examples, the block diagrams of the digital fly-by-wire control system and the attitude and altitude control system are shown in Figures 1 and 2.

In these figures, $z_1 = e^{sT_1}$, $z_2 = e^{sT_2}$ and $z_4 = e^{sT_4}$. In Figure 1, ZOH_1 is the digital zero order holder and ZOH_2 is the D/A holder. In Figure 2, ZOH_1 and ZOH_2 are the digital holders. ZOH_4 is the D/A holder and pf is the pre-filter.

1. Equivalent Transformation of

In order to convert a multi-rate sampling system into an equivalent single-rate system, it is necessary to convert two different components in the system into a single-rate component.

(1) Low-rate Input-High-Rate Output Component

The equivalent transformation is shown in Figure 3.

When pseudo high rate sampler must be introduced behind the low-rate sampler, then the transfer characteristics of the sampling signal remain unchanged, i.e.,

$$\begin{aligned} R'(z_n) &= R(z_1) \\ C(z_n) &= G(z_n)R'(z_n) = G(z_n)R(z_1) \end{aligned} \quad /180$$

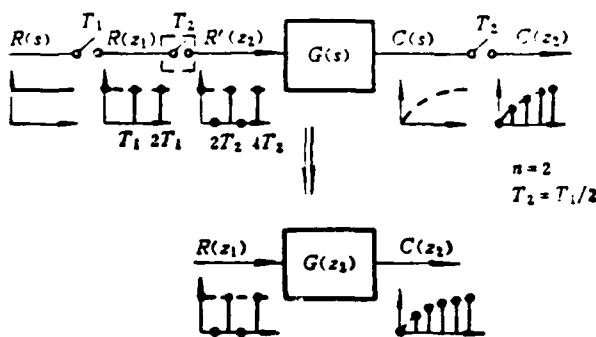


Figure 3. Equivalent transformation of low sampling rate input high rate output component

We can process a low-rate input signal $R(z_1)$ into an equivalent high sampling rate signal $R(z_2)$. The values of this equivalent high sampling rate signal at low sampling periods $0T_1, 1T_1, 2T_1, \dots$ are equal to $R(z_1)$. They are zero at high sampling periods $1T_2, 3T_2, 5T_2, \dots$.

(2) High-rate Input Low-rate Output Component

The equivalent transformation is shown in Figure 4.

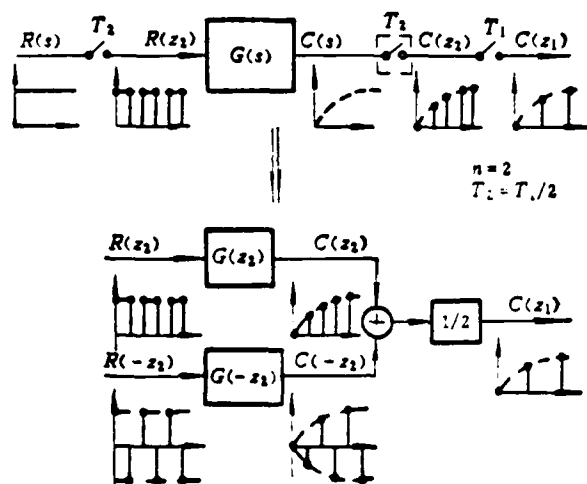


Figure 4. Equivalent transformation of high sampling rate input low rate output component.

A pseudo high-rate sampler is introduced in front of the low-rate sampler.

In order to decompose the sampling signal in the frequency domain, let us assume that

$$C(z_1) = [C(s)]^{*T_1} = \frac{1}{T_1} \sum_{l=-\infty}^{\infty} C\left(s + j \frac{2\pi}{T_1} l\right) = \frac{1}{T_1} \sum_{l=-\infty}^{\infty} C\left(s + j \frac{2\pi}{T_1} nl\right)$$

failure due to instantaneous changes of the power supply and electromagnetic interference. Hence, the redundancy for first failure is significantly delayed. The above principle also applies to computers and rudder servos.

IV. Design of Second Failure Reconfiguration Management

The reconfiguration management for second failures is far more complex than that for first failures. It must be capable of bringing the system safely into a single channel or control law reconfigured state in case of any possible similar second failure state (including detected and undetected). There are two possible basic monitoring methods. First, it is necessary to incorporate self-monitoring to identify and isolate a failed channel because a comparison monitor can only detect, but not identify, a failed channel in case of second failure. Secondly, a control law reconfiguration is used to replace a self-monitor. This means that the failure is detected by a comparison monitor. Then, both channels are isolated (one of the two actually failed). Based on approximation of the output from the operating components, the normal output value of the failed components is estimated and substituted into the new control law. Consequently, the system can still operate when a component is missing (the performance may be downgraded). Apparently, the second plan is only applicable to sensors. Moreover, it takes longer to estimate and reconfigure. It is not necessarily appropriate in all conditions. However, when it is possible, the combination of both methods discussed above is more favorable because it is not only capable of undergoing control law reconfiguration when a second failure is not detected by sensors, but also able to operate in a single channel manner when the sensor or other components failed twice. Consequently, the second failure coverage rate and the safety and reliability of the system can be improved. With regard to the requirement

overcome the side effect of equalization - burying failures, equalization should be appropriately limited. In this work, an integrating component with a feedback mechanism (i.e., an inertia component) was used as the equalizer for the sensor. Furthermore, the median was used as the base for equalization. The principle of equalization is shown on the left side of Figure 1. The time constant of the equalizer should be sufficiently large to obtain an approximate integration. It was selected to be about 6 seconds. The equalization algorithm is shown in Figure 2. The channel input signal (S) is a typical sinusoidal wave (1Hz), the tolerance of the three channels considered as a time dependent biasing error. The maximum absolute tolerance (δ) is ± 0.07 . From the figure, after 0.025 seconds (two computation cycles) of initial equalization, the channel tolerance fell within the absolute tolerance band of ± 0.012 .

In order to avoid comparison monitor errors at first failure /183 (primarily to prevent error in the initial equalization), at least three times the equalized tolerance should be used to monitor a dead zone.

In order to meet the high coverage requirement for monitoring the first failure, both dynamic and static comparison monitors were used. For instance, it is very difficult to identify a slow drift failure with dynamic comparison monitoring. The principle of monitoring is shown on the right half of Figure 1. No matter whether it is a dynamic or static failure, a corresponding temporary failure marker is set up. Furthermore, it is insulated as the failure channel. In the meantime, a timer is started. When the reconfiguration time limit is exceeded, and the failure still exists, then it is determined to be a permanent failure. If the failure disappears before the time limit, then the channel is restored (i.e., removing the isolation). In order to cover more temporary failures, the reconfiguration time limit should be as long as possible, such as 2 seconds. Such reconfigurations can significantly lower the probability of

S-channel input, F_S -self-monitored failure indicator, F_P -permanent failure indicator, F_F -dynamic instantaneous failure indicator, F_C -static instantaneous indicator, V-decision output, e-error signal, e_1 -amplitude limiting error, E-channel tolerance, E_1 -amplitude limiting channel tolerance, E_S -channel input after equalization

1. dynamic comparison monitoring and reconfiguration logic
2. static comparison monitoring and reconfiguration logic

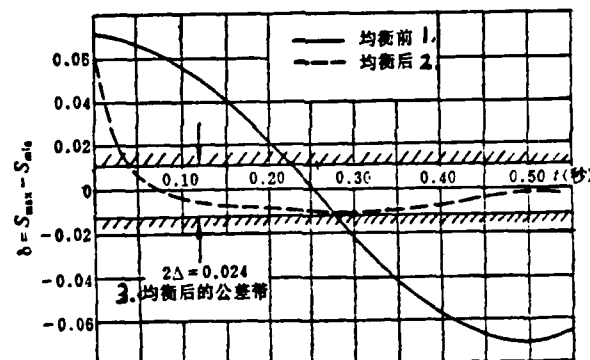


Figure 2. Demonstrated result for equalization algorithm

- Key:
1. before equalization
 2. after equalization
 3. tolerance band after equalization

Equalization of redundancy channels is usually required for sensors and rudder control servo, there are two purposes for equalization. The first one is to prevent the uncontrollability (divergence) of certain intermediate components (variables) in the redundancy system due to channel tolerance, especially integrating components. The second one is to accomplish comparison monitoring with high coverage rates. In order to

The reconfiguration management after any failure consists of two fundamental aspects: monitoring failures and treating failures (reconfiguration and isolation). As for monitoring failures, there are two main strategies to choose from. One is to use a simple comparison monitor, and the other is a combination of comparison monitoring and self-monitoring. The former has a relatively lower coverage rate, but the computation time is shorter. The latter takes longer time to calculate, but its coverage rate is higher. In this work, only the latter was considered. The reconfiguration of first failure is primarily aimed at the identification of instantaneous and permanent failures and the restoration of the system to the same redundancy after an instantaneous failure.

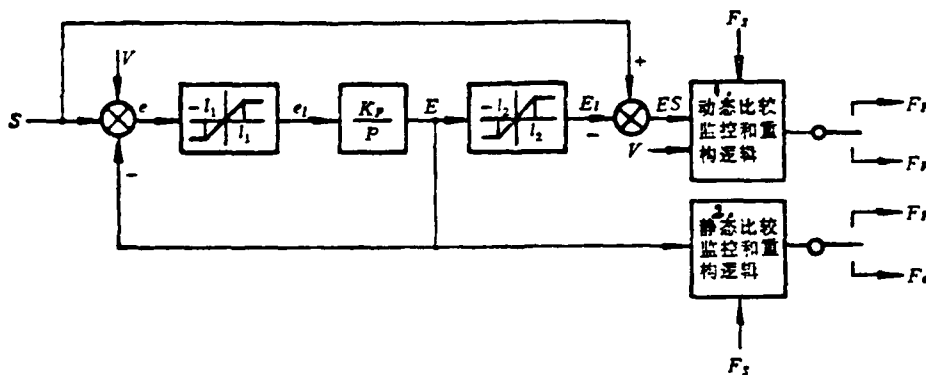


Figure 1. Equalization and comparison monitor for sensors

Analog calculation and real-time verification showed that this reconfigurable management plan is feasible and not difficult to realize.

II. Design Requirements

In this study, the DFBW is a triple redundancy system which remains operational after a second failure. Each component was able to monitor itself or to be monitored on-line. The computer itself, however, has quadruple redundancy (triple redundancy with a spare channel for heat) to ensure the performance of this core component. Major design requirements for this reconfigurable management system are as follows:

Prior to the first permanent failure takes shape, it should have the capability to restore its performance instantaneously with a probability of restoration not less than 0.97.

Comparison monitoring is the primary method to monitor failures. It is aided with self-monitoring. In combination, the coverage for a first permanent failure should not be less than 0.97.

Self-monitoring and control law reconfiguration are combined in such a way so that the coverage for second failure is not less than 0.90.

After a second failure is spotted and the control law reconfiguration takes effect, the probability of success for third failure-safety is primarily determined by the comparison monitor coverage rate of the computer, which should not be less than 0.97.

The time required to run the entire reconfigurable redundancy management system should not exceed 50% of the total computation cycle.

Reconfigurable Redundancy Management Strategy for a * /186
Triplex DFBW System

Li Lichun

(Institute of Automatic Flight Control System)

Abstract

A reconfigurable redundancy management strategy, including the suitable indicators proposed for the redundancy management system, the design principle of redundancy and control law reconfiguration after failures and experimental verifications, was discussed. In addition, the reconfigurable management software and the feasibility for real time operation were also described.

I. Introduction

The reliability of digital fly-by-wire flight control system (DFBW system for short) is, to a great extent, dependent on the redundancy management design. Among various management strategies, the reconfiguration management method has already demonstrated its superiority^[1,2]. Conceptually, reconfiguration management has a "specific" and a "generalized" sense. A specific reconfiguration is limited to the redundant restoration of the system after one instant failure. A generalized reconfiguration, however, has already extended to the reconfiguration of redundancy and control structures after multiple failures (including instantaneous and permanent failures). In this paper, a generalized reconfiguration management strategy for a DFBW system with triple redundancy was introduced. The purpose was to fully utilize the capability of a computer to satisfy the high reliability requirement of operating with double failure with relatively uncomplicated hardware.

*received in July, 1983

MULTI-RATE DIGITAL FLIGHT CONTROL SYSTEMS

Guo Suofeng

(Nanjing Aeronautical Institute)

Abstract

Considering the multi-rate sampling feature of digital flight control systems, the approach of equivalent transformation and its transformation into an equivalent single-rate system are analyzed.

The method of decomposition of sampling signal in frequency domain may be utilized in this equivalent transformation. To simplify the implementation and timing on computer, the ratio of sampling rate n is often considered as an integer. Thus, the equivalent single-rate system may be represented by Z transfer function with several parallel paths. If the integer n is such a small number as 2, 4, the computation is not very complicated.

The behavior of multi-rate system is discussed. It may be illustrated by a simple system. As a high sampling rate has been introduced to one part of the system, the open-loop poles and its steady-state gain of the resulted system are not varied, only a zero is added in the real axis of the Z -plane. It implies that the margin of stability is increased, the overshoot of step response and D/A output ripple may be decreased. The unequal sampling rates can be adopted to improve system performance.

Finally, the approaches to design multi-rate digital flight control system are described in brief.

References

- [1] John F. L. Lee, A.F. Konar, Analysis of Multi-loop Multi-rate Digital Flight Control Systems, AIAA 76-1972.
- [2] Xie Kexing, Analysis and Constitution of a Digital Attitude Control System, Journal of Astronautics, (1980), 6.

flight control systems.

The design of a multi-rate digital flight control system is far more complicated than that of a single-rate system.

Digitized design is carried out on the basis of a continuous system because of our trust on the guidelines of or the design of a continuous system and our experience in design over the years. This method is based in the concept that the frequency response is approximately unchanged. It is generally required that the difference between the open loop frequency response and the digital response is $\Delta A \leq 1$ db, $\Delta \phi \leq 5^\circ$ at the cutoff frequency. A Tustin transformation can result in more satisfactory results. The shortcomings are that the phase shift caused by the pre-filter and the holder must be compensated, the performance cannot be checked directly and the design cannot be changed easily.

The W' -plane design method may be used as a design tool in the frequency domain. More direct performance verification and design changes can be made. The steady state $G(W')$ and that of $G(s)$ are equal. The zero poles are very close. The extent of closeness is determined by the sampling rate and zero poles. Furthermore, the effect of the pre-filter and the holder can be directly shown. By choosing the appropriate sampling rate, it is possible to make the zero pole in the s -domain equal to that in the W' -domain. By making the proper correction, the few high frequency zero poles can be directly transformed into the zero poles in the W' -domain. The computation process can then be significantly simplified^[2]. The $D(W') \rightarrow D(z)$ process for the designed controller is similar to the Tustin transformation using a specially designed digitized continuous controller.

By combining these two design methods with the equivalent transformation of the multi-rate system, it is possible to design digital multi-rate systems. The specific procedures are omitted.

Comparing the open loop transfer function of a multi-rate system with that of a single-rate system, one can see that:

- (1) the poles remain unchanged;
- (2) the steady-state gain after taking integration into account remains unchanged; and
- (3) a zero point is added on the Z_1 plane in the multi-rate system which is equivalent to introducing a compensation in advance.

If we let $K = 0.5$ and $T = 1$, the input is a unit step, then the output of the system is as shown in Figure 8.

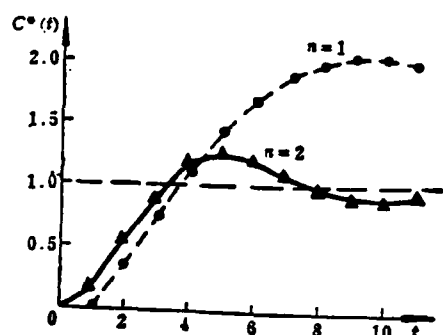


Figure 8. Unit-step response of simple system

From this figure one can see that the stability of the system increases, the overshoot decreases, the rise time becomes faster and the quality is improved as high-rate sampling is locally introduced into the system. In addition, the D/A output ripple may also be decreased.

We analyzed situations under which there are multiple parallel channels ($n=4$) and there are complex poles in addition to real poles in the loop, and discovered that the three rules mentioned above are still valid. This indicates that this simple example is somewhat general. It is also applicable to digital

From Figures 5 and 6 one can see that there are two and four parallel channels, respectively. The complexity of the equivalent systems is determined by the magnitude of n .

A~B are ancillary channels and point A is the low sampling rate signal. Because $E(z_1) = E(z_2^2) = E[(-z_2)^2]$, the ancillary channel begins with the sampling rate signal.

III. Performance Analysis and Design of Multi-rate System

A simple example is used to illustrate this point, as shown in Figure 7.

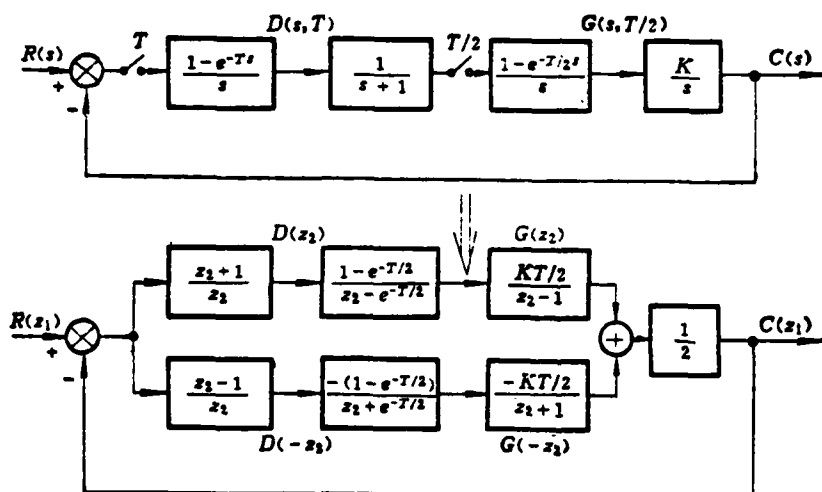


Figure 7. Block diagram of equivalent transformation of one simple system

The open loop transfer function of the system is:

$$\begin{aligned} W(z_1)|_{n=2} &= \frac{1}{2} \left[\frac{KT/2(1-e^{-T/2})(z_1+1)}{z_1(z_1-1)(z_1-e^{-T/2})} + \frac{KT/2(1-e^{-T/2})(z_1-1)}{z_1(z_1+1)(z_1+e^{-T/2})} \right] \\ &= \frac{KT/2(1-e^{-T/2})(z_1^2+1+2e^{-T/2})}{(z_1^2-1)(z_1^2-e^{-T})} \\ &= \frac{KT/2(1-e^{-T/2})(z_1+1+2e^{-T/2})}{(z_1-1)(z_1-e^{-T})} \end{aligned}$$

When the entire sampling cycle is T ,

$$W(z_1)|_{n=1} = \frac{KT(1-e^{-T})}{(z_1-1)(z_1-e^{-T})}$$

/184

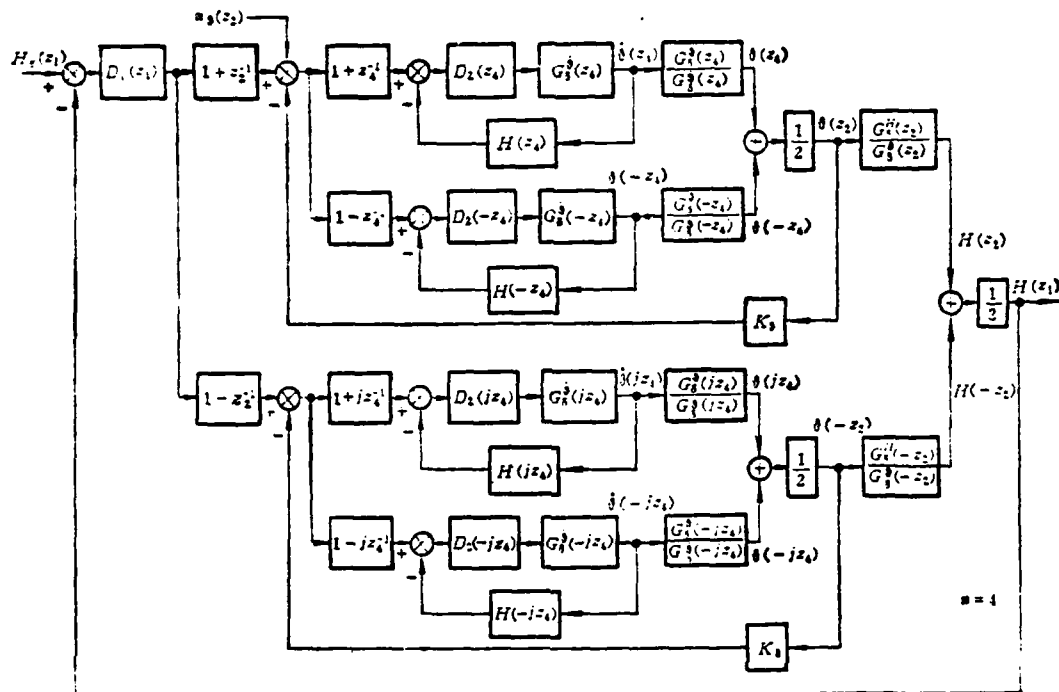


Figure 6. Block diagram of equivalent transformation of multi-rate digital attitude and altitude control system

/183

$$C(z_n) = \frac{1 - z_1^{-1}}{1 - z_n^{-1}} R(z_1) = \frac{1 - z_n^{-n}}{1 - z_n^{-1}} R(z_1) = [1 + z_n^{-1} + z_n^{-2} + \dots + z_n^{-(n-1)}] R(z_1)$$

$$C(z_2) = (1 + z_2^{-1}) R(z_1)$$

If $n=2$,

$$C(z_4) = (1 + z_4^{-1} + z_4^{-2} + z_4^{-3}) R(z_1)$$

$n=4$,

The digital holder will introduce a similar phase shift.

(2) Formation of Ancillary Channel in the System

When a system undergoes an equivalent transformation, the ancillary component must extend forward to the low-rate input high-rate output component, including the digital holder, to form an ancillary channel.

The multi-rate digital in-by-wire and auto-pilot loops shown in Figures 1 and 2 are undergoing equivalent transformation. Their structures are shown in Figures 5 and 6.

The transformation of this component is accomplished by an ancillary component $G(-z_2)$ in the high-rate signal channel. Its input signal $R(-z_2)$ and output signal $C(-z_2)$ are equal in amplitude as those of the input signal $R(z_2)$ and output signal $C(z_2)$ of the component $G(z_2)$. The sign alternates with the sampling point. The sampling value of the middle point will cancel out by adding the two values and dividing it by two to obtain the low sampling rate signal.

2. Equivalent Transformation of the System

When low sampling rate and high sampling rate signals are combined in the equivalent transformation of a system, a digital holder is brought into the low-rate signal. It is then combined with the high sampling rate signal at the same rate. In addition, a digital holder is required to link sampling signals at various rates.

(1) Equivalent Transformation with Digital Holder

/182

Because $C(z_n) = G(z_n) R(z_1)$ we get

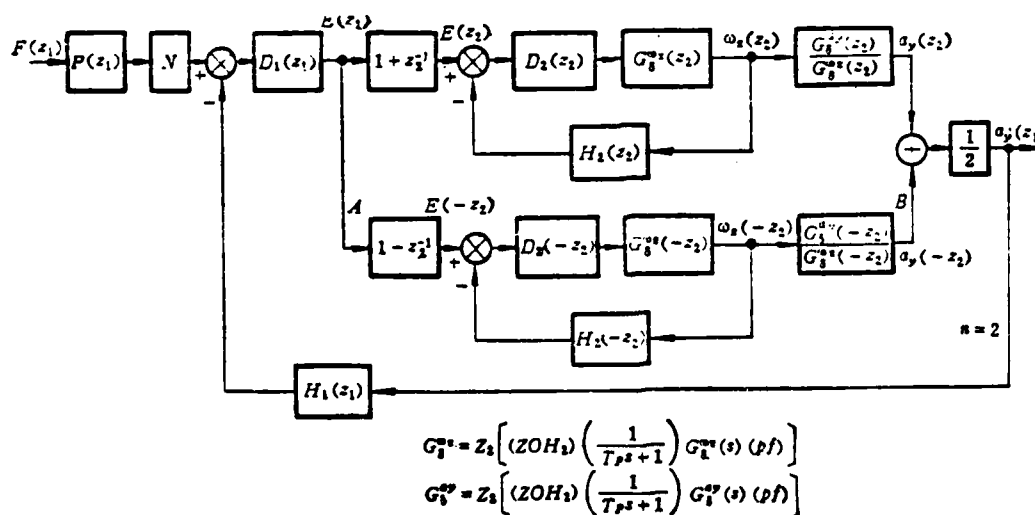


Figure 5. Block diagram of equivalent transformation of multi rate digital fly-by-wire control system

$$C(z_1) = [C(s)]^{*T_1} = \frac{1}{T_1} \sum_{m=-\infty}^{\infty} C\left(s + \frac{2\pi}{T_1} m\right)$$

In order to find the relation between $C(z_1)$ and $C(z_n)$, we let $m = k + nl$ in the above equation. Then,

$$\begin{aligned} C(z_1) &= \frac{1}{T_1} \sum_{k=0}^{n-1} \sum_{l=-\infty}^{\infty} C\left(s + j \frac{2\pi}{T_1} k + j \frac{2\pi}{T_1} nl\right) \\ &= \frac{1}{n} \sum_{k=0}^{n-1} \left[\frac{1}{T_n} \sum_{l=-\infty}^{\infty} C\left(s + j \frac{2\pi}{T_1} k + j \frac{2\pi}{T_n} l\right) \right] \\ &= \frac{1}{n} \sum_{k=0}^{n-1} \left[C\left(s + j \frac{2\pi}{T_1} k\right) \right]^{*T_n} \end{aligned}$$

According to the complex displacement theory of Z transformation, we get

$$C(z_1) = \frac{1}{n} \sum_{k=0}^{n-1} C\left(e^{j \frac{2\pi}{n} k} z_n\right) = \frac{1}{n} \sum_{k=0}^{n-1} C(a_k z_n)$$

From Figure 4,

$$C(z_n) = G(z_n) R(z_n)$$

$$C(a_k z_n) = G(a_k z_n) R(a_k z_n)$$

or

Therefore,

$$C(z_1) = \frac{1}{n} \sum_{k=0}^{n-1} G(a_k z_n) R(a_k z_n)$$

where $a_k = e^{j \frac{2\pi}{n} k}$, $k = 0, 1, 2, \dots$, which is a unit vector whose argument is equal to $\frac{2\pi}{n} K$; a complex number.

If $n = 2$, $a_k = [1 \ -1]$, then

$$C(z_1) = \frac{1}{2} [G(z_2) R(z_2) + G(-z_2) R(-z_2)]$$

If $n = 4$, $a_k = [1, j, -1, -j]$

$$\begin{aligned} C(z_1) &= \frac{1}{2} \left\{ \frac{1}{2} [G(z_4) R(z_4) + G(-z_4) R(-z_4)] + \frac{1}{2} [G(jz_4) R(jz_4) \right. \\ &\quad \left. + G(-jz_4) R(-jz_4)] \right\} \end{aligned}$$

In simple cases ($n=2$), the equivalent transformation of a high-rate input output component demonstrates an obvious concept, as shown in Figure 4.

that the velocity gyroscope should never fail for an aircraft with relaxed static stability, controlled reconfiguration is a feasible scheme. From any two measured values of rudder deflection angle, attack angle and pitch rate, it is possible to estimate the third variable according to a linear short period motion (reconfiguration does not require a very accurate estimation).

Table 1. Reconfigurable strategy for 2nd failures

故障 组合	1. 一次故障		5 二次故障		8 重 构 策 略
	3. 性质	4. 监 控 条 件	6. 性质	7. 监 控 条 件	
1	T	(1 - α)	T	(1 - α)	14 立即将故障标升级为永久故障
2	P	(1 - α), (1 - β), 9. 或 (1 - α), β , 10. 或 α , (1 - β)	P	(1 - α), (1 - β)	15 余度降级为单通道工作
3	P	11. 同组合 2	P	α , (1 - β)	16 余度降级为单通道工作
4	P	12. 同组合 2	P	(1 - α), β	17 控制律重构
5	P	13. 同组合 2	P	α , β	18 转备份系统工作
6	P	α , β	P	α , (1 - β)	19 余度降级为单通道工作
7	P	α , β	P	(1 - α), β	20 转备份系统工作

21. 注: T—瞬时性故障; P—永久性故障; (1 - α)—比较监控冗余; α —比较监控漏检; (1 - β)—自监控冗余; β —自监控漏检。

Key:

1. failure combination
2. first failure
3. nature
4. monitoring and control condition
5. second failure
6. nature
7. monitoring and control condition
8. reconfiguration strategy
9. or
10. or
11. same as combination 2
12. same as combination 2
13. same as combination 2
14. immediately elevate failure to permanent failure
15. reduce tolerance to single channel operation
16. reduce tolerance to single channel operation
17. reconfiguration
18. switch to back-up system
19. reduce tolerance to single channel operation
20. switch to back-up system

21. Remark: T-temporary failure; P-permanent failure; (1- α)-comparative monitor coverage; α -comparative monitor missing rate; (1- β)-self-monitor coverage; β -self-monitor missing rate

Theoretically, this is not difficult to do. However, it requires 189 verification and calibration in in-flight experiments. Various second failure combinations and corresponding reconfiguration strategies are listed in Table 1.

Different reconfiguration measures are taken for various types of sensor failures according to the extent of effect on safety. Table 2 shows some typical plans for reconfiguration (using longitudinal system as an example). Figures 3 and 4 show the digital analog result of the step lever control of a fighter at $H=12\text{Km}$ and $M=1.0$, when the speed gyroscope in the DFBW system failed twice consecutively. The failure in Figure 3 corresponds to combination 2 in Table 1 (no miss by the monitors). It is capable of switching to single channel operation. The failure in Figure 4 corresponds to combination 4 in Table 4 (a second failure not detected). It represents reconfiguration when the sensor breaks down. From the two figures one can see that both failures did not create any noticeable effect on the flight quality and maneuverability.

Table 2. Reconfiguration for various sensors

1. 传 感 器	7. 重 构 措 施
2. 俯仰速率	8 用估算值 $\hat{\omega}_z$ 代替传感器输出
3 法向加速度	9 令 $N_y = 0$, 并改变其它反馈的传动比
4. 迎 角	10 令 $\alpha = 0$, 并改变其它反馈的传动比, 或用估算值 $\hat{\alpha}$ 代替传感器输出
5. 杆 力	11 令 $F_P = 0$, 转备份系统工作
6. 动压和静压	12 用固定增益代替大气数据测参

Key:

1. sensor
2. pitch rate
3. normal direction acceleration
4. attack angle
5. lever force
6. dynamic and static pressure
7. reconfiguration procedure
8. use estimated ω_z to replace sensor output
9. let $N_y=0$ and change the transmission ratio of other feedback
10. let $\alpha=0$ and change other feedback transmission ratio or use estimated $\hat{\alpha}$ value to replace sensor output
11. let $F_p=0$ and switch to standby unit
12. use constant gain to replace atmospheric data

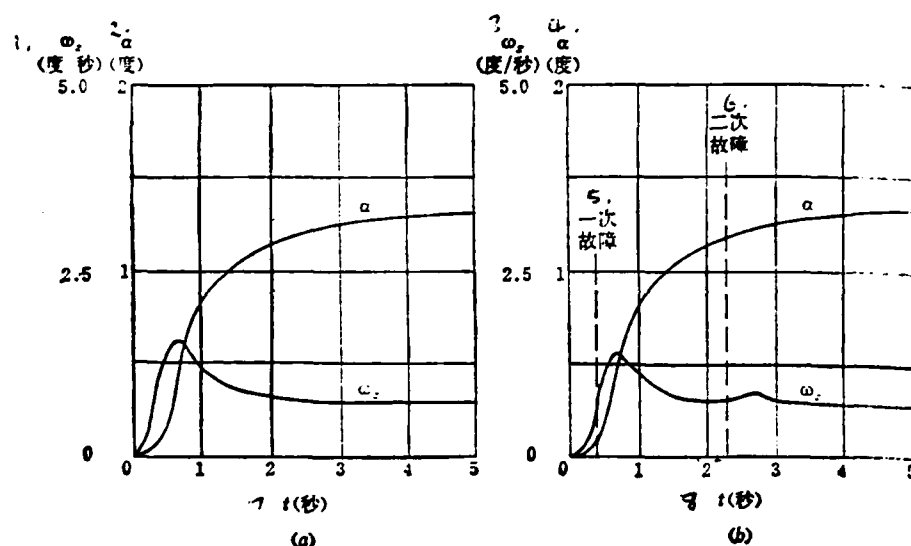


图3 二次重构数字仿真结果 (故障组合2)

(a) 无故障; (b) 二次故障。

Figure 3. Digital analog result for 2-nd reconfiguration (failure combinations No.2)

Key:

1. (degree/sec)
2. (degree)
3. (degree/sec)
4. (degree)
5. first failure
6. second failure
7. (sec)
8. (sec)
9. no failure
10. second failure

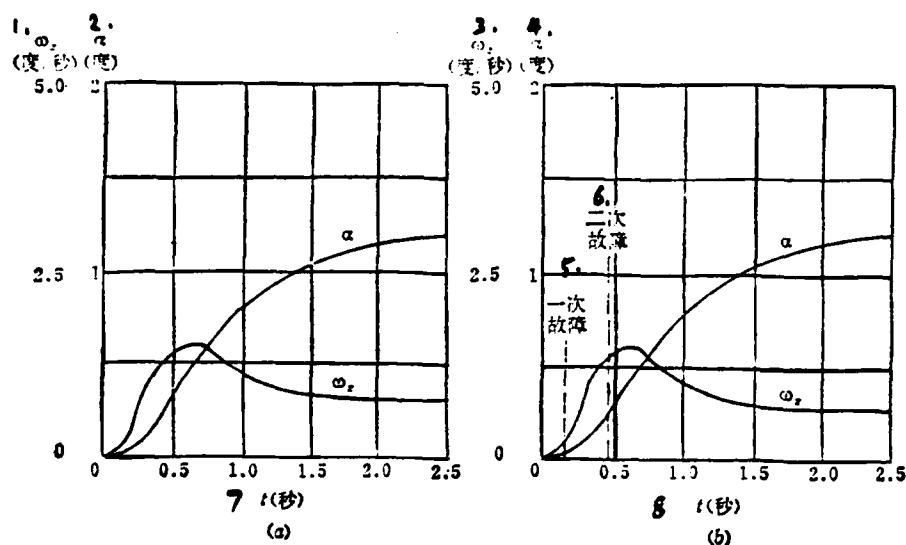


图4 二次重构数字仿真结果 (故障组合4)

9. (a) 无故障; (b) 二次故障。

Figure 4. Digital analog result for 2-nd reconfiguration (failure combinations No.4)

- Key:
1. (degree/sec)
 2. (degree)
 3. (degree/sec)
 4. (degree)
 5. first failure
 6. second failure
 7. (sec)
 8. (sec)
 9. no failure
 10. second failure

V. Triplex Reconfiguration Design

When the redundancy of the system is reduced to single channel operation, only self-monitoring can be used to detect a third failure. Hence, the only situations after a failure are coverage and miss. For a sensor, when a third failure is detected, it is safely switched to a reconfiguration. Moreover, it only reports the failure but not cut off the DFBW system.

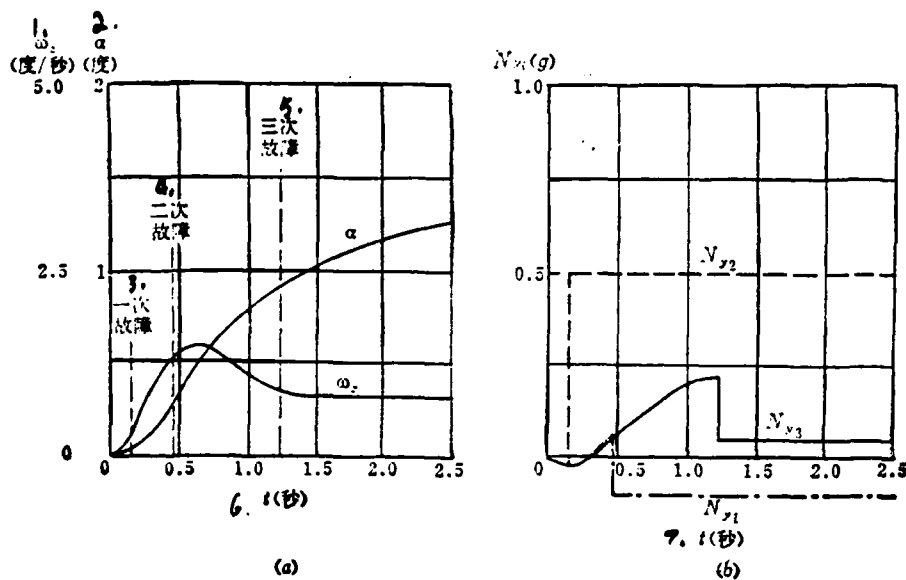


图5 三次重构数字仿真结果
8. (a) 飞机运动响应; (b) 传感器故障特征。

Figure 5. Digital analog result for 3rd reconfiguration

- Key:
1. (degree/sec)
 2. (degree)
 3. first failure
 4. second failure
 5. third failure
 6. (sec)
 7. (sec)
 8. aircraft flight response
 9. sensor failure characteristics

This spares the pilot from switching to the standby system in a /191 hurry. It is very important for an aircraft with relaxed static stability. When a third failure is not detected, then we must depend on human judgement and switch to the standby system for emergency. However, it is highly improbable. Figure 5 shows the flight response and sensor output (N_{y1}) failure characteristics when the third failure of the normal direction acceleration meter is detected and the system is switched into reconfiguration under the same conditions as those in Figures 3 and 4. All third failures did not cause any noticeable change in the motion. Compared to no failure (Figure 4(a)), there is no difference in

the control quality of the flight.

VI. Design and Execution of Reconfiguration Software

Redundancy reconfigurations and controlled reconfigurations mentioned above are materialized by software. However, the signal source comes from the hardware. The structure of the reconfiguration management software, using a sensor as an example, is shown in Figure 6. In addition to the collection of input signals, there are seven modules. The core of the software is the "reconfiguration and isolation" module. It executes the reconfiguration management logic after failures and controls the "signal voting" module by using the "isolation marker (I)" to complete the isolation of the failed channels.

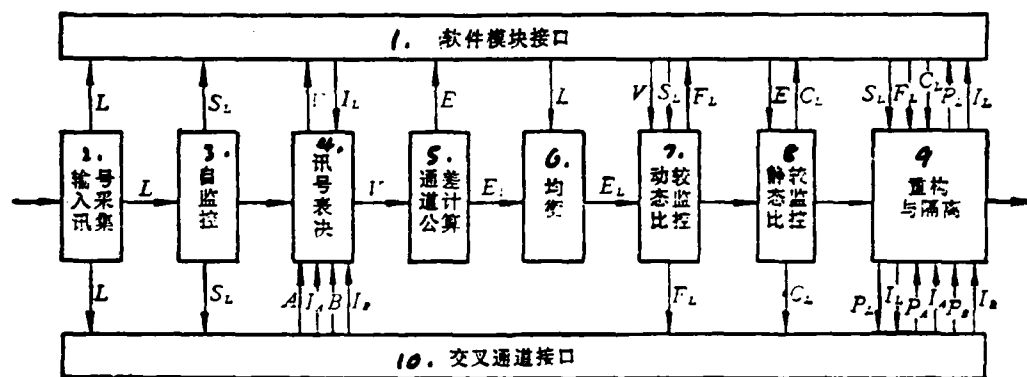


图6 传感器重构管理软件的模块结构

11. L, A, B —传感器本地、左和右通道输入; S_L, F_L, C_L, P_L —本地通道的自监控、动态瞬时、静态瞬时和永久性故障标; I_L, I_A, I_B —本地、左和右通道的故障隔离标。

Figure 6. Functional diagram for sensor reconfigurable management software modules

Key:

1. software module interface
2. collecting input signal
3. self-monitoring
4. signal voting
5. calculating channel variance
6. balancing
7. dynamic comparative monitoring
8. static comparative monitoring
9. reconfiguration and isolation

10. cross channel interface
11. L, A, B-sensor input from channels on the spot and from the left and right; S_L , F_L , C_L , P_L -self monitoring, dynamic temporary, static temporary and permanent failure markers, respectively; I_L , I_A , I_B -failure isolation markers for local, left and right channels.

The primary factor determining the software execution time is data transmission, especially the cross channel data transmission time. For a typical microcomputer processing the reconfiguration management of six sensors, there are six sets of data to be cross transmitted by each sensor. Each data cross-transmission time is under 50 microseconds. Then, the total execution time of all the sensors is about 4.2 milliseconds. It is approximately 33.6% of the total time (12.5 milliseconds in this example). When we consider the redundancy management of other components, the redundancy management time will be about 50% of the total computer time in the longitudinal DFBW system.

VII. Conclusions

1. The use of redundancy reconfiguration management strategy in a DFBW system is a natural consequence of utilizing the potential of a computer. It has advantages in improving the reliability of the system, delaying the downgrading of redundancy and reducing wrong switching probability.

2. The reconfiguration strategy introduced in this paper is capable of expanding the scope and function of the reconfiguration because it combines two monitoring modes. Furthermore, it also increases the monitoring coverage. It is /192 more superior over other reconfiguration strategies using comparative monitoring mode.

3. The key to the realization of reconfiguration management is the data transmission time of the computer. Through software design and tailoring, current computers can be used to

materialize it. However, we must increase the data transmission rate as we increase the computation time on the development of future flight control computers.

References

- [1] AIAA 77-1479, P. Ray, ont, et al, The Flight Control Computer of the F-18 Electronics Set-Flight Control, (1977).
- [2] AIAA 81-1707, A. F. Berfied et al, AFTI/F-16 Advanced Control System Design for Task-Tailored Operation, (1981).

A RECONFIGURABLE REDUNDANCY MANAGEMENT STRATEGY FOR A TRIPLEX DFBW SYSTEM

Li Lichun

(Institute of Automatic Flight Control System)

Abstract

A reconfigurable redundancy management strategy for a triplex DFBW flight control system is discussed in this paper. The strategy consists of redundancy and control law reconfiguration after 1st, 2nd and 3rd failures. Every part of the system uses both the comparison monitored and the self-tested schemes. With the combination of two monitors schemes the functional range of reconfigurable strategy can be expanded, and high system reliability can be achieved. The computer verification results for reconfigurable strategy are presented. The reconfigurable management software has been designed, and the architectures for all of software moduls and its interfaces are introduced. It has been shown that the key factor impact on feasibility of the strategy is the data transmitted rate, especially the across-channel data transmitted rate.

An Equivalent Strength Method for Optimum Design of*

Composite Laminates

Liu Fanglong, Huang Jixi

(Beijing Institute of Aeronautics and Astronautics)

Abstract

An equivalent strength method for optimum design of composite laminated plates subjected to an in-plane arbitrary loading is presented as an intuitive and simple engineering method. The method affirms that the design of composite laminates is optimum when the strength ratios of each lamina are equivalent and equal to one. This is a criterion. It can be considered that the orientations of individual ply groups are determined, but the thickness of each group can be adjusted in accordance with the principle of the equivalent strength ratio, in result that the failure of statical tension, compression or shear in each ply of laminate under the designed loads happens at the same time. In design optimization by the equivalent strength method the thickness and the weight of a laminated plate are minimized.

Five numerical examples are given and compared with corresponding data in references [1] and [2]. The results show that the equivalent strength method is better than the methods employed in references [1] and [2].

I. Introduction

The laminated plate, which is one of the main elements of the thin aerofoil structure of the aircraft and spacecraft, is mainly subjected to in-plane static tension, compression and shear under general loads. Presently, symmetric laminates are still widely used due to limitations on the industrial manufacture technology. In order to maintain the continuity of the fibers of each ply of laminate during manufacture, the

*Received in November 1982

orientation of each ply (or group) of laminates should be confined. Experience indicates that the common $\pi/4$ laminated plates, i.e., $[0_i/90_j/45_k/-45_l]_s$ laminates have a reasonable design. This type of laminate is discussed in this paper. The optimum design of a composite structure can be simplified to be the optimum design of a series of symmetrically laminated plates and bars under given load with planar forces having zero moment. The optimum design of the laminates can be considered to be the one which gives minimum thickness and weight for each ply (group) of the laminates with fixed orientation.

Reference [1] uses the equivalent strain energy ratio as the criterion for optimization. With the equations for design iterations, each design iteration is modified regarding the feasibility using the Tsai-Hill strength theory as control condition. This method requires recalculation of the strain energy ratio of each ply (group) as well as the strength criterion of the laminates for each design iteration and is quite complicated. Since the design points usually are outside the strength boundary of the feasible region, it gives excess strength and the design is not an optimum. References [2,3] consider that the optimum design condition for the laminate is one which gives zero excess. The problem of finding the minimum weight under constrained conditions is transformed to an unconstrained problem of determining the extreme values using the method of Lagrange multipliers. The strength criterion for the laminated plate is established experimentally similar to the strength criterion for the uni-directional plates. The limiting strength of the laminated plate along one axis is obtained from the limiting strength of each differently oriented ply (or group) of the laminate along the same axis using the method of linear weighted means with the assumption that the limiting shear strengths along the opposite directions are equal. This method contains certain errors and is limited in applications.

We have proposed an equivalent strength method as a criterion of the optimum design for symmetrically laminated plates. The optimum design is obtained when the strength ratios of each ply (group) of the laminates are equivalent and equal to 1. Figure 1 shows the schema of the optimization. We have applied Tsai-Wu's tensor strength theory with "quasi-network principle" to determine the initial design. According to the characteristics of the laminated plate under stress, design revisions and adjustments are carried out based on the strength ratio of each ply (group).

Analyses and calculation examples indicate that our method is simpler, easier to be visualized, better in engineering and easier in design compared with other methods. It can be widely used by various technical professionals. The formulas are simple and less calculations are involved.

More complicated strength criteria having large number of variables can also be used in this method.

/201

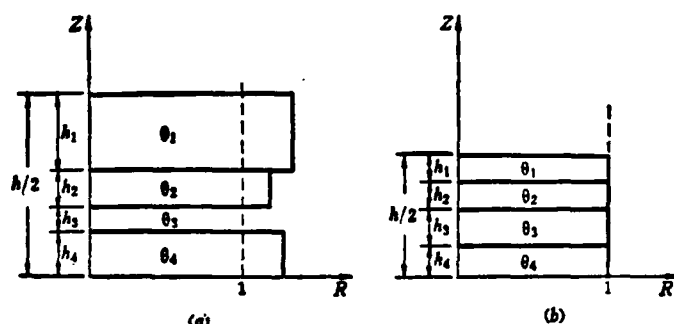


图1 层板等强最优设计示意图
(a) 层板优化前; (b) 层板优化后。

Figure 1. Schematic of optimization in equivalent strength laminate design

(a) Before optimization (b) After optimization

Numerical analyses have been carried out with the same examples given in references [1] and [2]. The results have indicated that our method is more reliable and effective than those in references [1,2].

II. The Basic Principle of Optimization in Laminate Design by Equivalent Strength

In order to compare the result of our calculation with that of reference [1], the influences of temperature and humidity are not included in the optimization calculation. With a laminated plate under compression, we consider only the strength criterion which satisfies the compression. The condition of bending is not included.

1. The stress analysis and the characteristics of the optimum design of the symmetrically laminated plate.

The basic equation for a zero moment, symmetrically laminated plate is^[4,5]

$$\begin{Bmatrix} N_1^* \\ N_2^* \\ N_3^* \end{Bmatrix} = \begin{bmatrix} A_{11}^* & A_{12}^* & A_{13}^* \\ A_{12}^* & A_{22}^* & A_{23}^* \\ A_{13}^* & A_{23}^* & A_{33}^* \end{bmatrix} \begin{Bmatrix} \varepsilon_1^0 \\ \varepsilon_2^0 \\ \varepsilon_3^0 \end{Bmatrix} \quad (1)$$

where $[A^*]$ is the normalized matrix of the in-plane stiffnesses of the laminates,

$$[A^*] = \begin{bmatrix} A_{11}^* & A_{12}^* & A_{13}^* \\ A_{12}^* & A_{22}^* & A_{23}^* \\ A_{13}^* & A_{23}^* & A_{33}^* \end{bmatrix} = 2 \sum_{k=1}^m \begin{bmatrix} Q_{11} & Q_{12} & Q_{13} \\ Q_{12} & Q_{22} & Q_{23} \\ Q_{13} & Q_{23} & Q_{33} \end{bmatrix}_{(k)} V_k \quad (2)$$

where $N_i^* = N_i/h$ — components of the normalized in-plane forces on the laminate

N_i — components of the in-plane forces on the laminate

$V_k = h_k/h$ — volume ratios of the ply groups

h_k — thickness of the ply group

h — thickness of each ply of the laminate

- ϵ_i^0 strain components within the laminate
 Q_{ij} off-axis stiffness components of the plies (groups)
 m number of groups of uni-directional plies within half thickness of the laminate

Subscripts $i = 1, 2, 6$; $j = 1, 2, 6$; $k = 1, 2, 3, 4$, represent the components along the x, y and the tangential coordinates and the group numbers respectively.

The normal strains $\{\epsilon\}_k$ of each ply (or groups) are given by /202

$$\{\epsilon\}_k = [T_e]_k [A^*]^{-1} \{N^*\} \quad (3)$$

where $[T_e]_k$ is the conversion matrix of the strains of each ply (group)

$$[T_e]_k = \begin{bmatrix} m^2 & n^2 & mn \\ n^2 & m^2 & -mn \\ -2mn & 2mn & m^2 - n^2 \end{bmatrix}_k \quad (4)$$

where $m = \cos \theta_k$; $n = \sin \theta_k$.

The normal stresses $\{\sigma\}_k$ in each ply (group) are

$$\{\sigma\}_k = [Q][T_e]_k \{\epsilon^0\} \quad (5)$$

i.e.,

$$\{\sigma\}_k = [\bar{Q}]_k \{\epsilon^0\} \quad (6)$$

where $[\bar{Q}]_k = [Q][T_e]_k$ — the stress matrix, and

$$[\bar{Q}]_k = \begin{bmatrix} Q_{xx} & Q_{xy} & 0 \\ Q_{xy} & Q_{yy} & 0 \\ 0 & 0 & Q_{zz} \end{bmatrix} \begin{bmatrix} m^2 & n^2 & mn \\ n^2 & m^2 & -mn \\ -2mn & 2mn & m^2 - n^2 \end{bmatrix}_k \quad (7)$$

The governing structure equation of the symmetrically laminated plate indicates that the normalized in-plane stiffnesses $[A^*]$ are directly affected by the changes of the design variables h_k . Due to the interactions between plies (or groups), several iterations should be carried out for design

modification. Since the matrix of the normalized in-plane stiffnesses of the laminated plate has a linear relation with the design variables and the stress matrix is irrelative with the design variables, feasibility adjustments can be carried out using the ray-steps method^[6].

2. Selection of the Strength Criterion for the Composite Materials

The Tsai-Hill's theory has been currently used in most publications of design optimization as a strength criterion for the uni-directional plates since it is simple in mathematical treatment. However, since this theory has not considered the difference between the tension strength and the compression strength, it gives rather poor fitness between the theoretical values and the experimental results under certain conditions (such as compression). We have employed the rather complicated Tsai-Wu's tensor theory as the strength criterion for unidirectional plates, which can provide better fitness between the theoretical values and the experimental results. The expression in the strain space is given as

$$\{\varepsilon\}^T \{\tilde{G}\} + \{\varepsilon\}^T \{\tilde{\tilde{G}}\} \{\varepsilon\} = 1 \quad (8)$$

where

$$\{\varepsilon\} = \begin{Bmatrix} \varepsilon_x \\ \varepsilon_y \\ \varepsilon_z \end{Bmatrix}, \quad \{\tilde{G}\} = \begin{Bmatrix} G_x \\ G_y \\ 0 \end{Bmatrix}, \quad \{\tilde{\tilde{G}}\} = \begin{bmatrix} G_{xx} & G_{xy} & 0 \\ G_{xy} & G_{yy} & 0 \\ 0 & 0 & G_{zz} \end{bmatrix} \quad (9)$$

$$\left. \begin{aligned} G_x &= \left(\frac{X' - X}{XX'} \right) Q_{xx} + \left(\frac{Y' - Y}{YY'} \right) Q_{yy} \\ G_y &= \left(\frac{X' - X}{XX'} \right) Q_{xy} + \left(\frac{Y' - Y}{YY'} \right) Q_{yy} \\ G_{xx} &= \frac{1}{XX'} Q_{xx}^2 - \sqrt{\frac{1}{XX'YY'}} Q_{xx}Q_{yy} + \frac{1}{YY'} Q_{yy}^2 \\ G_{yy} &= \frac{1}{XX'} Q_{yy}^2 - \sqrt{\frac{1}{XX'YY'}} Q_{xx}Q_{yy} + \frac{1}{YY'} Q_{xx}^2 \\ G_{xy} &= \frac{1}{XX'} Q_{xx}Q_{yy} - \frac{1}{2} \sqrt{\frac{1}{XX'YY'}} (Q_{xx}Q_{yy} + Q_{yy}^2) + \frac{1}{YY'} Q_{xx}Q_{yy} \\ G_{zz} &= \frac{1}{S^2} Q_{zz}^2 \end{aligned} \right\} \quad (10)$$

NEWS IN BRIEF

Conference on Aviation Service and Test Techniques in Beijing

The Aviation Service Engineering Commission sponsored a conference on aviation service and test techniques in Beijing on November 30 to December 4, 1983. There were 74 participants from 35 organizations. The conference had 23 presentations and 30 papers on subjects including: (1) the development of the test techniques in foreign countries and the progress and the direction of the development of the test techniques in China (2) discussions on the technical difficulties and main problems on aviation service and test (3) reviews on the technical experiences of the aviation service and test technology in China. The research topics were more confined. Most theories were related to practice. Many papers were valuable and elaborated clearly in a theoretical aspect. Some papers had quite distinguishable view points. These technical articles, "New Transducer for Supersonic Test-Main Contact Pressure Transducer", "JK-8211 Inertial Time Monitor" and "Investigation on the External Method of Measurement of the Thrust of the Turbojet Engine" had received favorable comments in the conference.

The test techniques have been regarded as a science in the meeting. The progress of scientific technologies in the recent twenty years has changed significantly the techniques and methods of service. It has changed also the philosophy, the methodology and the organization system of aviation service and doubled the economical benefit on maintenance service. The technical level of aviation service and test is a measurement of the modernization of the maintenance service. Recently we have developed various techniques such as undestructive damage detection, in-situ test, condition monitoring, etc., for aircraft service. The capability of aviation service is improved greatly. The aviation industries have paid great attention to the

Analyses and comparisons of the numerical results of the examples with the corresponding data in references [1] and [2] show that the equivalent strength method of design optimization is reasonable and secure.

The value of the super-relaxation factor, Q , should be selected reasonably to increase the speed of convergence. The introduction of certain details in numerical treatment can avoid the unnecessary stop of the computer at certain unreasonable locally optimized points.

Zhou Shurong, Zhang Yuzhu, Huang Hai and Lu Jilin have participated in the work of calculations and analyses. Rong Xiangtao, Xia Renwei and Zhang Yongshun have provided many valuable comments. Their assistance is gratefully acknowledged.

References

- [1] Khot, N.S., Venkayya, V.B., Johnson, C.D. and Tischler, V.A., Optimum Design of Advanced Composite Structures for Static Loads, AFFDL-TR.
- [2] Harold Switzy, Preliminary Design of Wings, Vol. IV- Minimum Weight Design of Composite Structure, AD A003667, AFFDL-TR-74-20.
- [3] Ma Zhukang, Optimization Design of Composite Symmetrically Laminated Plate According to the Condition of Wrecking by Static Force. Acta Aeronautica Et Astronautica Sinica, Vol. 2, No. 2, (1981).
- [4] Tsai, S.W. and Hahn, H.T., Introduction to Composite Materials, Technomic Publishing Company, (1980).
- [5] Liu Fanglong, Lecture on the Strength of Composite Materials. Beijing Institute of Aeronautics and Astronautics, Research Lecture Room 503 (1981).
- [6] Xia Renwei, Zhang Yongshun, "Fundamentals of Structure Design Optimization." Lecture, Beijing Institute of Aeronautics and Astronautics, Research Lecture Room 503 (1979).

variables, the final design was obtained after 8 iterations to be $\{h\}^* = \{0.0146 \ 0.010 \ 0.2744 \ 0.1134\}^T$ (inch) with $\{R\}^* = \{1 \ 1.008 \ 2.195 \ 2.088\}^T$. Our method is more effective than that of reference [1]. Figure 6 shows the design process. Additional study is needed for certain conditions having multiple combined loads with which the criterion of optimization by equivalent strength cannot be met.

Example 5. A laminated plate was under a combined load, $N_x = 10$ K-lb/in, $N_y = 5$ K-lb/in, $N_{xy} = 3.183$ K-lb/in. Reference [2] used the method of Lagrange multipliers to obtain the optimum thickness, $\{h\}^* = \{0.07013 \ 0.03964 \ 0.0061 \ 0.0061\}^T$ (inch). Test results showed that the values of R_k of individual ply groups were all less than 1. Using our method, the final design was obtained to be $\{h\}^* = \{0.0322 \ 0.003485 \ 0.03983 \ 0.00249\}^T$ (inch), with $\{R\}^* = \{1.04 \ 1 \ 1.04 \ 1\}^T$. Our method is perfect and gives ideal design.

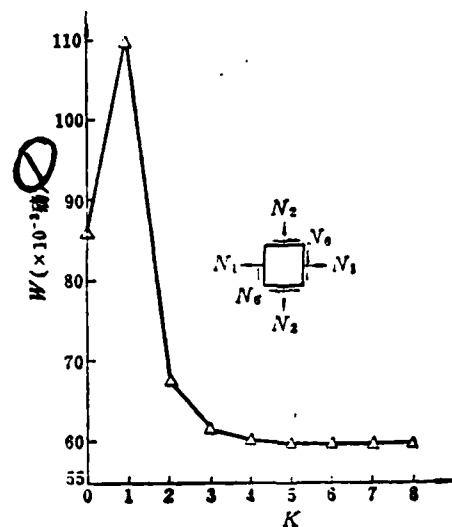


Figure 6. Optimization in design of square laminate under four combined loads

Key: 1. 1b

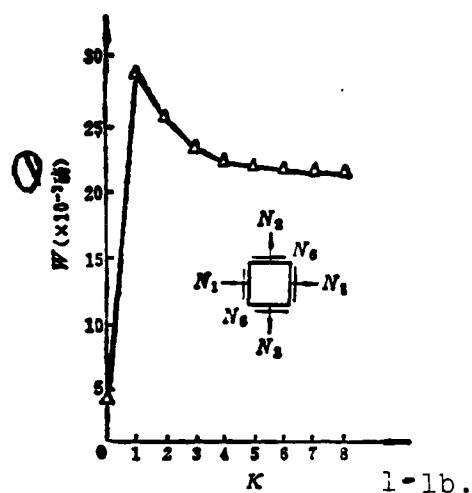


Figure 5. Optimization in design of square laminates under one combined load

Example 4. Similar square laminate was under four types of combined loads as listed in the following table:

载荷情况 ①	N_x 千磅/英寸 ②	N_y 千磅/英寸 ③	N_{xy} 千磅/英寸 ④
1	2.10	-0.60	7.30
2	6.40	8.30	1.85
3	7.30	7.90	19.90
4	1.70	-0.40	6.90

Key:

1. loading condition
2. K-lb/in

The x-axis was parallel to the 0° direction of the fibers. Reference [1] used an initial design by equivalent percentage. The final design after iteration was $\{h\}^* = \{0.06 \ 0.06 \ 0.17 \ 0.17\}^T$ (inch). Test result showed that $\{R\}^* = \{0.964 \ 0.949 \ 2.502 \ 1.956\}^T$, which was within the unfeasible region. Using our method with the same initial design and without using the enveloping method to select the maximum value of the design

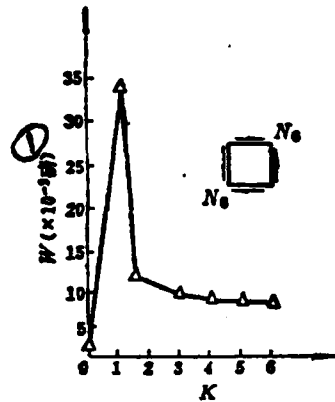


Figure 4. Optimization in design of square laminates under shear loads by equivalent strength

Key:

1. 1b

Table 3 Optimization in design of square laminates under one combined load by equivalent strength

① 迭代次数	重量 $W \times 10^{-3}$ 磅	$h_{0^\circ} \times 10^{-3}$ 英寸	$h_{90^\circ} \times 10^{-3}$ 英寸	$h_{45^\circ} \times 10^{-3}$ 英寸	$h_{-45^\circ} \times 10^{-3}$ 英寸	R_{0°	R_{90°	R_{45°	R_{-45°
0	3.66	5.37	0.69	13.20	5.96	0.128	0.134	0.187	0.213
1	28.62	42.03	5.42	103.3	46.62	1	1.046	1.464	1.665
2	26.01	27.26	3.68	98.12	50.35	1	1.057	1.274	1.416
3	24.64	20.37	2.91	93.38	53.26	1	1.066	1.154	1.265
4	23.81	16.85	2.56	89.08	55.70	1	1.071	1.083	1.172
5	23.26	14.90	2.43	85.35	57.75	1	1.058	1.044	1.108
6	22.92	13.81	2.38	82.59	59.29	1	1.046	1.022	1.070
7	22.69	13.17	2.37	80.48	60.47	1	1.036	1.010	1.047
8	22.53	12.77	2.38	78.83	61.40	1	1.0288	1.0039	1.033

注: $q = 1.0$

Key:

1. number of iterations
2. weight, lb
3. inches

Table 2 Optimization in design of square laminates under shear loads by equivalent strength

迭代次数	重量 $W \times 10^{-3}$ 磅	$h_{0^\circ} \times 10^{-3}$ 英寸	$h_{90^\circ} \times 10^{-3}$ 英寸	$h_{45^\circ} \times 10^{-3}$ 英寸	$h_{-45^\circ} \times 10^{-3}$ 英寸	R_{0°	R_{90°	R_{45°	R_{-45°
0	4.227	0	0	20.09	9.07			0.304	0.407
1	34.62	0	0	161.7	72.96			2.443	2.443
2	11.85	0	0	50.89	30.81			1	1.337
3	10.27	0	0	39.15	31.69			1	1.173
4	9.598	0	0	33.96	32.23			1	1.040
5	9.451	0	0	32.80	32.84			1	1.010
6	9.417	0	0	32.52	32.42			1	1.002

注: $q = 1$

Key:

1. iteration number
2. weight, $W \times 10^{-3}$ lb
3. inches
4. note: $q=1$

Example 3. The same square laminate as above was under one combined load, $N_x = 1.89$ kilo lb/in, $N_y = -0.54$ kilo-lb/in, $N_{xy} = 6.57$ kilo-lb/in, with the x axis along the 0° direction of the fibers. Reference [1] chose an initial design by equivalent percentage. After an unknown number of iterations, the final design was $\{h\}^* = \{0.0199 \ 0.0173 \ 0.05425 \ 0.05425\}^T$ (inch). The strength ratio was tested to be $\{R\}^* = \{0.861 \ 0.833 \ 1.57 \ 1.47\}^T$, which was within the unfeasible region. With an initial design determined by "quasi-network principle", a final design was obtained using our method after 8 iterations to be $\{h\}^* = \{0.01277 \ 0.002383 \ 0.07883 \ 0.0614\}^T$ (inch) with $\{R\}^* = \{1.0 \ 1.0288 \ 1.0039 \ 1.033\}^T$. The iteration process of the design is shown in Table 3 and Figure 5.

Example 1. A 1 inch x 1 inch square laminate was loaded with a unidirectional tension force of 104 lb/in inch along the 0° direction of the fibers. Reference [1] chose an initial design by equal percentage. The dimension of the final design was $\{h\}^* = \{0.076 \ 0.000098 \ 0 \ 0\}^T$ (inch) after 10 iterations using the criterion of equal stress. The final weight was about 61.2% of that of the original design. Tests showed that the final design still had significant excess strength, $R_{0^\circ} = 2.526$, and it should be further optimized. The thickness of the 0° ply was reduced to 0.03795 inch after 10 iterations using our method of optimization. The thickness of the final design was $\{h\}^* = \{0.02841 \ 0 \ 0 \ 0\}^T$ (inch), $R_0 = 1$, with a weight decrease of 85% after 19 iterations. If the initial design was determined using "quasi-network principle", it would be the optimized design. The figures and tables for the calculation are omitted here.

Example 2. The same square laminate of Example 1 was loaded with 104 lb.in shear force. The 0° direction of the fibers was parallel to one side of the plate. An initial design by equivalent percentage was used in Reference [1]. The final design after 10 iterations was $\{h\}^* = \{0 \ 0 \ 0.064 \ 0.064\}$ (inch), 54% decrease in weight, and $R_{\pm 45^\circ} > 1$. Our method of optimization gave a final design, after 7 iterations, to be $\{h\}^* = \{0 \ 0 \ 0.03243 \ 0.03243\}^T$ (inch), 72.6% decrease in weight and $R_{\pm 45^\circ} = 1$. If the initial design was determined using "quasi-network principle", a final design could be obtained after 6 iterations to be $\{h\}^* = \{0 \ 0 \ 0.03252 \ 0.03242\}^T$ (inch), strength ratio $R_{45^\circ} = 1$ and $R_{-45^\circ} = 1.002$. The iteration process of the design is shown in Table 2 and Figure 4. /207

from the initial calculation according to the "quasi-network principle", that is

$$\{h\}^{(0)} = \underset{L=1, \dots, NLD}{\text{Max}} \{h\}_L^{(0)} \quad (24)$$

The flowchart of calculation for optimization in laminate design by equivalent strength is shown in Figure 3.

IV. Examples and Analyses

Five examples were carried out using the optimization program written in FORTRAN language following the flowchart as shown in Figure 3 with the FELIXC-256 and the SIEMENS-7760 computers. For comparison purpose, the examples in references [1,2] are selected for analyses. They are all $\pi/4$ symmetrically laminated plates. The plates were made from boron/epoxy composite materials. The basic mechanical characteristics are shown in Table 1. The thicknesses of the individual plies were 0.005 inch^[1] and 0.0075 inch^[2].

Table 1 Characteristics of B/EP material

E_x	30×10^6 磅/英寸 ² (1)	X	176×10^3 磅/英寸 ² (2)
E_y	2.7×10^6 磅/英寸 ² (1)	X'	390×10^3 磅/英寸 ² (2)
ν_x	0.21	Y	11.4×10^3 磅/英寸 ² (1)
E_z	0.65×10^6 磅/英寸 ² (1)	Y'	44.6×10^3 磅/英寸 ² (2)
ρ	0.725 磅/英寸 ³ (2)	S	2.1×10^3 磅/英寸 ² (1)

Key:

- (1) lb/in²
(2) lb/in²

Key:

1. start
2. initial data input $K = 0$
3. determine the initial values of $\{h\}^{(0)}$ by "quasi-network principle"
4. calculate the initial weight W_0
5. calculate the stiffness matrix $[A]=2$
6. obtain the inverse matrix $[a]=[A]^{-1}$
7. obtain the orthogonal stresses of individual ply groups $\{\epsilon\}_{(k)} = [T_e][\bar{A}]^{-1} \{N\}$
8. set up the matrix of strength ratios $[RR]$
9. let $R_{\min} = \min[RR]_{L,k}$, $L=1,2,\dots,NLD$; $k=1,\dots,4$
10. adjustment by the ray steps method $h_k = h_k / R_{\min}$
11. calculate the strength ratio matrix at the point on boundary surface $[RR]=[RR]/R_{\min}$
12. calculate the weight at the point on boundary surface W_k
13. yes
14. obtain the ply group number
15. stop
16. no
17. modify the design according to the equivalent strength criterion, let
18. obtain new design values using the enveloping method, let $h_k = \max_{L,k} h_{L,k}$

The initial design of the laminated plate can be obtained /206 using the "quasi-network principle". The quasi-network principle considers only the resistance along the direction of the fibers in the unidirectional ply group and neglects the resistance along the lateral and the tangent directions. It neglects also the interactions between individual ply groups. (The "network principle" considers only the resistance of the fibers but not the action of the matrix.) The initial design of the laminated plate under single load, determined according to the "quasi-network principle", is

$$\{h\}^{(0)} = \left\{ \frac{N_1}{2X} \quad \frac{N_2}{2X} \quad \frac{N_3}{2\sqrt{2}X} \quad \frac{N_4}{2\sqrt{2}X'} \right\}^T \quad (23)$$

When N_1 is negative, the compression strength becomes extension strength or vice versa. Under the condition with multiple loads, the initial design of the laminated plate can be determined by selecting, using the enveloping method, from the values obtained

above steps, 1, 2, 3, and 4, until no more weight decreases or the difference of the weights of consecutive iterations reaches the predetermined accuracy.

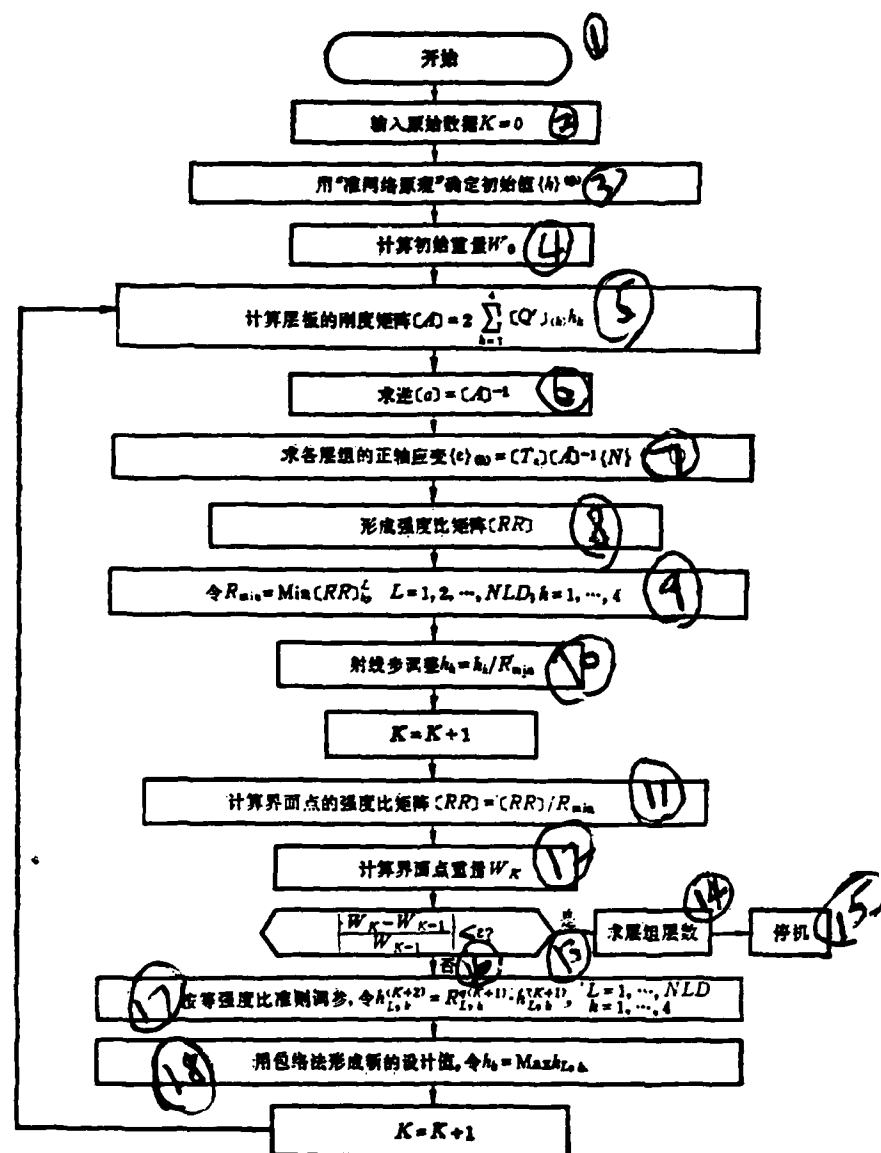


Figure 3. Flowchart of calculation for optimization in laminate design by equivalent strength

III. Procedure of Design Optimization of the Laminated Plates By Equivalent Strength Method

1. Select an initial design $\{h\}^{(0)}$, obtain the strength ratios $R_{L,k}^{(0)}$ ($L = 1, 2, \dots, NLD$; $k = 1, \dots, 4$) of individual ply groups under various loading conditions using Equations (3) and (15).

2. Based on the minimum strength ratio R_{\min} ,

$$R_{\min} = \min R_{L,k} \quad (17)$$

carry out feasibility adjustments using the ray steps method and move the design point to the constraint surface (Figure 2), that is

$$\{h\}^{(k+1)} = \{h\}^{(k)} / R_{\min} \quad (18)$$

and calculate the weight, $W^{(k+1)}$ of the laminated plate

$$W^{(k+1)} = 2 \sum_{k=1}^4 \rho_k F_k h_k^{(k+1)} \quad (19)$$

where ρ_k , F_k —are the specific gravity and the in-plane area of the k -th ply group.

3. Since $[A^*]$ and $\{h\}$ have linear relation, the strength ratios, $R_{L,k}^{(k+1)}$, of individual ply groups of the design point $\{h\}^{(k+1)}$ under various loads can be obtained,

$$R_{L,k}^{(k+1)} = R_{L,k}^{(0)} / R_{\min} \quad (20)$$

and design adjustments can be carried out based on the principle /205 of optimization by equivalent strength, that is

$$h_{L,k}^{(k+2)} = R_{L,k}^{(k+1)} \cdot h_{L,k}^{(k+1)} \quad (21)$$

4. Using the enveloping method, select the maximum value of the design variable $\{h\}_L^{(k+2)}$, of individual ply groups obtained under different carrying loads, that is

$$\{h\}_{\max}^{(k+2)} = \max_{L=1, \dots, NLD} \{h\}_L^{(k+2)} \quad (22)$$

5. Using $\{h\}_{\max}^{(k+2)}$ as the next starting point, repeat the

where q —overrelaxation factor, which can improve the speed of convergence,

$K = 1, 2, \dots, N$ —number of iterations;

the carrying capacity of the laminated plate can be increased effectively with minimum increase of the weight. This provides a condition for further sizable reduction of the weight by the ray steps method to approach the optimum point as shown in Figure 2. The concept of adjustment for optimization, which is accomplished by increasing the cross-section dimensions of the elements (ply groups) having abundant strength and decreasing the cross-section dimensions of the elements lacking in strength, is opposite to the structure of the common isotropic metallic materials.

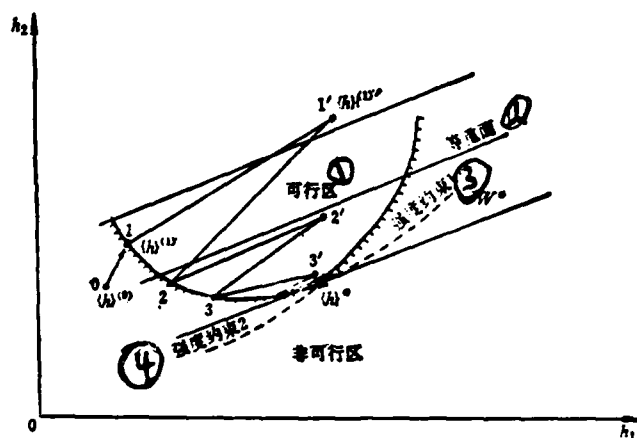


Figure 2. Optimization in laminate design by equivalent strength

- Key:
1. surface of equivalent weight
 2. feasible area
 3. strength constraint 1
 4. strength constraint 2

where

$$\left. \begin{aligned} A &= G_{xx}\varepsilon_x^2 + 2G_{xy}\varepsilon_x\varepsilon_y + G_{yy}\varepsilon_y^2 + G_{zz}\varepsilon_z^2 \\ B &= G_{xz}\varepsilon_x + G_{yz}\varepsilon_y \\ C &= -1 \end{aligned} \right\} \quad (14)$$

Under certain loading conditions, the strength ratios, $R_{L,k}$ of individual ply groups of the common $\pi/4$ symmetrically laminated plate are given by

$$R_{L,k} = \left| \frac{-B_k^L \pm \sqrt{B_k^{L^2} - 4A_k^L C_k^L}}{2A_k^L} \right| \quad (15)$$

where $L = 1, 2, \dots$, NLD — loading conditions.

For any arbitrary design point, the strength ratios of individual ply groups, $R_{L,k}$, are not equal. They may be greater than 1 or less than 1. For optimum design, the thicknesses of individual ply groups, h_k , should be adjusted such that the strength ratios of individual ply groups $R_{L,k}$, will all equal 1 under one loading condition. The design obtained at such condition is the optimized design of the laminated plate, which is different from the design obtained by the concept of full stress.

If the strength ratio of a ply group in certain directions is the highest under load, this ply group should have the highest strength and highest carrying capacity. Increasing the thickness of this ply group can effectively increase the carrying capacity of the laminated plate with minimum increase of the total weight. The ply groups with lower strength ratios have lower carrying capacity. Reducing properly the thicknesses (or layers) of these ply groups or eliminating the ply groups having poor carrying capacity can improve greatly the utilization of materials and reduces effectively the weight of the laminated plate. Design modifications for optimization can be carried out directly and simply by using the method of equivalent strength ratio. With

$$h_{L,k}^{(K+1)} = R_{L,k}^{(K)} \cdot h_{L,k}^{(K+1)} \quad (16)$$

X, X', Y, Y', S — are the orthogonal longitudinal extension, compression, lateral extension, compression and the in-plane shear strength of the unidirectional plate respectively.

/203

Given the internal forces $\{N\}$ within the laminated plate, the orthogonal strains $\{\epsilon\}_k$ corresponding to any arbitrary group of design variables $\{h_k\}$ can be obtained from equation (3). A value can be obtained by substituting the values of the strains into equation (8). If the value equals to 1, it indicates the unidirectional plate is deformed. If the value is less than 1, no deformation of the plate will occur.

3. Criterion for Design Optimization by Equivalent Strength

In order to estimate the loading abilities of individual ply groups of the symmetrically laminated plate, we have introduced an additional parameter, the strength ratio.

$$R = \frac{\{\epsilon\}_{(a)}}{\{\epsilon\}} \quad (11)$$

where $\{\epsilon\}_{(a)}$ — maximum or available orthogonal strain vectors,
 $\{\epsilon\}$ — orthogonal working strain vectors of the unidirectional plate.

Since in the static experiment for determining the structure strength the loads are added proportionally, the assumption that the strain vector increases along the same direction as the load is applicable for composite materials having good linearity. The strength ratio R , defined in Equation (11) is also applicable for individual components of the strains, that is

$$R = \frac{\epsilon_{i,(a)}}{\epsilon_i}, \quad i = x, y, s \quad (12)$$

Since Equation 8 is the deformation criterion for a unidirectional plate, the criterion is satisfied until the working strain reaches the maximum available value. Substituting Equation (12) into Equation (8), it gives

$$AR^2 + BR + C = 0$$

$$R = \left| \frac{-B \pm \sqrt{B^2 - 4AC}}{2A} \right| \quad (13)$$

performance of service and maintenance in new designs or manufacture of the aircraft. However, our techniques are still behind those of the foreign countries. We lack systematic theoretical guidance and the service and test techniques have not been seriously considered in general in various stages including design, manufacture, education, research and practical usage. The conference has suggested (1) to set up a technical group specialized in aviation service and test, (2) to develop job positions and to set up research organizations in various departments involving maintenance and service to resolve the difficulties in service and test and to investigate various problems in test equipment, design, production and standardization, (3) to improve the capability and reliability of the methods of test and detection and to reinforce the research in new techniques of test and detection such as micro-processor, acoustic emission, laser photography, techniques of condition monitoring, etc.

Abstract

This paper introduced the modal test and parameter identification of a flutter wing model with external missiles. The emphasis was placed on improving the reliability and accuracy. An identification program was developed and the first nine orders of modal parameters were identified on an ordinary computer. The reliability and accuracy of the test data and the identification results were verified by four data examining techniques.

I. Introduction

In order to satisfy the design specification of aircraft flutter and dynamic response, and to further actively control flutter and response, and to modify the finite element model, it is necessary to accurately measure the dynamic characteristics of the structure. For a complex structure such as an aircraft, it is still a research subject to improve the reliability and accuracy of the modal parameters identified.

In recent years, the admittance frequency response test for parameter identification and modal analysis has been used in aeronautics and astronautics in the world. It has been successfully applied in the ground vibration test for aircraft components (such as the vertical tail of F-4)^[1] and the entire aircraft (such as Boeing-747 and its modifications)^[2], as well as in tests of flutter models with active control inside and outside the wind tunnel (such as the YF-17 wing with external

*Received in June 1983

missiles)^[3].

The object of this study was the flutter model of a wing with external missiles. The focus was to improve the reliability and accuracy of the experimental modal analysis. A modal parameter identification program^[4] developed in recent years based on a complex modal vibration theory was used. Various methods were employed to examine the accuracy and reliability of the test results. Without additional special analytical equipment, the anticipated high accuracy was attained.

II. Theoretical Basis of Frequency Domain Modal Analysis

The dynamic differential equation for an N-dimensional linear discrete system is

$$[M]\{\ddot{x}\} + [C]\{\dot{x}\} + [K]\{x\} = \{f(t)\} \quad (1)$$

where $[M]$, $[K]$ and $[C]$ are real coefficient symmetric matrices. $[M]$ is a positive definite matrix. $[K]$ and $[C]$ are positive definite or quasi-positive definite. Assuming the initial condition is zero, we can get the following by taking the Laplace transform on both sides:

$$[s^2[M] + s[C] + [K]]\{X(s)\} = \{F(s)\} \quad (2)$$

It may be written in simpler terms as

/212

$$\{Z(s)\}\{X(s)\} = \{F(s)\} \quad (A)$$

or

$$\{H(s)\}\{F(s)\} = \{X(s)\} \quad (3)$$

where

$$\{H(s)\} = \{Z(s)\}^{-1} = \frac{\text{adj}\{Z(s)\}}{\det\{Z(s)\}} \quad (4)$$

It is called the generalized dynamic flexibility matrix or the transfer function matrix.

Let S_r and $\{\psi_r\}$ be the eigen value and eigen vector of equation (2), respectively. For an ordinary viscous damping system both are complex numbers appearing in conjugates. For a

stable sub-critical damping system, we can assume that

$$s_r = -\alpha_r + j\beta_r, \quad s_r^* = -\alpha_r - j\beta_r, \quad (5)$$

It satisfies the following eigen function.

$$\begin{aligned} \det[Z(s)] &= |s^2[M] + s[C] + [K]| = |M| \prod_{r=1}^N (s - s_r)(s - s_r^*) \\ &= |M| \prod_{r=1}^N (s^2 + 2\alpha_r s + (\alpha_r^2 + \beta_r^2)) = 0 \end{aligned}$$

Let ω_r and S_r be the r th order modal frequency \otimes and damping ratio, respectively. We get

$$\alpha_r = \zeta_r \omega_r, \quad \beta_r = \sqrt{1 - \zeta_r^2} \omega_r, \quad (6)$$

According to eq (4), the element of $[H(S)]$ is a rational function of S . The denominator is a $2N$ order polynomial of S and numerator is a $2(N-1)$ order polynomial of S . The transfer function matrix can be expanded at the pole with respect to S_r .

$$[H(s)] = \sum_{r=1}^N \left(\frac{[A_r]}{s - s_r} + \frac{[A_r^*]}{s - s_r^*} \right) \quad (7)$$

where $[A_r]$ is the residual matrix corresponding to the pole S_r (and $[A_r^*]$ is its conjugate).

By multiplying both sides of equation (7) on the left by $[Z(S)](S - S_r)$ and letting $S = S_r$, we get

$$[Z(s_r)][A_r] = 0$$

Hence, we know that a column of $[A_r]$ is proportional to $\{\psi_r\}$. Similarly, by multiplying both sides by $(S - S_r)[Z(S)]$ on the right and letting $S = S_r$, we notice that

$$[Z(s)]^T = [Z(s)]$$

Therefore,

$$[Z(s_r)][A_r]^T = 0$$

This again proves that a row of $[A_r]$ is proportional to $\{\psi_r\}^T$. Hence, we get

$$[A_r] = \frac{\{\psi_r\} \{\psi_r\}^T}{\rho_r} \quad (8)$$

where ρ_r is a proportionality constant (usually a complex number). We can prove that

$$\rho_r = \{\psi_r\}^T [2s_r[M] + [C]] \{\psi_r\} \quad (9)$$

When the damping of the system is structural and proportional, the evolution of $\{\psi_r\}$ is the characteristic vibration modal $\{\phi_r\}$. Thus, we get $\rho_r = 2\beta_r m_r$ where $\beta_r = \sqrt{1-\xi_r^2} \omega_r$ and $\omega_r = \{\phi_r\}^T [M] \{\phi_r\}$ is the r th order real modal mass. Substituting equations (8) and (9) into (7), we can obtain the analytical expressions for the transfer function matrix and real modal parameters.

* Obviously, $\omega_r = S_r$. In reference [5] it was called the characteristic vibration frequency, which is different from the dampingless characteristic frequency^[5].

$$[H(s)] = \sum_{r=1}^N \frac{\{\phi_r\} \{\phi_r\}^T}{m_r (s^2 + 2\zeta_r \omega_r s + \omega_r^2)} = \sum_{r=1}^N \frac{\{\bar{\phi}_r\} \{\bar{\phi}_r\}^T}{s^2 + 2\zeta_r \omega_r s + \omega_r^2} \quad (10) \quad /213$$

where $\{\bar{\phi}_r\} = \{\phi_r\} / \sqrt{m_r}$ is a normalized characteristic vibration mode, which is analytically related to the residual number by the following

$$\{\bar{\phi}_r\} \{\bar{\phi}_r\}^T = -2Im[A_r] \beta_r \quad (11)$$

Let $s = j\omega$ and then the element at the p th row and q th column of the transfer function matrix, $H(j\omega)_{qp}$, is the frequency response function to an excitation on the p -axis measured on the q -axis.

$$H(j\omega)_{qp} = \sum_{r=1}^N \frac{\bar{\phi}_{qr} \bar{\phi}_{pr}}{(\omega_r^2 - \omega^2) + j2\zeta_r \omega_r \omega} \quad (12)$$

Obviously, a unique correlation between the multiple frequency response measured at many points ($q = 1, 2, \dots, N$) by a single excitation point and all real modal parameters is established.

III. Modal Test Techniques

There are two advanced admittance frequency response techniques. One is to use a transient or random wide band excitation followed by FFT frequency response analysis. The

other involves a steady-state sinusoidal excitation followed by "track filtering" of the force and the response to determine the frequency response data^[6]. The advantage of the former is its fast speed. The disadvantages are its low signal to noise ratio and poor frequency resolution. The latter has opposite advantages and disadvantages. We combined both methods. First, we used a wide band excitation to determine the approximate frequency of each modal by FFT analysis. Then a digital high resolution scan was done near each modal to print out the frequency response. Figures 1 and 2 show the force and frequency response curves of a wing and a wing with external missiles obtained by FFT analysis under a pseudo-random excitation, respectively. In the frequency band measured, the former has 5 modals and the latter has 13 modals.

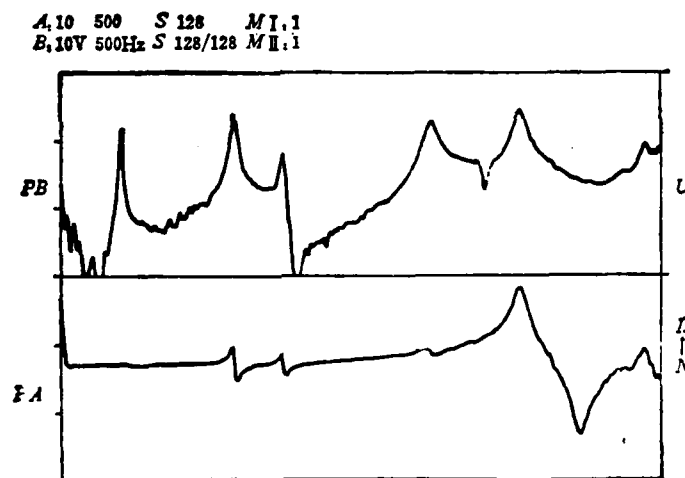


Figure 1. Power spectrum of excitation force and acceleration response

In order to correlate experimental results to the finite element mathematical model, the point of measurement was chosen to be the node of the finite element. The finite element model of the specimen is shown in Figure 3.

The excitation device is connected to the specimen through a force transducer and a miniature connector. The point of connection was chosen to be near the root of the wing (p=29) to

minimize the effect of added mass. The response signal is obtained from a miniature acceleration sensor (weighing 0.5g) and a charge amplifier.

/214

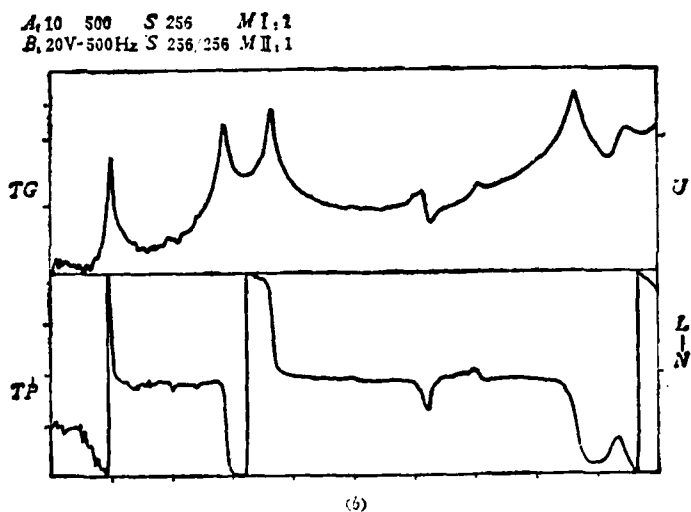
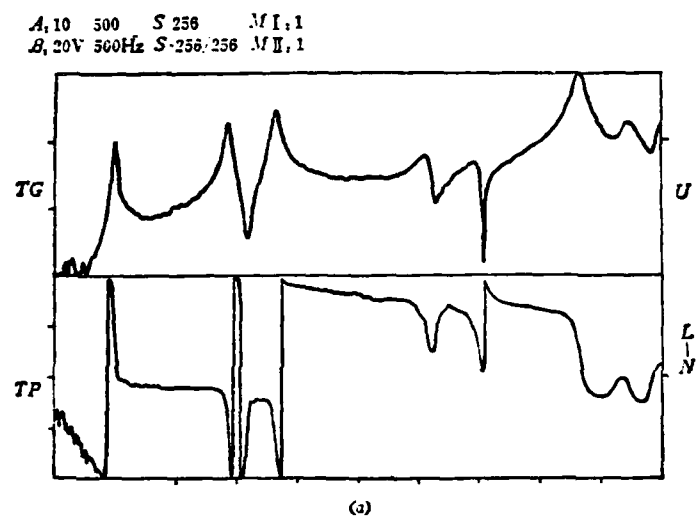


Figure 2. Frequency response curve (Bode's curve)

Because the frequency response data for modal parameter identification are not dimensionless (the acceleration admittance frequency response: $1/\text{kg}$) and the accuracy of a normalized mode is directly affected by the accuracy of the test system, we used a system specification method^[6]. A 10kg standard mass block was used for system specification. In the entire frequency band tested (0~360 Hz), the acceleration admittance frequency response is 0.094~0.096. The error is less than 2%.

/215

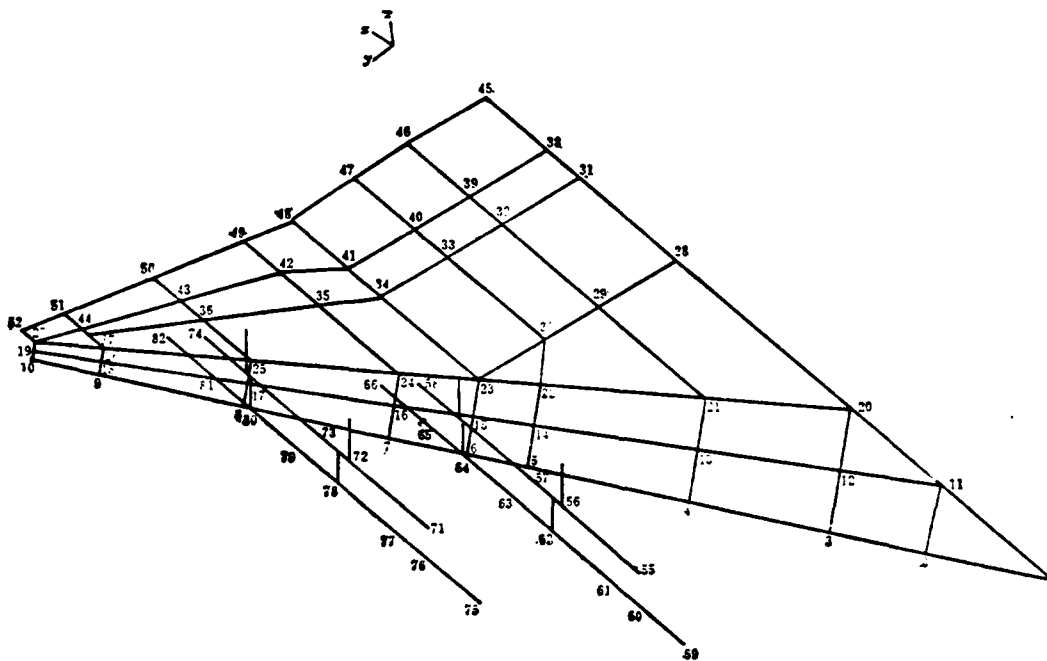


Figure 3. Finite element model of the test specimen

IV. Modal Parameter Identification and Its Results

In spite of the fact that the object of this work is a small damping system, it is possible to use real modal parameters to describe its dynamic properties. When we compiled the identification program, the complex modal theory, eq (7), was used as the basis. After identifying the complex frequency S_r

and complex residual number A_r , a real vibration mode could be "extracted" from equation (11) to solve this problem.

In eq (7), we separated the real and imaginary parts of S_r and A_r by letting $S = j\omega$.

$$s_r = -\alpha_r + j\beta_r, \quad A_r = u_r + jv_r \quad (13)$$

We get

$$H(j\omega)_{qr} = \sum_{r=1}^{N_1} \left(\frac{(u_r)_{qr} + j(v_r)_{qr}}{\alpha_r + j(\omega - \beta_r)} + \frac{(u_r)_{qr} - j(v_r)_{qr}}{\alpha_r + j(\omega + \beta_r)} \right) + (H_c^R + jH_c^I)$$

where N_1 is the number of modes in the measured frequency band ($N_1 < N$); H_c^I and H_c^R are "residual admittance" introduced to compensate the modal cutoff. $u_r, v_r, \alpha_r, \beta_r$ ($r = 1, 2, \dots, N$), H_c^I and H_c^R are parameters to be identified ($4N_1 + 2$ in total).

Corresponding to each test frequency ω_i ($i = 1, 2, \dots, N_m$ usually $N_m > 4N_1 + 2$), there are N_m non-linear algebraic equations. The standard deviation of the measured and estimated frequency response values for each ω_i is the target function (which can be expressed as a generalized function of parameters to be identified). The modal identification problem was thus converted to a non-linear least square optimization problem, which could be solved by an iterative method^[7].

Tables 1 and 2 show the results of modal identification of the first model.

The modal frequency and damping ratio of each state in the second model were referred to in reference [8]. The vibration patterns are also shown in the article.

Table 1 Modal frequency and damping ratio of the wing model /216

r	1	2	3	4	5
f_r, ζ_r					
$f_r(\text{Hz})$	49.4	143.7	183.6	311.0	352.5
$\zeta_r(\%)$	0.45	0.54	0.48	0.80	1.28

Table 2 Modal frequency and damping ratio of the wing model with two external missiles

f, ζ	1	2	3	4	5	6	7
$f, (\text{Hz})$	33.0	35.6	39.0	47.8	78.3	100.4	113.8
$\zeta, (\%)$	0.59	0.61	0.64	—	—	0.67	—

f, ζ	8	9	10	11	12	13
$f, (\text{Hz})$	161.6	183.1	220.0	251.2	290.1	314.1
$\zeta, (\%)$	0.48	0.45	0.72	—	1.06	0.90

V. Accuracy Examination and Discussion

In order to ensure the reliability of the measured frequency response data and the accuracy of the identified modal parameters, we used a number of examining techniques.

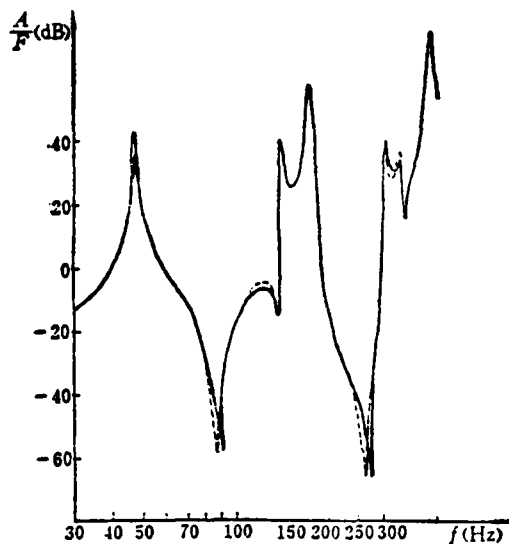


Figure 4. Results of reciprocity check

1. Reproducibility of Frequency Response Data: During the beginning and ending periods of the experiment, frequency response at several points was repeatedly tested. The result is /217 that the error on the frequency response data near each mode is less than 5%-10%.

2. Reciprocity of Frequency Response: From the definition of the frequency response matrix, it is reciprocal. This means that the frequency to excitation at p measured at q is the same as that measured at p due to excitation at q. Figure 4 shows the acceleration admittance response curve corresponding to points 29 and 32 (Bode diagram). The two coincide well. There is some difference near the anti-resonance frequency because there are screw holes near these two points which caused some deviations.

3. Verification of Accuracy of Modal Frequency and Damping Ratio: In a linear system, modal frequency and damping ratio should, in principle, be independent of the coordinate of the point of measurement. In reality, results of identifications are scattered. The scatter of the root mean square can be used as an

indicator for accuracy. In this experiment, the statistical frequency error is less than 0.5% and that of the damping ratio is less than 9%.

4. Orthogonality of Vibrational Mode Accuracy: The maximum non-diagonal element in the normalized modal mass matrix obtained from the identified normalized vibration modal data is less than 9%, which is superior over the 10% accuracy specification in the world. The rest of the orthogonality test results are shown in reference [8].

5. Curve Fitting: This is a reliable examining technique to verify the accuracy of the identified modal parameters and the reliability of the test data. The identified modal parameters are used to construct a mathematical model for the frequency response to derive a fitted curve. This curve is used to compare with the data points. Figure 5 shows the fitting of a wing with the Nyquist curve.

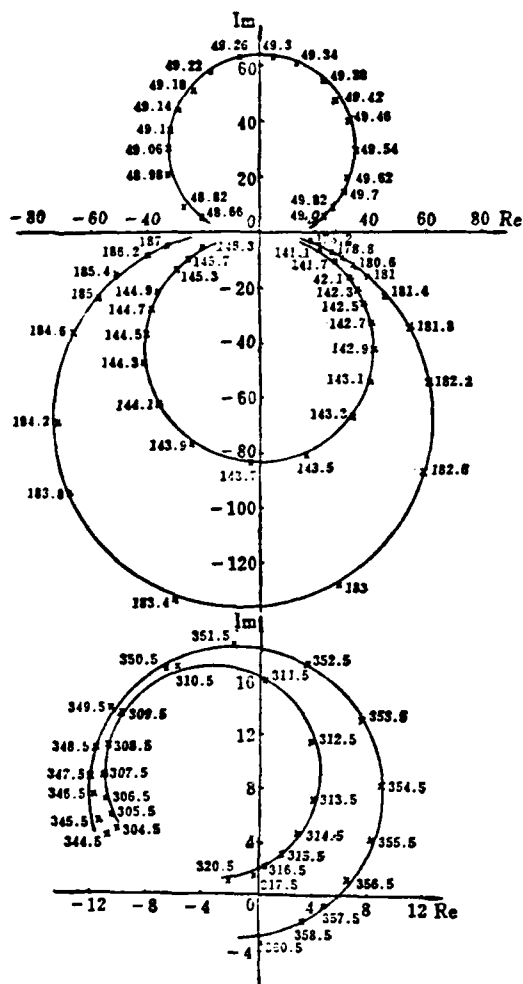


Figure 5. Nyquist's curve fitting

A special problem in this work was that the specimen was a small and complex structure. The entire wing model is under 2.5 kg. The weight of the 4 nodal point at the wing tip was less than 10g. If the conventional resonance method is used to determine the mode, a relative error will be introduced even if we use a 0.5 g miniature acceleration meter. Table 3 shows the first order mode of the trailing edge obtained by the parameter identification and by the conventional resonance method. At the wing tip, ($q = 52$) the relative error is 25% using the resonance

method.

Table 3 1 th Mode shape of trailing edge of the wing model

端点号数	46	47	48	49	50	51	52
共振法	7.23	15.6	28.6	35.7	42.0	50.4	54.5
识别法	7.26	16.0	29.4	37.3	61.2	64.5	72.4

VI. Conclusions

/218

This experimental study shows that admittance measurement and parameter identification is a feasible and highly accurate method for modal analysis. This method is superior over other techniques such as resonance and pure modal identification by multiple point excitation, especially for small flutter models. The frequency response was measured by steady-state sinusoidal excitation and digital coherent analysis, which has a higher accuracy than the wide band excitation, FFT analysis technique. The first model parameters were identified on a Model 709 computer using our own program. The second model was completed on a microprocessor. The test equipment required included a universal frequency response analyzer and Chinese made power amplifier, excitation device, transducers, and charge amplifiers. It is suited for promotion. Various examining techniques presented in this work ensured the reliability and accuracy of the modal analysis. The shortcoming of this technique is that there is a great deal of preparatory work in parameter identification. This is due to off-line processing. Recently, we have successfully developed an on-line modal identification technique.

AD-A158 454

ACTA AERONAUTICA ET ASTRONAUTICA SINICA (SELECTED
ARTICLES)(U) FOREIGN TECHNOLOGY DIV WRIGHT-PATTERSON
AFB OH W JI ET AL. 05 AUG 85 FTD-ID(R5)T-1515-84

3/3

UNCLASSIFIED

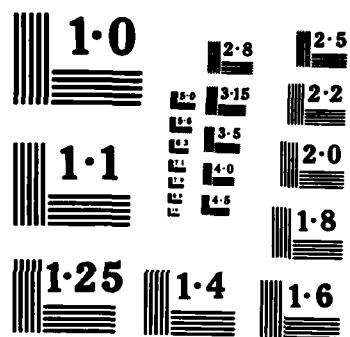
F/G 1/3

NL

END

FILMED

DTIC



NATIONAL BUREAU OF STANDARDS
MICROCOPY RESOLUTION TEST CHART

References

- [1] Gordon, R.W., Wolfe, H.F., Modal Investigation of Lightweight Aircraft Structures Using Digital Technique, S & V. Bull., V47, (1977).
- [2] D. Gimmestad, Your Next Ground Vibration Test Doesn't Have to Cost a Million Dollars, 22th S.D.M. Conference, (1980).
- [3] Hwang, C., et al, Recent Development of the YF-17 Active Flutter Suppression System, 21th S.D.M. Conference, pt 1. (1980).
- [4] Zhang Lingmi, Transfer Function and Modal Parameter Identification in Structure Analysis, Journal of Solid Mechanics, No. 1, (1982).
- [5] Ni Jinfu and Zhang Arzhou, Problems Concerning Complex Modal Theory, Journal of Nanjing Aeronautic Institute, Vol. 42, (1982).
- [6] Zhang Lingmi, Application of Mechanical Resistance in Vibration Analysis, Mechanical Strength, No. 2, (1980) (Special Issue).
- [7] Zhang Lingmi, Application of Mechanical Resistance in Vibration Analysis, Aerospace Technology, No. 2 (1981).
- [8] Zhang Lingmi, Sun Jiuhou and Xiao Yuying, Modal Identification of Flutter Modal of a Wing with Missiles, Technical Document in Chinese Aviation, HJB 830106.

An Experimental Study on the Effect of Overload on Fatigue Life* /219

Zeng Chunhua and Guo Kangmin

(Institute of Mechanics, Academia Sinica)

Abstract

There are many factors which affect the fatigue life, but residual stress and overload are the most important. Overload in a metal can improve its fatigue strength markedly. Based on a large number of tests, the effects of the overload on fatigue crack initiation life, fatigue crack propagation life, fatigue cumulative damage cyclic rate and crack propagation retardation are researched.

Experimental data on the influence of overload on the fatigue initiation life are summarized in a table. In order to compare the influence of overload on fatigue crack propagation life with crack propagation retardation effect, a $\sim N$ curves are used for demonstrating the experimental results of three notched specimens. Finally the effect of overload on fatigue life is explained in the view of residual stress.

I. Introduction

Recently, many investigators have been interested in the effects of overload on fatigue life and the importance of the effects are recognized gradually. The mechanism of overload is the theoretical basis of fatigue design for controlling the fatigue life and improving the fatigue strength of materials. Several overload retardation models have been developed recently in foreign countries^[1-5]. However, most papers are focused on the effect of overload on the fatigue crack propagation; only very few papers have discussed the effects of overload on the fatigue crack initiation life and the fatigue cumulative damage cyclic rate.

*Received in May 1983

We have studied the effects of overload on the fatigue crack initiation life, fatigue crack propagation life, fatigue cumulative damage and crack propagation retardation based on the experimental fatigue tests on 15MnVN, 28Cr2NiMoV alloys and the LY12CZ aluminum alloy. The residual stresses at the base of the notches caused by overload have been measured. Resealing of the crack, crack retardation and the effect of overload on fatigue life are explained from the point of view of residual stress.

II. The Effect of Overload on Fatigue Crack Initiation Life

The fatigue damage usually involves four stages: these are fatigue nucleation period, micro-crack propagation period, macro-crack propagation period and the breaking period. The fatigue crack initiation life is referred to as life of the fatigue nucleation period and the micro-crack propagation period. There is no consistent criterion in the world for the length of the crack to be regarded as the end of the fatigue initiation stage. We have used the criterion employed by the majority that the formation of a 1mm crack on the testpiece is the end of the fatigue initiation stage.

We have used four 15MnVN, four 28CrNi3MoV and three 25Cr2NiMoV notched testpieces to study the effect of overload on the fatigue crack initiation life. The sizes of the testpieces are shown in Figure 1. Different overloads were applied on the testpiece and the residual stress at the base of the notch was measured by an X-ray stress analyzer. Equal space three points bending loads are then applied on the testpieces using the West German Schenck fatigue test instrument with a stress ratio $R = 0.5$ and frequency of 40 Hz. A microscope was used to detect the formation of 1mm fatigue crack on the testpiece and the cycle number was recorded. The test results were used as a basis to analyze the effects of different overloads on the fatigue initiation life of various materials.

The experimental results are summarized in Table 1.

/220

Table 1 Test results of effect of overload on fatigue crack initiation life

材料 ①	15MnVN		28CrNi3MoV		25Cr2NiMoV	
	超载 ③	形成寿命N次 ④	超载 ③	形成寿命N次 ④	超载 ③	形成寿命N次 ④
② 试件 1	无 ⑤	0.087×10^5	无 ⑤	0.28×10^5	无 ⑤	1.359×10^5
试件 2	41.4% σ_s	0.795×10^5	32.7% σ_s	9.47×10^5	60% σ_s	3.460×10^5
试件 3	48.3% σ_s	1.243×10^5	38.4% σ_s	0.925×10^5	70% σ_s	9.659×10^5
试件 4	55.2% σ_s	1.620×10^5	43.6% σ_s	1.07×10^5		

Key:

1. material
2. testpiece #1
3. overload
4. cycle number of initiation life
5. none

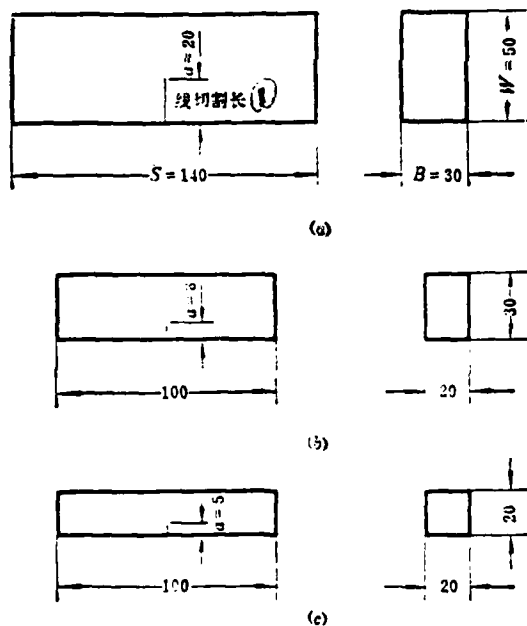


Figure 1. Notched fatigue testpieces

- key: (a) 15MnVN (b) 28CrNi3MoV (c) 25Cr2NiMoV
1. length of linear notch
 2. unit: mm

III. The Effect of Overload on Fatigue Crack Propagation Life

The fatigue crack propagation life includes the stage of macro-crack propagation and the stage of final breaking, which is the life to final breaking after the formation of a 1mm crack. The same 11 testpieces were used to investigate the effect of overload on the propagation life. The amounts of overload as listed in Table 1 were applied on the testpieces after the cracks propagated to 5 mm and the residual stresses at the base of the notches were measured. The testpieces were then tested using Schenck fatigue tester with the same loads as those applied in the crack initiation stage. The propagation of the cracks was observed using a microscope. The cycle number for each fixed increment of crack length was recorded until the crack propagated to a critical length. The relation curves of the crack length, a , vs. loading cycles were then obtained. These curves were used as bases for analyzing the effect of overload on the fatigue propagation life.

Figures 2 to 4 show the test results of the effects of overload on the fatigue propagation lives of the notched specimens of three types of materials.

/221

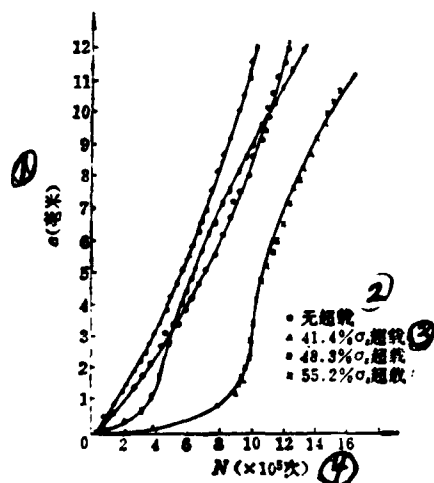


Figure 2. $a \sim N$ curves of 15MnVN steel notched testpieces

Key:
1. a (mm)
2. no overload

3. % overload
4. N ($\times 10^5$ cycles)

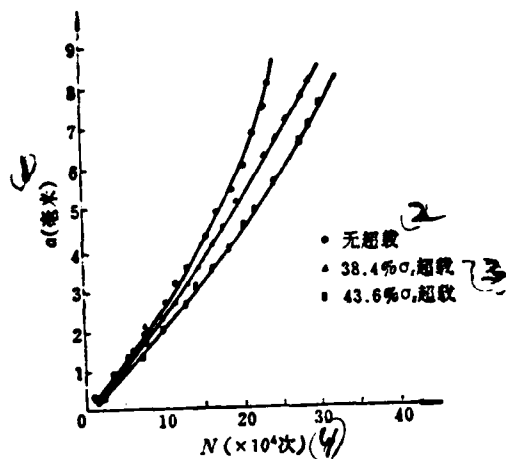


Figure 3. $a \sim N$ curves of 28CrNi3MoV steel notched testpieces

- Key:
1. a (mm)
 2. no overload
 3. % overload
 4. (--- cycles)

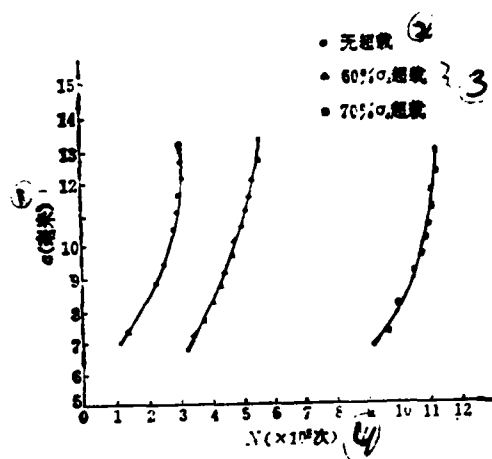


Figure 4. $a \sim N$ curves of 25Cr2NiMoV steel notched testpieces

- Key:
1. a (mm)
 2. no overload
 3. % overload
 4. (--- cycles)

IV. The Effect of Overload on Fatigue Cumulative Damage

Fatigue damage refers to the damage of the material under cycling load. The microcracks of the material grow progressively and deeply under the cycling load which decreases significantly the effective working surface of the material. Miner proposed a theory of linear cumulative damage in 1945. Many investigators have indicated later that the damage cyclic rate (i.e., $\sum n/N$) is not necessary to be 1 when the material reaches fatigue damage. The value deviates from 1 slightly for most cases, but significant deviation is also observed occasionally. This deviation is because Miner's theory has not considered the interaction between the stresses. There are many factors which affect the $\sum n/N$ value. Overload is one of /222 the main factors.

We have carried out fatigue tests on center notched plate testpieces of LY12CZ aluminum alloy to study the effect of overload on cumulative damage cyclic rate, $\sum n/N$. The dimension of the testpiece is shown in Figure 5. The loading stress was divided into five consecutive levels from low to high. Each overload was added after 12 testpieces were cycled. The values of overload were $45\sigma_s$, $55\sigma_s$ and $75\sigma_s$. The overload tests were carried out using a Swiss Ansler high frequency fatigue tester. Cycling was continued until fatigue damage occurred. Five to eight specimens were tested for each loading. The cumulative damage cyclic rate, $\sum n/N$, of each testpiece was obtained from the cycling life and the corresponding fatigue curve. The effect of overload on the cumulative damage was analyzed based on logarithmic average of the damage cycling rate. The results of tests and calculations are shown in Table 2.

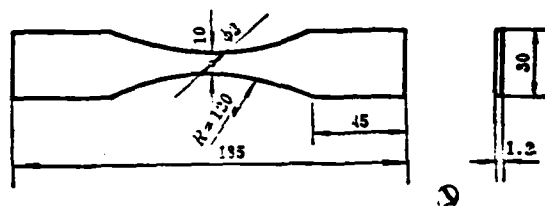


Figure 5. LY12CZ aluminum alloy center notched plate testpiece

1. --unit: ml

Table 2 Test results of effect overload on damage cyclic rate

① 超載量	② 疲勞累積損傷周比值 $\Sigma \frac{n}{N}$								④ 平均
③ 試件 1	2	3	4	5	6	7	8		
45% σ_r	1.6373	2.4845	1.7715	3.3809	3.1217	2.2622	1.7800	1.6710	2.0300
55% σ_r	6.7685	7.1510	6.9530	6.9570	6.9490				6.9530
75% σ_r	8.9670	4.3900	16.8500	16.4050	13.3440				13.9600

Key:

1. amount of overload
2. fatigue cumulative damage cyclic rate, $\Sigma n/N$
3. testpiece #
4. average

V. The Effect of Overload on Crack Retardation

In the process of equal space loading, the propagation rate of the crack after each or several peak tensile loads will reduce gradually to its original level after several cycles. This slowdown phenomenon of the rate of crack propagation caused by overload is referred to as the crack propagation retardation effect. /223

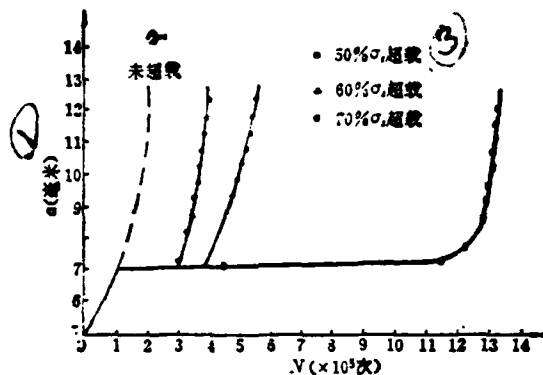


Figure 6. Retardation effect curves of crack propagation of 25Cr2NiMoV steel notched testpieces

Key:

1. mm
2. no overload
3. overload

We have tested three 25Cr2NiMoV steel notched specimens to study the retardation effect of overload. The dimension of the testpieces is shown in Figure 1(c). A crack of 2 mm was first initiated using the fatigue test machine and the overloads of $50\sigma_s$, $60\sigma_s$ and $70\sigma_s$ were then added respectively. After the residual stress at the base of the crack was measured, the test was continued and the crack propagation was examined using a microscope to study the influence of overload on the retardation effect of crack propagation. The retardation curves of crack propagation are shown in Figure 6.

VI. Conclusion and Analysis

1. The experimental results indicated that the tensile overload affected greatly the fatigue crack initiation life. Overload increased significantly the crack initiation life of the three types of steel testpieces. The crack initiation life of 15MnVN steel testpiece under $55.2\sigma_s$ tensile overload was over 19 times that of a testpiece without overload. The crack

initiation life of 28CrNi3MoV steel testpiece under $43.6\%\sigma_s$ tensile overload was over 5 times that of a testpiece without overload. The crack initiation life of 25Cr2NiMoV steel under $70\%\sigma_s$ tensile overload was 7.5 times that of a testpiece without overload.

2. The experimental data showed that the crack initiation life of all three types of steels increased with increasing tensile overload and was closely related to the residual stress. Tensile overload created residual compression stress at the base of the notch as shown in Table. 3. Within a certain limit, the residual compression stress is beneficial to the fatigue life; it increases the fatigue resistance of the material and retards the formation and propagation of the fatigue crack, and therefore the fatigue life of the specimen is greatly improved.

3. The experimental results indicated that tensile overload also significantly affected the fatigue crack propagation life. Overload greatly increased the fatigue crack propagation life of all three types of steel specimens. The life of 5 mm crack propagation of a 15MnVN steel under $55.2\%\sigma_s$ overload was about 4 times that of a testpiece without overload. The life of 2 mm crack propagation of 25Cr2NiMoV steel testpiece under $70\%\sigma_s$ tensile overload was 9 times that of a testpiece under $50\%\sigma_s$ overload, and was many more times that of a testpiece without overload.

4. The test results showed that the $a-N$ curves shifted to the right along the x-axis with increasing tensile overload. The shifting was less significant when the tensile overload increased. It was also related to the residual stress at the base of the notch. The residual stress was mainly caused by non-uniform plastic deformation. Within certain limits, the plastic deformation at the base of the crack increased with increasing tensile overload. It is well known that the peak overloads retard the fatigue crack propagation. The retardation process occurs when the crack passes the plastic region. The amount of retardation depends on the distance of the crack passing through the plastic region. The larger the plastic region is, the longer

the retardation time will be or the longer the time for resealing the crack is. The resealing phenomenon of the crack retards the fatigue crack propagation and increases the fatigue crack propagation life.

5. Overload has significant effect on the fatigue cumulative damage cyclic rate. Tests and calculations showed that the addition of a tensile overload before applying the cyclic overload could increase the damage cyclic rate, $\Sigma n/N$ for several times. Within a certain limit, $\Sigma n/N$ increased rapidly with increasing overload and overload had a beneficial effect on the fatigue life. Since overload causes plastic deformation at the base of the crack, the plastic deformation increases with increasing overload. Since the area around the plastic region is still in an elastic state, the plastic region is under compression when the overload is released. This creates a residual compression stress which is beneficial to the fatigue life and increases the $\Sigma n/N$ value.

6. The experimental results as exhibited in Figure 6 showed that the tensile overload caused apparently a crack propagation retardation effect. In the process of equal space overload, the /224 crack propagation slowed down or stopped immediately after the addition of a peak tensile load. The crack propagation recovered to its original level after numerous cycles. Tests showed that, within a certain limit, the retardation time increased with increasing overload. This slowdown phenomenon of crack propagation induced by overload is referred to as the crack propagation retardation effect. This is an important concept in practical applications.

Table 3 Residual stress of measured initiation fatigue crack before and after on three steel notched testpieces

材 料 ①	试样号 ②	裂纹引发前的残余应力 ③ (kg/mm ²)		裂纹引发后的残余应力 ④ (kg/mm ²)	
		长度方向 ⑤	宽度方向 ⑥	长度方向 ⑤	宽度方向 ⑥
15MnVN	1	0	0	0	0
	2	-20.7	-34.5	-25.3	-29.7
	3	-18.4	-34.5	-20.1	-43.7
	4	-16.1	-27.6	-2.3	-39.8
28CrNi3MoV	1	0	0	0	0
	2	-25.3	-50.6	-27.6	-39.1
	3			-27.6	-39.1
	4			-32.2	-39.1
25Cr2NiMoV	1			0	0
	2			-18.4	
	3			-23.0	
	4			-23.0	
	5			-36.8	-41.4
	6			-36.8	-36.8

Key:

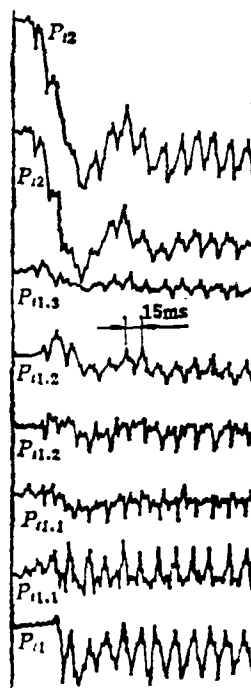
1. material
2. specimen number
3. residual stress before cracking
4. residual stress after cracking
5. length direction
6. width direction

References

- [1] Wheeler, D.C., ASME.D. (1972).
- [2] Engle, R.M. and Rudd, J.L., AIAA paper, No. 74-369.
- [3] J. Maarse., Fracture. (1977).
- [4] AFFDL., Vol. 1, ADAO 21700.
- [5] Matsuoka and Tanaka., Eng. Fract. Mech, (1976), Vol. 8, No. 3.

Rotating Stall. Our experimental result shows that when $n \leq 0.716$ ($B \leq 0.81$), the instability of the compressor of the engine is an abrupt overall stall. Figure 8 shows the time history of the total pressure fluctuation at various major cross-sections when rotating stall occurs. From the figure one can see that after the total pressure at the engine nozzle drops suddenly the total pressure of the compressor begins to fluctuate periodically. The pulsing frequency is 43.9% of the rpm.

Classical Surge. Figure 9 shows the time history of total pressure fluctuation of major cross-sections of an engine installed with a 36 mesh screen at its inlet during a surge at $\bar{n} = 0.87$. It is obvious that there is a rotating stall at 40.4% rpm at each stage of the compressor in this surge cycle.



/231

Figure 9. Time histories of fluctuating total pressure in main sections in a state of classical surge

1. $\bar{n} = 0.87$, 180° , 36 mesh

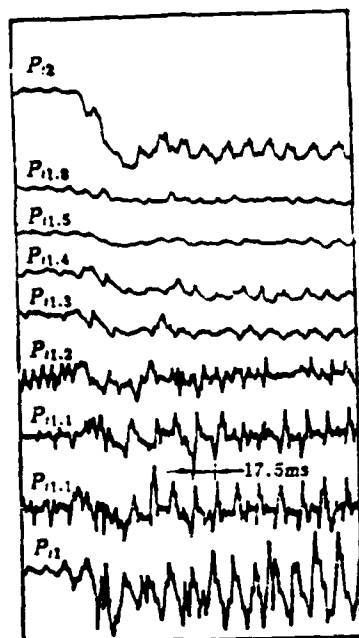


Figure 8. Time histories of fluctuating total pressure in main sections in a state of overall rotating stall

Key: 1. ($\bar{n} = 0.716$, no distortion)

$$B = \frac{U}{2a} \sqrt{\frac{V_p}{A_o L_o}}$$

where U -compressor plate speed; a -speed of sound; V_p -compressor nozzle volume; A_o -equivalent area of the annular flow path of the compressor; and L_o -equivalent axial length of the compressor.

Any specific engine has a critical value $B_{critical}$. When $B < B_{critical}$ the engine becomes unstable due to rotating stall. When $B \geq B_{critical}$

it is a surge. The nozzle volume of the compressor is a fixed value for a real engine. Therefore, the instability state is principally determined by the rpm of the engine. The $B_{critical}$ value of the turbojet engine studied in this work is approximately $0.81 < B_{critical} < 0.98$.

figure that the pressure waveform at various radii is basically the same on the same circumferential position of the inlet section.

(2) Comparison of Various Unstable States of the Turbojet Engine

Primarily, the unstable phenomenon of a turbojet engine is the flow instability of the axial compressor and the sudden deterioration of the engine performance. This instability may be rotating stall or surge. Furthermore, a surge may be categorized /230 as a classical, deep or drift surge. In general, instability is primarily determined by the rpm and nozzle volume, i.e., B value of the compressor^[6,7].

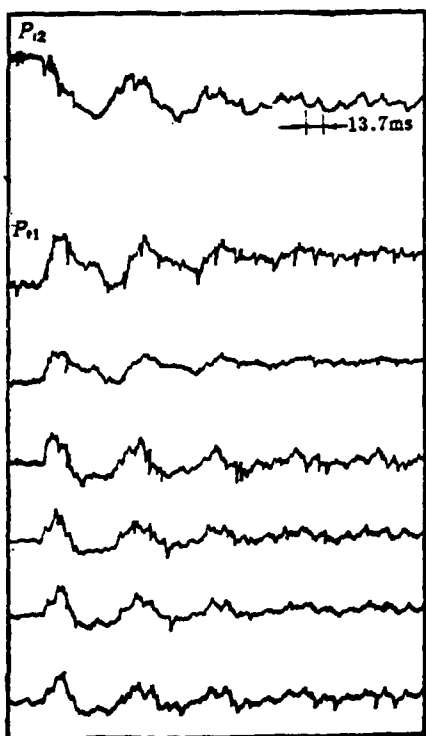


Figure 7. Time histories of fluctuating total pressure as a "drift" surge across (behind the tip-plate)

Key:
1. ($\bar{n} = 0.9$, tip-plate)

8. stable period before surge
9. temperature behind the turbine before and after the surge
10. vibration device reading during the surge
11. tip plate
12. tip plate
13. tip plate
14. tip plate
15. hub plate
16. hub plate
17. tip plate
18. hub plate
19. smaller
20. smaller
21. smaller
22. smaller
23. smaller
24. normal
25. normal
26. normal
27. 4 min.
28. 3 min.
29. 2 min.
30. 7 min.
31. 12-13 min.
32. 3 min.
33. 8-9 min.
34. 3 min.
35. Note: ↷ indicates that the blockage plate is rotating and → represents a sudden temperature increase

Figure 7 shows the time history of total pressure fluctuation at the inlet, outlet and other cross-sections of the compressor when the engine began to surge due to the turbulence-type dynamic distortion caused by the tip plate at $\bar{n} = 0.9$. It is apparent that an obvious rotating stall is associated with the surge cycle. The frequency is about 44.2% of the rpm. The frequency of the double surge cycle is about 16.7 Hz based on the first surge. As shown in the figure, the turbine nozzle temperature suddenly increased by nearly 100°C during the surge (the actual temperature rise might be larger due to inertia). However, this temperature is far lower than the turbine nozzle temperature of the engine at the same rpm during a surge caused by steady-state distortion. In the latter case, the turbine nozzle temperature is close to 800°C. One can see from the

36. smaller
37. no surge
38. smaller
39. surge
40. M + V represents the extent to forcing a surge,
i.e., adding blocking cone V to nozzle M
(equivalent to reducing nozzle area by about 33%)

The experimental result also indicates that the surge of the engine under this turbulence type dynamic distortion belongs to the "drift-mode". According to the extremum (distortion peak in this case) distribution theory in statistics, "drift surge" may be interpreted by the randomness of the pressure fluctuation at the inlet.

In this study, a total of eight surges appeared. Table 2 lists the details of these eight "drift" surges. All eight surges appeared several minutes after stable operation. Therefore, they are called "drift" surges.

Table 2. Details of eight "drift-mode" surges

1. 序号	2. 挡块位置	3. 堵塞比	4. 喷嘴状态	5. 转速	6. 导向器状态	7. 喘振时板位置	8. 喘前稳定时间	9. 喘振时涡轮后温度	10. 喘振时指示值
1	叶尖	50%	H	0.9	19 小一导	45°	27 4分	510℃	—
2	叶尖	50%	H	0.9	20 小一导	70°	28 3分	500→600	—
3	叶尖	50%	H	0.87	21 小一导	45°	29 2分	—	—
4	叶尖	50%	H	0.9	22 小一导	75°	30 7分	510→600	10~11
5	叶根	50%	H	0.9	23 小一导	105°	31 12~13分	545→600	11
6	叶根	50%	Φ	1.0	24 正常	180°	32 3分	—	—
7	叶尖	50%	Φ	1.0	25 正常	180°	33 8~9分	510→620	—
8	叶根	50%	Φ	1.0	26 正常	90°	34 3分	480→600	20

● 附注：↻表示挡块正在转动中；→表示温度突然增到。

Key:

1. number
2. blockage plate position
3. blockage ratio
4. nozzle condition
5. rpm
6. steering condition
7. plate position during surge

Table 1. Conditions for occurrence of engine surge

/229

1. 转速	2. 挡板畸变发生器					3. 网格畸变发生器			
	挡板	堵塞比	导向器	喷嘴	是否?	堵塞比	导向器	喷嘴	是否?
1.0	叶根 ¹³	50%	正常 ¹⁴	φ	喘 ¹⁵ (2次)	49.6%	正常 ¹⁶	φ	未喘 ¹⁷
	叶尖 ¹⁴	50%	正常 ¹⁴	φ	喘 ²⁰	49.6%	正常 ¹⁶	M+V ¹⁸	未喘 ²²
0.9	叶根 ¹³	50%	小一号 ²⁴	H	喘 ²⁵	49.6%	小一号 ²⁶	H	未喘 ²⁷
	叶尖 ¹⁴	50%	小一号 ²⁴	H	喘(3次) ³⁰	49.6%	小一号 ²⁶	M-V	喘 ³²
0.87						49.6%	小一号 ²⁶	H	未喘 ³⁷
	叶尖 ¹⁴	50%	小一号 ²⁴	H	喘 ³⁵	49.6%	小一号 ²⁶	M-V	喘 ³⁹

(40)

Key:

1. rpm
2. blockage plate distortion generator
3. screen distortion generator
4. blockage plate
5. blockage ratio
6. steering
7. nozzle
8. surge or not?
9. blockage ratio
10. steering
11. nozzle
12. surge or not?
13. hub-plate
14. normal
15. surge (2 times)
16. normal
17. no surge
18. tip-plate
19. normal
20. surge
21. normal
22. no surge
23. hub-plate
24. smaller
25. surge
26. smaller
27. no surge
28. tip-plate
29. smaller
30. surges (3 times)
31. smaller
32. surge
33. tip-plate
34. smaller
35. surge

3. Turbojet Engine Response to Turbulence-type Dynamic Distortion

(1) "Drift-mode" Surge Generated by Turbulence-type Dynamic Distortion

The experimental result of this work shows that the turbojet engine is much more sensitive to the turbulence-type dynamic distortion than to the steady-state distortion caused by the screen. The reason primarily is because the latter distortion is essentially steady-state, while the former has strong pressure fluctuations. Therefore, the instantaneous distortion peak may be much larger than the steady-state distortion value. With a large instantaneous peak, as long as there is enough time (e.g., one revolution of the engine), the engine surges when the instantaneous peak reaches the limit. The blockage plate used in this work has a 50% blockage ratio over 180° , which is comparable to that of a 36 mesh screen (49.6%). There is little difference between the steady-state distortions. However, the effect on the stability of the engine differs significantly. From Table 1 one can see that the turbojet engine is much more sensitive in response to turbulence-type dynamic distortion than to steady-state distortion.

It is obvious from Table 1 that dynamic distortions generated by the blockage plate under the fire conditions shown on the left can cause the turbojet engine to surge. The distortions produced by the screen could not make the engine surge. Only when a smaller section and a blocking cone were used, the engine began to surge at certain revolutions.

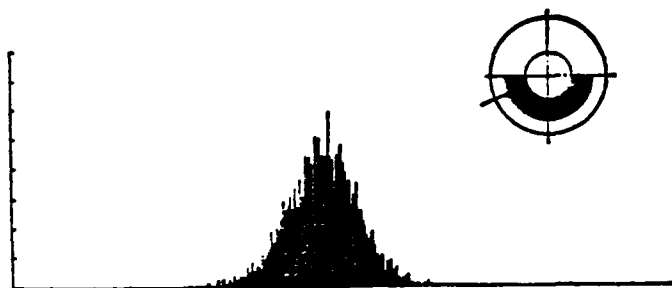


Figure 5. APD of fluctuating total pressure at the circumferential edge behind hub-plate

The amplitude of the pressure pulse generated by the blockage plate obeys a near normal distribution for a simple plate such as the one described above. Based on probability, one can further deduce that the pressure pulse still approximately follows a normal distribution with a complex plate.

Figure 6 shows the power spectrum density of fluctuating pressure behind the hub-plate. The distribution curve is relatively flat.

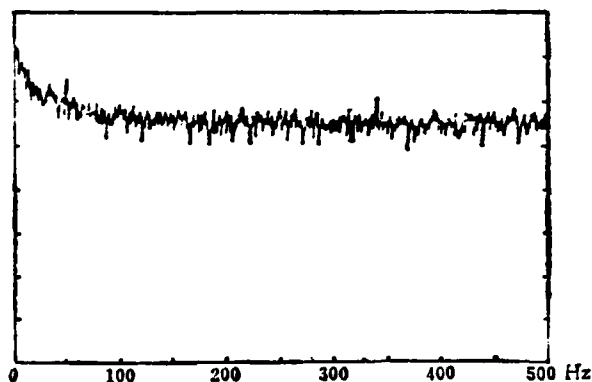


Figure 6. PSD of fluctuating total pressure behind the hub-plate

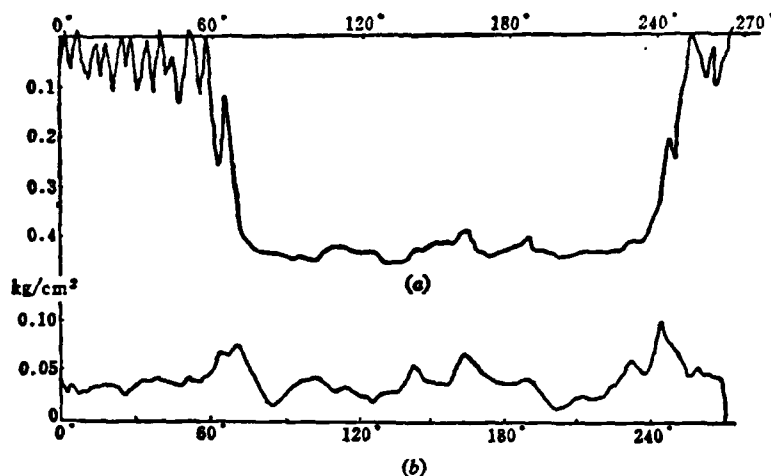


Figure 4. Circumferential distribution of the total pressure (a) and the rms of fluctuating pressure (b) behind plate

(2) Amplitude Probability Density (APD) and Power Spectrum Density (PSD) of Fluctuating Pressure

Figure 5 shows the amplitude probability density of random fluctuating pressure generated by the hub-plate. The upper right-hand corner in the figure shows the relative positions of the blockage plate and the measuring points. The solid circle indicates the measuring points. Figure 5 shows the amplitude probability density of the pressure signal measured at point 3 behind the plate (radial edge). From the figure, one can see that the APD of the pressure signal still remains an approximate normal distribution even in the vortex region around the plate.

/228

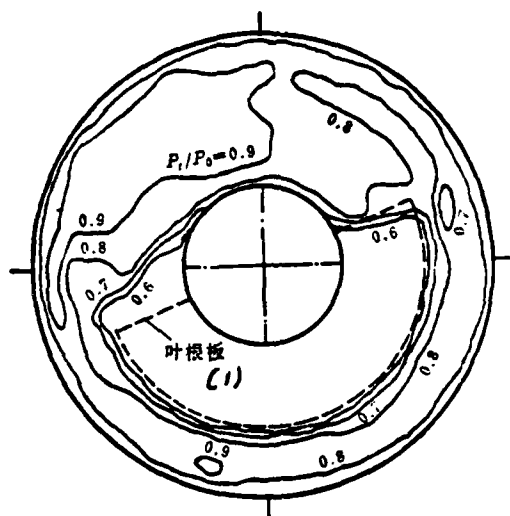


Figure 2. Total pressure distortion pattern behind the hub-plate
Key: (1) - blockage plate position

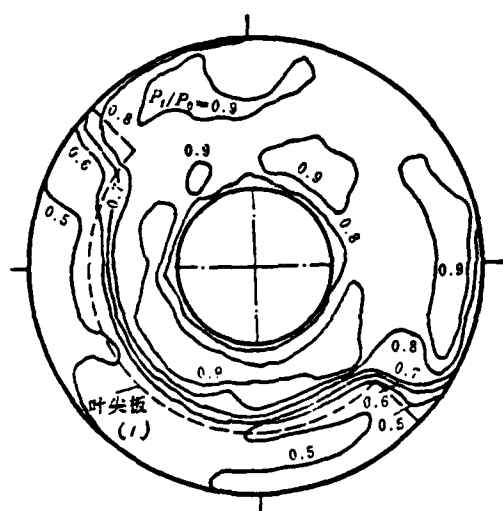


Figure 3. Total pressure distortion pattern behind the hub-plate
Key: (1) - blockage plate position

III. Results and Analyses

1. Steady-State Flow Field at Engine Inlet

Figures 2 and 3 are the time-averaged total pressure patterns behind the hub-plate, respectively, at $\bar{n} = 0.933$. The dotted line represents the position of the blockage plate. From the figures one can see that the low pressure range is basically consistent with the plate position at various RPM's. The pressure recovery lines are concentrated around the plate edges (radial and circumferential) which indicates that the pressure gradient is large. The pressure is relatively uniform behind the plate and in the "clean" region. In addition, it is also obvious that the low pressure zone was moved relative to the plate by a certain angle. The direction of deviation happens to be in the same direction as the circumferential vortex behind the plate. For instance, the circumferential vortex behind the tip-plate is counter-clockwise. The flow behind the plate is also counter-clockwisely rotated by an angle. When the circumferential vortex behind the hub-plate is clockwise, the flow field is also clockwisely rotated by an angle.

2. Dynamic Flow Field at Engine Inlet

(1) Analysis of Pressure Pulses

Figure 4 shows the circumferential distribution of the static pressure and the root-mean-square (rms) value of dynamic pressure (0~1000 Hz) measured by the dynamic pressure sensor at point 3 when the plate turns at $\bar{n} = 0.933$. From the figures one can see that the rms value of the fluctuating pressure is high at the circumferential edge of the blockage plate. Behind the plate, the pressure drops significantly. The extent of steady-state distortion, D , is about 0.22. Because point 3 of the pressure sensor is located at the radial edge of the blockage plate, the turbulence remains high.

II. Experimental Apparatus and Testing System

Figure 1 shows a simple sketch of the experimental apparatus. The tip-plate or hub-plate was secured on a rotating screen. Two 5-point pressure sensors were installed behind the blockage plate to measure the steady-state and dynamic pressure. The angular spacing is 180° . Each sensor consists of 5 pairs of steady-state and dynamic sensing points. Each dynamic sensing point was installed with a solid-state micro pressure transducer. They are distributed annularly. The total steady-state pressure and static pressure were measured using a Model SYD-1 digital pressure transducer and a Model XJ-100 circular pressure detector. The dynamic pressure pulses were measured by using a highly responsive, solid-state micro pressure transducer, an amplifier bridge and a 14 channel FM magnetic tape recorder to receive, convert, amplify and record the data for off-line processing. In addition, steady-state pressure and temperature were collected and processed by a 622 computer.

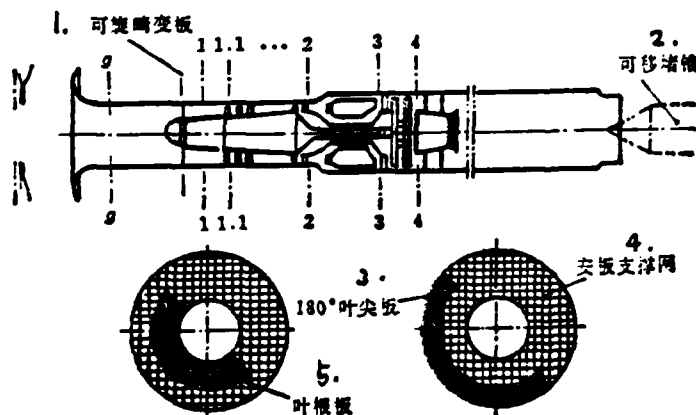


Figure 1. Testing Apparatus

- Key:
1. rotating distortion plate
 2. movable blockage cone
 3. tip plate
 4. plate support screen
 5. hub plate

to steady-state distortion, dynamic pressure distortion can more easily cause the engine to surge. In reality, an engine does not encounter a pure steady-state or dynamic pressure distortion. Instead, it is a combination of steady-state and dynamic distortion.

In practice, there are three types of dynamic pressure distortion frequently encountered by a turbojet engine: (1) pulse-type, such as the one caused by a temporary failure to start up at the inlet due to a certain reason, (2) homogeneous oscillation type, such as the one caused by inlet surge leading to axial oscillation of the shock wave, and (3) turbulent-type, such as the one caused by gas flow separation due to the interference of the trailing wave and the boundary layer when the inlet is operating in a supercritical state. Turbulent-type dynamic distortion is one of the most common dynamic distortions. In addition to the reason mentioned above, other reasons such as taking off in cross-wind, flow separation at the inlet caused by high attack angle or large yawing angle, separation in the inlet pipe, smooth flow layer swallowed by the inlet, or turbulence generated by other aircraft, belong to this type of dynamic distortion.

When an inlet/engine compatibility test is conducted, a simulation device is usually used to generate turbulent-type dynamic pressure distortions. In this work, a blockage plate was used to generate turbulent-type dynamic distortions. It was used to determine the steady-state and dynamic aerodynamic parameters of this distorted flow field, to analyze the statistical characteristics of the distorted flow field, and to investigate the turbojet engine response to this turbulence-type dynamic distortion. /226

An Experimental Investigation on Turbojet Engine Response to
Turbulence-type of Dynamic Inlet Distortion *

Northwestern Polytechnical University

Chen Fuqun, Li Wenlan, Wang Zongyuan, Cong Mengzi, Lu Baoquan
and Zheng Lizhi

Abstract

The response of a turbojet engine to the turbulence-type dynamic distortion is discussed in this paper. The turbulence-type dynamic distortion is caused by a blockage at the inlet section by the blade-tip or blade-hub region. The circumferential range of the blockage plate is 180° and the blockage ratio is 50%. These two dynamic distortion generators are capable of creating very intense turbulent-type dynamic distortions at the tip-plate and hub-plate, respectively. When the RPM of the engine is $n = 1.0$, they will cause the turbojet engine to surge in a "drift-mode". In this work, a smaller turbojet engine was experimentally investigated (the first stage turbine-nozzle section was decreased by 12%). It showed that the turbulent-type dynamic distortion due to the same blockage plate also caused the engine to surge in a "drift-mode" at $\bar{n} = 0.9$. At $\bar{n} = 0.87$, when the inlet gas is "clean", the engine instability was a deep-mode surge. The inlet distortion generated by the screen produced a "classical mode" of surge. These results indicate that in addition to RPM, the instability of an engine is also related to inlet conditions.

I. Introduction

Inlet distortion causes the stability of a turbojet engine to decline. A serious pressure distortion will make the engine surge. The turbojet engine responds much more sensitively to a dynamic distortion than a steady-state distortion^[1-3]. Compared

*Received in September 1983

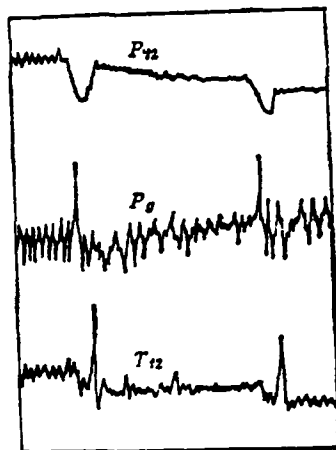


Figure 10. Time histories of fluctuating total pressure in main sections in a state of deep surge

1. $\bar{n} = 0.87$, no distortion

Deep Surge. Figure 10 shows the time history of the total pressure fluctuation of the major cross-sections of the engine with a "clean" inlet at $\bar{n} = 0.87$. From the figure, one can see that there are two surge cycles of unequal frequencies.

The experimental result shows that the engine instability is overall rotating stall at $\bar{n} \leq 0.716$, and it is a surge when $\bar{n} \geq 0.87$. It was also found that, in addition to the major factor rpm, the instability status of the engine differs with the structures and operating conditions in front and behind the compressor (such as gas inlet, turbine area, etc.).

Comrades Liu Sihong, Huang Zhitou, Guo Weimin, An Jicai, Hu Zhengfeng, Tu Ge and Wu Yafeng (data processing group) also participated in this work.

References

- [1] Williams, D.D. and Yost, J.O., Some Aspects of Inlet/Engine Flow Compatibility, The Aeronautical Journal, Vol. 77, No. 753, (1973), pp 483-492.
- [2] Plourde, G.A. and Brimelow, B., Pressure Fluctuations Cause Compressor Instability, AFAPL-TR-69-103, June (1970).
- [3] Amin, N.F. and Hollweger, D.J., F/A-18a Inlet-Engine Compatibility Flight Test Result, AIAA Paper NO. 81-1393.
- [4] Brimelow, B., Collins, T.P. and Prefferkorn, G.A., Engine Testing in Dynamic Environment, AIAA Paper No. 74-1198.
- [5] Li Sipei, Mathematical Treatment of Experiments, Science Publishing Co., (1980), pp 46-52.
- [6] Greitzer, E., Surge and Rotating Stall in Axial Flow Compressor, Pt I. Theoretical Compression System Model, Trans. of ASME, Vol. 98, April (1976), pp 190-198.
- [7] Greitzer, E., Surge and Rotating Stall in Axial Flow Compressor, Pt II. Experimental Results and Comparison with Theory, Trans. of ASME, Vol. 98, April (1976), pp 199-217.

Using a Two-Dimensional Laser-Doppler Anemometer to Study /233
a Complex Flow Field in a Combustor *

Northwestern Polytechnical University

Lin Qinxun, Ding Yisheng, Du Qinfang, Tang Ming and Xiao Ningfang

Abstract

This paper summarized some results and experience in using a two-dimensional Laser-Doppler anemometer to measure the flow field in an evaporation type combustor of an aircraft engine. Furthermore, they were compared to those obtained by conventional methods.

I. Introduction

The flow field in a combustor is a complicated three-dimensional flow field with return flow. The more we understand its velocity distribution, turbulence distribution, and the return flow pattern and size, the more certain we are when we design and modify the combustor.

Flow field data can be obtained using a conventional pitot tube or hot-wire anemometer. However, the information obtained by these contact type measurements is very limited because the cross-section measured is also limited. In addition, probes and support rods affected the flow field, causing distortions. Therefore, the results are not satisfactory.

Laser anemometry is of the non-contact type which is far more advantageous. It is a new technique developed in the 70's which grew rapidly in the late 70's^[1]. It has already become a comprehensive system including computer data processing and control. Laser Doppler anemometry principally relies on the monochromation and directivity of the laser to measure the flow velocity using the Doppler effect of the laser light scattered by fine particles moving along with the flow^[2].

*Received in September 1983

We employed a DISA Corp. dual color backscattering system which uses the blue and green light in the argon ion laser to measure the two velocity components on a vertical plane. It is also equipped with a computer controlled two-dimensional movement mechanism to allow the point of measurement to move on a horizontal plane. Thus, a two-dimensional field can be measured on one plane. The system also includes a two-dimensional optical and electrical frequency shift system to determine the direction of the flow. This is absolutely necessary in the study of the flow field in a combustor with return flows.

However, it is still inadequate to be only capable of measuring a two-dimensional flow field for the research of the flow field in a combustor. In order to extend its capabilities, we designed and fabricated a platform which is capable of moving the entire system up and down, as well as rotating the system around an axis on a horizontal plane. Consequently, the system can measure a three-dimensional flow field. Figure 1 shows the overall system.

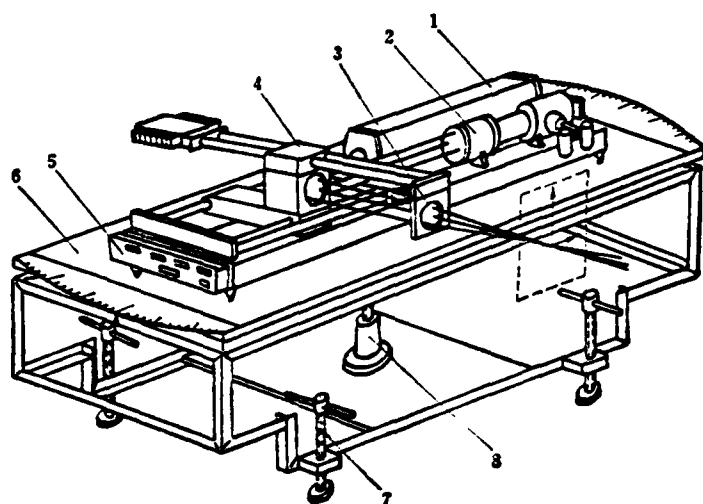


Figure 1. Schematic of the LDA System

Key:

- 1. argon ion laser
- 2. optical components
- 3. lens
- 4. mirror assembly
- 5. base
- 6. platform
- 7. screw support
- 8. elevation device

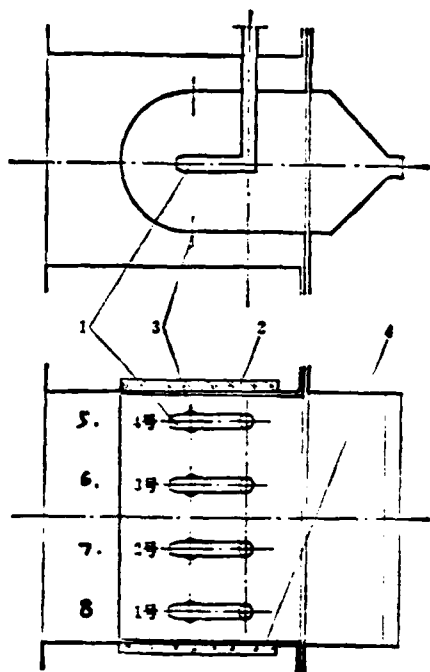


Figure 2. Schematic of the Vaporizing Tube Model Combustor

- Key:*
1. vaporizing tube
 2. high quality glass window
 3. primary combustion aperture
 4. optically flat front window
 5. No. 4
 6. No. 3
 7. No. 2
 8. No. 1

Figure 2 shows the schematic of the vaporizing tube combustor used in the experiment. The model is rectangular with four vaporizing tubes. The tube center spacing is 70 mm and the tube diameter is 15 mm. There are observation windows on both sides of the combustor. Because the front window is especially important to the back scattering system, it is optically flat. The rear window is used to minimize the weak wall reflection of the laser to improve the signal to noise ratio.

/235

II. Analysis and Comparison of Measured Results

In the measurement, the measured plane was divided into rectangular lattices. The intersections were calculated and given to the computer through the terminal. The computer manipulated the control mechanism to the location to perform the measurement from point to point. At each position, we asked the computer to take 100 valid samplings. Therefore, the measured velocity at any point is the average value of 100 measurements. From the distribution of these 100 samplings, we could also determine the root-mean-square (rms) of the velocity fluctuation at that point. Subsequently, the turbulence distribution could be obtained. According to the theory of error, we believe that the mean of 100 sampling points is sufficiently accurate.

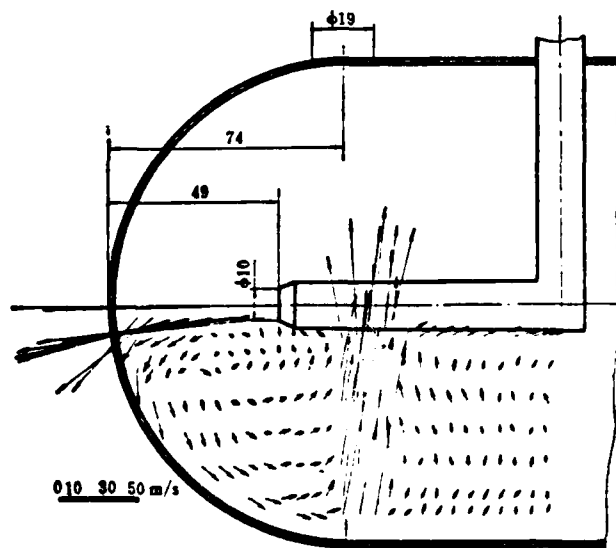


Figure 3. Velocity Profile in the Vertical Plane Passing Through the Centerline of No. 2 Tube

Figure 3 shows the velocity profile in the vertical plane passing through the center line of the No. 2 tube. The vertical spacing of the lattice is 10 mm. Near the bottom wall and at the center of the vortex, we added one additional row for measurement. The spacing is 5 mm. The horizontal spacing is also 5 mm.

From Figure 3 one can clearly see the structure of the return flow area at the head. Two symmetric vortices were created by the vaporizing tube and primary combustion aperture jets (the figure only shows the lower vortex). The area of the vortex occupies approximately 55% of the head cross-section. It is also possible to determine the center of the vortex from Figure 3. From flow field data we were able to determine that the mean revolution of the vortex is about 2700 rpm.

From Figure 3 one can also observe the primary combustion jet stream. The flow behind this cross-section is also directed upward towards lower velocity and then turns toward the nozzle near the vaporizing tube. The average upward velocity is about 5% of the primary jet stream velocity.

Because the primary aperture did not have a folded edge, although its diameter is 19 mm, yet its effective nozzle area is only about one half its original value due to the compression of the wash down flow created by the collision of the vaporizing tube flow against the wall. On the measuring cross-section the width of the primary flow aperture is only 10 mm. Furthermore, it was totally pushed to the rear of the aperture. This fully demonstrates that an aperture with a folding edge has a relatively low flow coefficient: approximately 0.5. /236

Figure 4 shows the distribution of the rms value σ of the velocity fluctuation in the vertical plane passing through the center line of No. 2 tube. One can see that the σ distribution is not uniform. The average σ in the entire flow field is about 15.7 m/sec, which is considerable. In the boundary layer of the primary flow, the σ value may be twice as high as the average.

At the axial center of the flow, the σ value is near the average level. This is obvious from the humps shown in Figure 4.

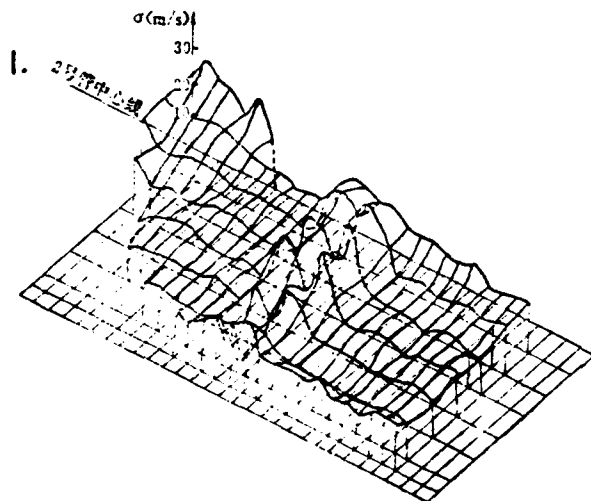


Figure 4. Distribution of the RMS Values of the Velocity Fluctuation in the Vertical Plane Passing Through the Centerline of No. 2 tube

1. center line of No. 2 tube

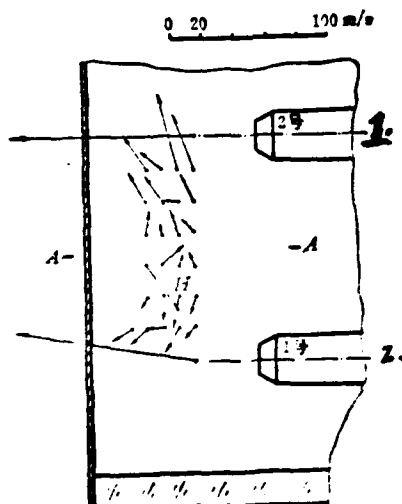


Figure 5. Velocity Profile Between No. 1 and No. 2 Tubes in the Horizontal Plane Passing Through Their Centerlines

1. No. 1
2. No. 2

Figure 5 shows the velocity vector profile at the head of the combustor between No. 1 and No. 2 vaporizing tubes, measured on the horizontal cross-section passing through the axes of all the vaporizing tubes. From Figure 5 one can see that under the influence of the vaporizing flow, other flows were attracted to it. This jet stream hits the wall and splashes in all directions as it turns. The ones on the right and left combine with the symmetric flow from the neighboring tube and the resultant flow goes to the rear. Soon after, it collides with the primary jet streams and thus produces a hole (as shown in Figure 5 at H). In order to verify this phenomenon, an additional row of velocity vectors was measured in the vertical plane along A-A. Figure 6 shows the result. The velocity vector profile shown in Figure 6 also can clearly illustrate the air pocket formation phenomenon described above.

All these figures show that the flow field in a vaporizing tube combustor is extremely complex. In order to verify the reliability of using a laser anemometer to measure such a complicated flow field, a three-hole probe was also employed to measure the flow field under similar conditions. Figure 7 shows the velocity vector field measured in the vertical plane passing through the axis the No. 2 tube by using a three-hole probe. It agrees with Figure 3. However, the scale is different. From Figures 3 and 7 one can see that the return flow structure is essentially the same and the vortex center position is also identical. But, the measuring cross-section cannot be as close using the three-hole probe as laser anemometry. This is the advantage of laser anemometry.

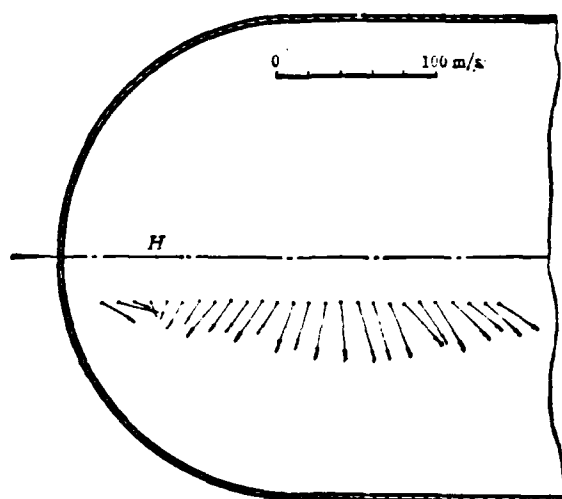


Figure 6. Velocity Profile in the Vertical Plane Containing the Line A-A

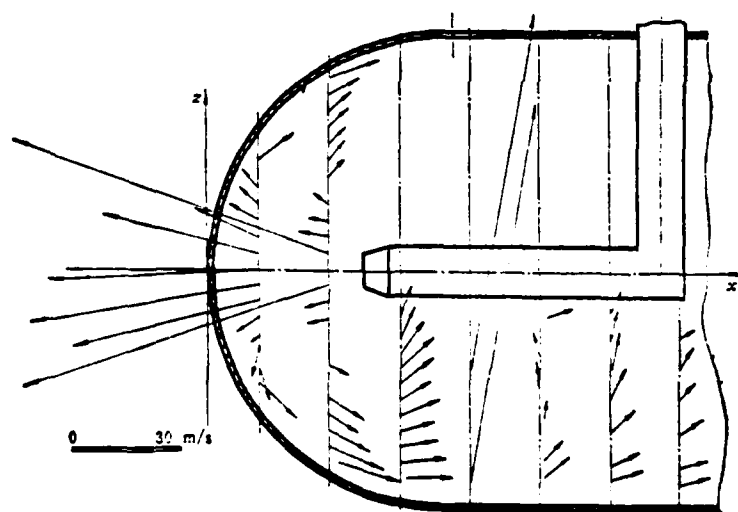


Figure 7. Velocity Profile Measured by a Two-dimensional Pitot Probe in the Vertical Plane Passing Through the Centerline of No. 2 Tube

Figure 8 shows the velocity profile measured by a Pitot probe in a vertical plane passing through the line A-A. It agrees with Figure 6. Figure 8 also draws the result obtained with laser anemometry by using dotted lines for comparison. From Figure 8 one can see that the two methods are equivalent.

All these results show that the laser anemometer is a powerful tool to study the complex flow field in a combustor and the results are valid.

/238

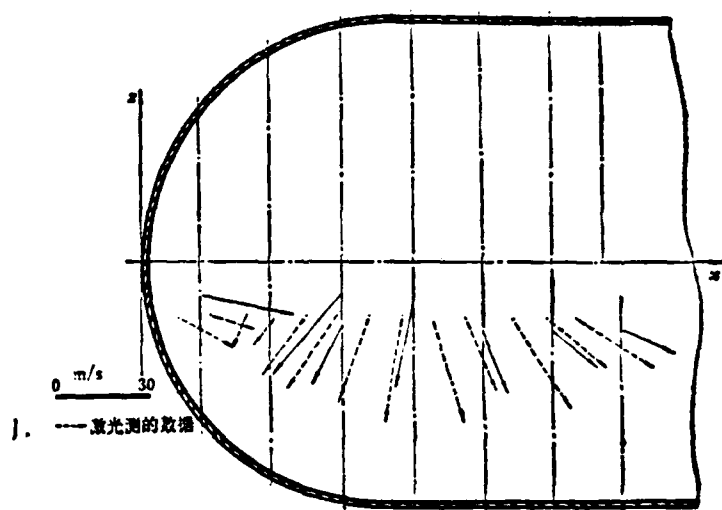


Figure 8. Velocity Profile Measured by a Two-dimensional Pitot Probe in the Vertical Plane Containing the line A-A

Key: 1. data measured with laser

III. Technical Problems in Applications

1. Calibration of the Instrument

As we know

$$V = K f_D \quad (1)$$

where V - flow velocity;

f_D - Doppler frequency;

K - instrument constant.

and

$$K = \frac{\lambda}{2 \sin \frac{\theta}{2}} \quad (2)$$

where λ - laser wavelength

θ - angle between light beams.

Because of the monochromatic nature of the laser, especially with an interference standard, the wavelength error is negligible.

The key is the accuracy of θ . The DISA system requires frequent user maintenance. Therefore, the actual θ value may differ significantly from the value given in the manual. We also discovered that the angle between the blue and green beams could hardly be adjusted at a right angle in our system. Sometimes this angle is only about 80° . This must be included in the determination of velocity.

However, these are system errors which can be eliminated by calibration. We calibrated the system by shining the light on a distant wall to measure the distance between the focal point to the spot and the distance between the spots. Then, the actual angles were determined.

2. Particle Problem

It is not easy to artificially add particles to the flow in order to improve the quality of the signal when we measure the entire flow field in high flow experiments to test combustor components. Fortunately, we do not have an air filter.

Therefore, there are considerable amounts of micro-particles in the flow. The measurement problem can be solved by relying on

these natural particles. However, this type of flow can easily contaminate the window to form a thin foggy layer to reduce the signal to noise ratio. With our gas supply, we must stop the experiment to wipe the windows after two hours of continuous operation. However, two hours of experimentation is already long enough not to cause any serious problem. /239

3. Three-dimensional Flow Measurement

A three-dimensional flow measurement problem can be solved by taking two measurements at two angles at the same point using a laser anemometer. The rotating working platform we developed enabled us to realize this measurement.

Figure 9 shows the basic principle of this approach. The projection of the velocity U perpendicular to the plane is one-dimensional, U_z . The other two dimensions are in the plane expressed by U_r and θ_r . A two-dimensional laser anemometer was used to take a measurement in the $+\alpha$ direction to obtain the projection of U_z and U_r , $U_{+\alpha}$. The projection of U_z and U_r , $U_{-\alpha}$, was obtained by measuring in the $-\alpha$ direction. Then

$$\operatorname{tg} \theta_r = \frac{1}{\operatorname{tg} \alpha} \frac{U_{+\alpha} - U_{-\alpha}}{U_{+\alpha} + U_{-\alpha}} \quad (3)$$

$$U_r = \frac{U_{+\alpha}}{\cos(\theta_r - \alpha)} \quad (4)$$

or

$$U_r = \frac{U_{-\alpha}}{\cos(\theta_r + \alpha)} \quad (5)$$

As long as the operating condition of the combustor remains unchanged in the $+\alpha$ measurement, the method will work. This is a basic requirement to ensure the validity of a point-by-point method. The velocity field shown in Figure 5 was obtained by this method.

6. Type B-1 Carbon Cloth Specimen

The stress-strain curve of the Type B-1 transverse carbon cloth specimen deviates from a straight line at 40% σ_{ult} (see Figure 8). Acoustic emission signals began from this point on. AE_r is 7×10 . There was interface separation laterally. Signals were found continuously until 45% σ_{ult} . The lateral layer separation continued and the shear was 45° . Cracks began to show radially with relatively strong release of energy. AE_r was 1.4×10^2 . Furthermore, another AE_r appeared at a 4% σ_{ult} interval apart. The maximum AE_{rt} is 2.25×10^4 . σ_{ult} is 5.25 kg/mm^2 . E is 1308 kg/mm^2 , ϵ is 0.61%, ν is 0.07 and the fracture surface is smooth (see Figure 4)

/246

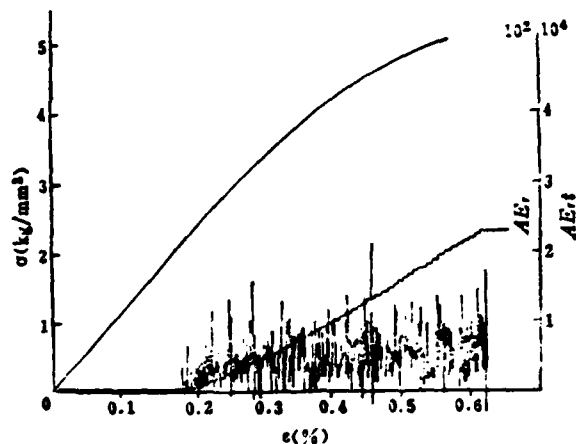


Figure 8. Stress-strain, AE-Strain Curve of B-1 Specimen

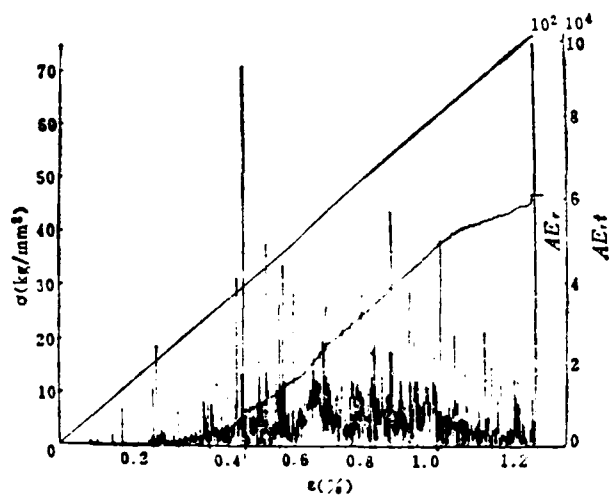


Figure 6. Stress-Strain, AE-Strain Curves of B-a Specimen

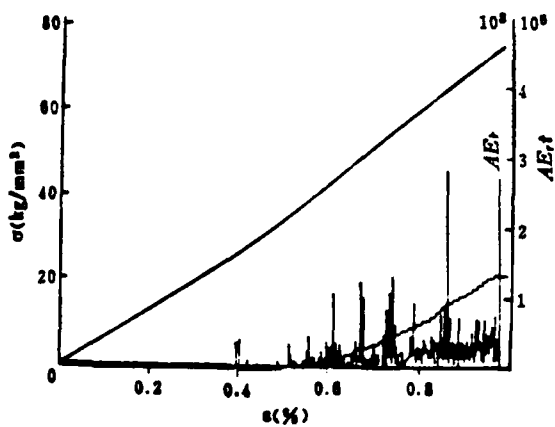


Figure 7. Stress-Strain, AE-Strain Curves of B-I Specimen

picked up. At 40% σ_{ult} , radial fibers broke and suddenly emitted a strong signal AE_r at 9.4×10^2 . Then, medium and small AE_r continued, corresponding to radial crack propagation and transversal separation, respectively. Finally, AE_r reached its full scale ($>10^3$) and the specimen was fractured. The maximum weighted ring is 6.1×10^4 .

5. Type B-I Carbon Cloth Specimen

The stress-strain curve of the Type B-I [-111-] longitudinal carbon cloth specimen (see Figure 7) showed a not so obvious turn at 40%. The slope changed slightly. However, linearity remained until destruction. The strength σ_{ult} is 75.14 kg/mm^2 . The modulus E is 8580 kg/mm^2 . The maximum strain ϵ_{max} is 0.98% and the Poisson ratio ν is 0.27. When the applied load was increased to 35% σ_{ult} , 2/5 of the maximum strain, the transverse layer began to degum with AE_r (4×10^2). At 50% σ_{ult} , another corresponding AE was found. Approximately 5% σ_{ult} apart, another transverse carbon cloth separation was separated. At 60% σ_{ult} , AE_r increased to 1.1×10^3 . It cracked radially. The maximum AE_r was 2.8×10^3 . Radial fibers began to snap. Before the final fracture, there were closely packed medium strength signals. The fractured cross-section is basically a clean break. However, we could still see the individual layers (see Figure 4). The maximum weighted ring is 1.4×10^5 .



Figure 4. Failure Mode of $[+45^\circ]$, $[30/60]$, B-I, B-1 Type Specimen

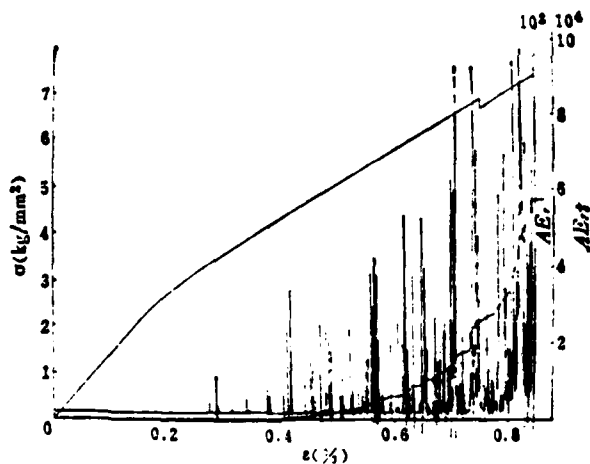


Figure 5. Stress-Strain, AE-Strain Curves of $[30/60]$ Specimen

Primarily because of the radial carbon cloth ply, the property is/245 very close to that of the 0° ply specimen. The strength is 73.5 kg/mm^2 , the modulus is 8333 kg/mm^2 and the Poisson ratio is 0.33. However, because the carbon cloth fibers are in both directions, the strain rate is high. In addition, a smaller $AE_r (10^2)$ began to appear early ($15\% \sigma_{ult}$). At this time, the transverse layer began to separate. After $25\% \sigma_{ult}$, acoustic emission signals

3. 30/60 Carbon/Epoxy Ply Specimen

When a load is applied to a [30/60] specimen, the stress-strain curve begins to deviate (see Figure 5). The slope of the straight line decreases. However, it still remains to be a straight line until 95% σ_{ult} . When the specimen is nearly destroyed, the curve begins to fluctuate. It continued to rise after dropping 2 kg until reaching 7.24 kg/mm^2 where destruction occurred. An acoustic emission signal (10^2) began to emerge at 40% σ_{ult} . The 60% ply began to degum along the 60% line. The 30° ply started to separate along the 30° line at 60% σ_{ult} . A medium intensity signal AE_r (3.2×10^2) was observed. The signals were getting closer. The interface was separated (see Figure 4). At 80 σ_{ult} , another interface was separated and AE_r reached 4.3×10^2 . The signals became more intense and concentrated. When the applied load reached 90% σ_{ult} , strong AE_r (9×10^2) started to appear. Every ply failed. The crack propagated which caused some medium intensity AE_r to be mixed in these signals. Finally, it cracked at the limit 7.24 kg/mm^2 . The maximum AE_r is 9.8×10^2 , the maximum AE_{rt} is 5.85×10^4 , the modulus is 1280 kg/mm^2 , the maximum strain rate is 1.4%, and the Poisson ratio is 0.3.

4. Type B-a Carbon Cloth Specimen

The stress-strain relation of [11=11] longitudinal carbon cloth type B-a specimen is always linear (see Figure 6).

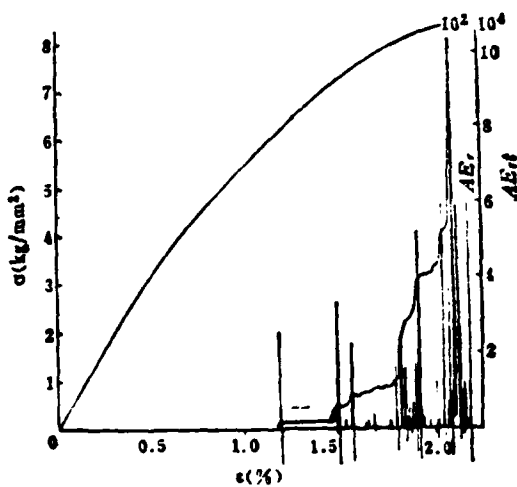


Figure 3. Stress-Strain, AE-Strain Curves of $[+45^\circ]_s$ Specimen

/244



Figure 2. Failure Mode of [0/90] Specimen

2. $\pm 45^\circ$ Ply Carbon Cloth/Epoxy Specimen

When the $\pm 45^\circ$ ply specimen was loaded to 35% σ_{ult} , the stress-strain curve is linear initially. When the load was increased, it deviated away from linearity. This is due to the inter-ply shear force along the 45° line as a result of tension (see Figure 3). When the load was increased to 65% σ_{ult} , which is 1/2 of the maximum strain, AE_r signals at 2.5×10^2 began to appear. In this instance, one ply was degumming along 45° which created a larger signal. Because the crack propagated in 45° , there were weak AE_r (2×10) signals. After reaching 95% σ_{ult} , the signals got much closer. The dense medium intensity AE_r corresponds to interface separation. A more intense AE_r could reach 6.7×10^2 . Every ply was sheared and snapped. The maximum AE_r is 8.3×10^2 . The maximum total number of weighted rings is 10^4 . Because of the mutual containing effect, the specimen usually does not break (see Figure 4). However, each ply cracked along $\pm 45^\circ$. The average strength is 9.24 kg/mm^2 , the modulus is 1033 kg/mm^2 , the maximum strain rate is 2.1%, and Poisson ratio is 0.54.

occurred more closely, approaching 3.5×10^2 . Even stronger AE_r , reaching $4-4.6 \times 10^2$, began to show up every 5% σ_{ult} . This represents the snapping of longitudinal fibers. In this interval, more and more delamination and longitudinal cracks were produced. AE_r also become closer. Finally, AE_r reached 9.6×10^2 when the material was fractured. The total number of weighted rings, AE_{rt} , is 1.9×10^2 . The ultimate strength σ_{ult} is 40.18 kg/mm^2 and the modulus is 4190 kg/mm^2 . The Poisson ratio of this specimen is 0.018. The experimental results are shown in Table 1 (with average values tabulated). There are two failure modes for this perpendicular ply specimen (see Figure 2). One cracks along a transverse (90°) section. However, most longitudinal fibers did not snap. Only a few broke off. Because of the 90° crack, many longitudinal cracks were found due to concentrated stress. The entire specimen was not fractured. This is a frequently encountered failure mode. The other kind is a total transverse crack. The crack is neat, with small bands of longitudinal fibers in some cases.

/243

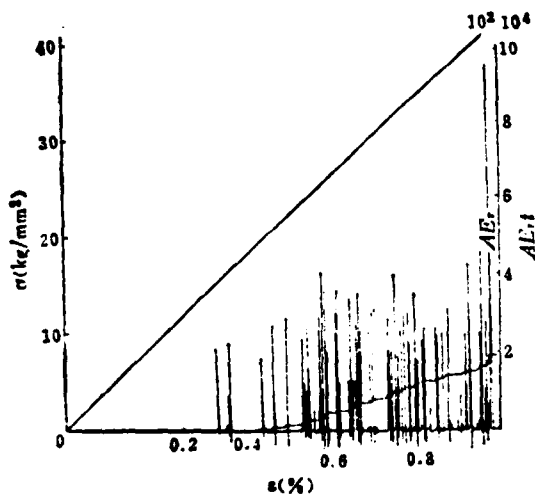


Figure 1. Stress-Strain, AE-Strain Curves of $[0/90]_s$ Specimen

Through a composite threshold, the interference resistance is improved in order to obtain the acoustic emission signal when the specimen is destroyed. A 120 KHz resonance piezo electric probe was placed on the specimen with grease in order to ensure good acoustic coupling. A transducer was used to convert acoustic emission to electric signals. After amplification, identification and signal analysis, various representative parameters (such as specimen, ringing, energy, ring width, weighted ringing, etc.) were obtained and displayed on the counter. Furthermore, the relations between increment of acoustic emission and cumulated acoustic emission with time^[2] were recorded on the X-Y₁-Y₂ instrument, respectively. Because a weighted ring represents the fluctuation of the entire original ringing area of the acoustic emission, which includes the amplitude of the acoustic emission ringing signal and the ringing time, weighted ringing can better reflect the energy of material distortion and destruction than other parameters. Therefore, weighted ringing was chosen as a parameter in this work. In the figure, AE_r is the weighted ringing increment and AE_{rt} is the cumulative weighted ringing. Experimental condition: the pre-amplifier is 40 db, the main amplifier gain is 35 db, and the threshold voltage is 2V.

III. Experimental Results

1. Perpendicular Ply Carbon/Epoxy Specimens

When the $[0/90]_s$ ply specimen was under a tensile load and the slope of the stress-strain line decreased slightly after reaching 40% of the ultimate strength (σ_{ult}), the acoustic emission signal began to appear. The weighted ringing was 2.1×10^2 , which is 1/3 of the maximum strain (see Figure 1). From this point on to 60% σ_{ult} , weighted ringing of similar magnitude appeared in distant intervals. This corresponds to the separation of the 90° fiber. From 60% σ_{ult} on, longitudinal cracks began to emerge and weighted acoustic emission rings (AE_r)

Table 1 The Experimental Result of Properties and AE of Six Ply Carbon/Epoxy

/242

1. 铺层	2. 试件类型	3. 试件数	4. 截面积 $F(\text{mm}^2)$	5. 强度 $\sigma_{ult}(\text{kg/mm}^2)$	6. 模量 E (kg/mm^2)	7. 泊松比 ν	8. 开始出 现AE, $\delta_{ult}\%$	9. 突变 AE, 信 号的 $\delta_{ult}\%$	10. 出现 最大 AE, 的 $\delta_{ult}\%$	11. 相对AE 最大值	
										AE_r	AE_{r1}
[0/90] _r	C-正-1	5	27	41.6	4268	0.018	40	50	100	9.6×10^2	1.9×10^4
[$\pm 45^\circ$] _r	C- $\pm 45^\circ$ -1	5	18.12	9.25	1033	0.54	65	85	95	8.3×10^2	10^4
[30/60]	C-I-1	5	53.5	7.76	1459	0.84	40	60	92	9.8×10^2	5.85×10^4
12 布[11=11] _纵	B-a	4	15.31	73.2	8035	0.39	15	40	100	10^3	6.1×10^4
13 布[-111-] _纵	B-I	4	17.5	74.4	8499	0.295	35	60	87	2.8×10^3	1.4×10^5
14 横向碳布	B-1	4	20	5.97	1282	0.083	40	45	86	2.2×10^2	2.25×10^4

Key:

1. ply
2. specimen type
3. specimen number
4. cross-section
5. strength
6. modulus
7. Poisson ratio
8. $\delta_{ult}\%$ when acoustic signals AE_r begin to appear
9. $\delta_{ult}\%$ when acoustic signals AE_r suddenly emerge
10. $\delta_{ult}\%$ at maximum AE_r
11. relative maximum AE_r
12. cloth [11=11] longitudinal
13. cloth [-111-] longitudinal
14. transverse carbon cloth

II. Experimental Apparatus and Testing Methods

The experiment was conducted on an Instron 1195 tester. The load adding rate is 1 mm/min. Distortion was measured by an extension meter. A strain plate was used to determine the Poisson ratio. The load-displacement or stress-strain curve was automatically recorded. The destroyed specimens were examined microscopically.

A SFS-4 four channel acoustic emission device was used to monitor the destruction process when a specimen is under load.

In this work, six multi-ply epoxy composite materials (including 0/90, $\pm 45^\circ$, 30/60 and three carbon cloths) were tested to determine their strength, modulus, maximum strain rate and Poisson ratio. Their stress-strain relations and acoustic emission signals were also obtained. Acoustic emission, together with microscopy, were used to analyze the relation between acoustic emission and the destruction, crack propagation and stress level of the composite material in order to study the destruction characteristics and mechanisms.

I. Materials and Specimens

The materials tested are carbon fiber reinforced epoxy (L180/648) composite materials, including $[\pm 45^\circ]_s$, [30/60], [0/90]. Their fiber volume content V_f is approximately 60%. Three carbon cloths: Type B-a consists of six plies, two longitudinal plies on either side and two transverse plies in the middle [11=11]. The specimen was cut longitudinally. Type B-I consists of 5 plies of carbon cloths, one transverse ply on either side and three longitudinal plies in the middle [-111-]. The specimen was cut longitudinally. Type B-II is a transverse carbon cloth specimen. Each ply has $\pm 45^\circ$ fibers. The specimen was rectangular. The geometric dimensions of the specimen and the experimental results are shown in Table 1.

Characteristics of Multi-ply Carbon/Epoxy Composite

Materials and Acoustic Emission Analysis*

Institute of Mechanics; Academia Sinica

Xian Xingjuan and Jiang Conxing

Abstract

The tensile failure behavior of six multi-ply carbon fiber reinforced epoxy composite materials was investigated by using the acoustic emission technique to monitor their damage propagation processes in order to analyze their failure mechanisms.

New high performance carbon fiber reinforced epoxy composite materials are used in aerospace, machinery and athletic equipment. Because of the complicated working conditions, a multi-ply configuration is required to satisfy various combinations of pulling, compressing, bending, shear and twist loads. The specific ply design must be determined by the major load. The destruction of a multi-ply composite material is more complicated than that for a unidirectional ply material. The mechanical properties and destruction mechanisms must be studied experimentally. Acoustic emission can be used to detect and record the destruction process in a non-destructive test^[1]. Furthermore, a relatively large area of the material tested can be monitored without moving the position of the probe. Therefore, it is used more and more widely. Acoustic emission relies on the principle that an elastic wave is generated due to the relief of strain in a material or structure under load to evaluate the properties of the material through detecting defects, deterioration and destruction. Acoustic emission can be used to detect shearing, tensile yield, delamination and fiber snapping, adhesion strength, etc.

*Received in May 1983

Comrades Ge Lichen, Chen Binglu, Shi Jingxun, Zhang Changshen, Shu Huiling and Hu Qing also participated in the experimental work. Without their dedication, the work could not have been done.

References

- [1] Lakshminarayana, B. and Runstadler, P., Measurement Methods in Rotating Components of Turbomachinery, ASME, (1980).
- [2] Measurement of Aerodynamic Parameters of Aircraft Engines, edited by Northwestern Polytech University, Defense Publishing Co., (1980).
- [3] Durst, F., Melling, A. and Whitelaw, J.H., Principles of Laser-Doppler Anemometry, Academic Press, London, (1976).

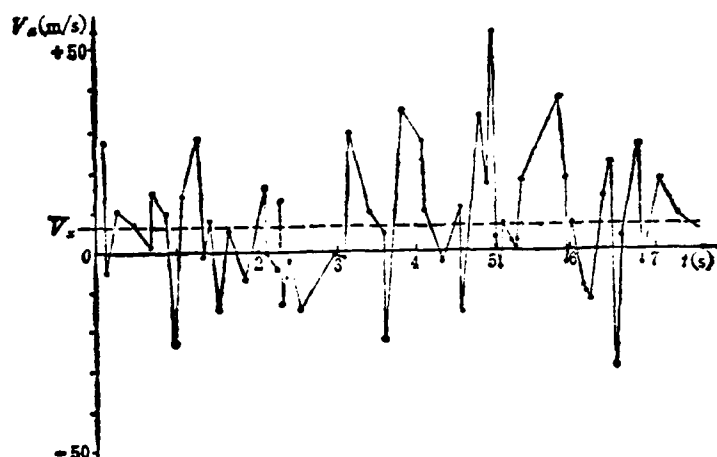


Figure 10. V_x vs. Time at a Given Point in the Combustor

Furthermore, the velocity value fluctuates randomly with time (with the exception of the core region in the jet stream). It may even be positive in one instance and negative in another. Figure 10 shows the velocity, V_x , change with time. One can see that although the mean value of V_x is positive, many instantaneous values are negative.

Therefore, we not only must accurately use an electrical /240 frequency shift to find the return flow region, but also use a sufficient shift even at a point whose mean velocity direction is known. Otherwise, the measured time averaged value will contain a large error.

In addition, one can see from Figure 10 that the fluctuation may be several times higher than the mean. Therefore, the bandwidth of the filter must be wide enough.

In summary, the selection of the electrical frequency shift and the filter bandwidth is a serious problem in measuring the flow field of a combustor as the point of measurement shifts. Otherwise, serious consequences will result.

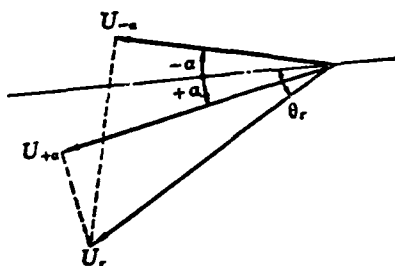


Figure 9. Geometry of Two Three-dimensional Velocity Measurements

In reality, the positive and negative values of α need not be the same. This is a simple geometry which we will not derive in detail.

4. Selection of Electrical Frequency Shift and Filter Bandwidth

The flow field in a combustor is three-dimensional in space. It also contains a return flow. In order to prevent measuring the wrong flow direction, it is usually necessary to use a frequency shift. Moreover, the electrical frequency shift must be large enough.

IV. Discussion and Conclusions

(1) From the tensile mechanical properties of the six multi-ply carbon/epoxy composite materials studied in this experiment, the two longitudinal carbon cloths (Type B-I and B-a) are better. The σ_{ult} and E values are approximately 85% of those for the 0° ply material. The value of ν is also close (0.3). The σ_{ult} of the Type B-I transverse carbon cloth is the lowest. Its ϵ_{max} is also the smallest (0.6%). ν is also small 0.083. The strength of an orthogonal ply specimen is approximately 50% that of the 0° ply material. Therefore, one can see that the tensile load is primarily on the 0° ply. The σ_{ult} and ϵ of the $\pm 45^\circ$ specimen are similar to those of the [30/60] specimen.

(2) Acoustic emission can be used to monitor the destruction of a composite material and to identify the properties of various multi-ply composite materials. They have common patterns as well as individual properties. The weighted ring of acoustic emission can reflect the release of the strain energy during the initial damage. It usually appears at the turning point of the stress-strain curve, at approximately 40% σ_{ult} . (However, it appears at a higher stress for this batch of $\pm 45^\circ$ specimens. In other $\pm 45^\circ$ specimens tested earlier by the authors, AE was also found at the turning point.) It is approximately at 2/5 of maximum strain (only Type B-a at 1/5 maximum strain). In [$\pm 45^\circ$], [30/60] and transverse carbon cloth specimens, AE_r , occurred at the yield strength of the material. Because the AE_r value of substrate shear separation is usually in the $1-4 \times 10^2$ range (only Type B-1 transverse carbon cloth has a slightly lower value), crack propagation occurs at near 60% σ_{ult} (see Table 1) and longitudinal cracks take place at 90%. The maximum AE_r value is generally around 10^3 (larger for Type B-a and smaller for Type B-1). However, there is a big difference in the total number of maximum weighted rings. This indicates that the total energy released by different multi-ply materials at their destruction is different. It is the highest for Type

B-I longitudinal carbon cloth (1.4×10^5). The rest of the materials are in the 10^4 - 8.6×10^4 range. From the acoustic emission pictures, the deformation and energy release of the carbon cloth are continuous. There is an abundance of signals with longitudinal signals. In bidirectional ply specimens, AE signals are discontinuous. Initially, they are wide apart. After 60% σ_{ult} , signals then began to pick up. Signals appear in regular intervals with perpendicular ply specimens. The weighted ring does not vary significantly. This reflects the anisotropic characteristics of the orthogonal plies of $[0/90]_s$ materials. The destruction of $\pm 45^\circ$ specimens primarily occurs in the late stage. The release of energy is concentrated in the final stage. Therefore, the AE_r cumulation curve rises steeply. It is similar with 30/60 specimens. The relative position of the fractured cross-section to the sensor is also different. The AE is also slightly different. Different carbon fiber or acoustic emission properties will also result in different AE patterns.

(3) A multi-ply carbon/epoxy composite material is damaged from the separation of the interface due to the shear force exerted on the substrate. A crack is produced and it begins to propagate. When the number of cracks increases and cracks enlarge to a certain extent, the high stress causes the surrounding fibers to snap. Finally, the specimen is totally destroyed. The destruction mode is different for various multi-ply materials. The longitudinal carbon cloth is damaged by brittle fracture. The cross-section is neat. The stress-strain curve is linear. The $[\pm 45^\circ]$ and $[30/60]$ specimens are destroyed primarily to shear force. The crack propagates along the interface (i.e., fiber direction) and gradually destroys the specimen. Finally, it is unable to carry the load. However, the specimen usually does not break. The early part of the stress-strain curve is linear and it begins to yield (slightly) after 40%. A perpendicular multi-ply material has the properties of both types. It sometimes breaks due to brittleness. However, in most cases the 90° layer is separated and the 0° layer does

/247

not break open. But, it has many longitudinal cracks.

The mechanical characteristics of composite materials can be fully utilized by designing the plies according to the load. It is an effective method to use acoustic emission to identify the properties of different multi-ply composite materials, to analyze the damage process and to predict destruction.

The authors wish to express their gratitude to Comrades Zheng Weiping, Liu Jingzhen and Xie Changchun for their participation.

References

- [1] Xian Xingjuan, "Non-destructive Testing of Composite Materials", Progress in Mechanics, 1 (1982) 280-286.
- [2] Chen Xihong et al, "Introduction to the Model SFS-4 Acoustic Emission Apparatus", Applications of Electronic Techniques, 1 (1981) 1-20.
- [3] R. Teti, A.D. Ieio, I.C. Visconti, Progress in Science & Engineering of Composites (Proc. of ICCM-IV) 1507-1514.

END

FILMED

10-85

DTIC